Dedicated to innovation in aerospace

TU Delft Delft University of Technology

COMPANY CONFIDENTIAL

NLR-TR-2022-103 | Oct 2022

In718-SS316L Functionally Graded Materials Produced by Directed Energy Deposition

A Comparative Study on Deformation due to residual stress through Simulation and Experimentation

MSc. Thesis A.D.D. van der Eems

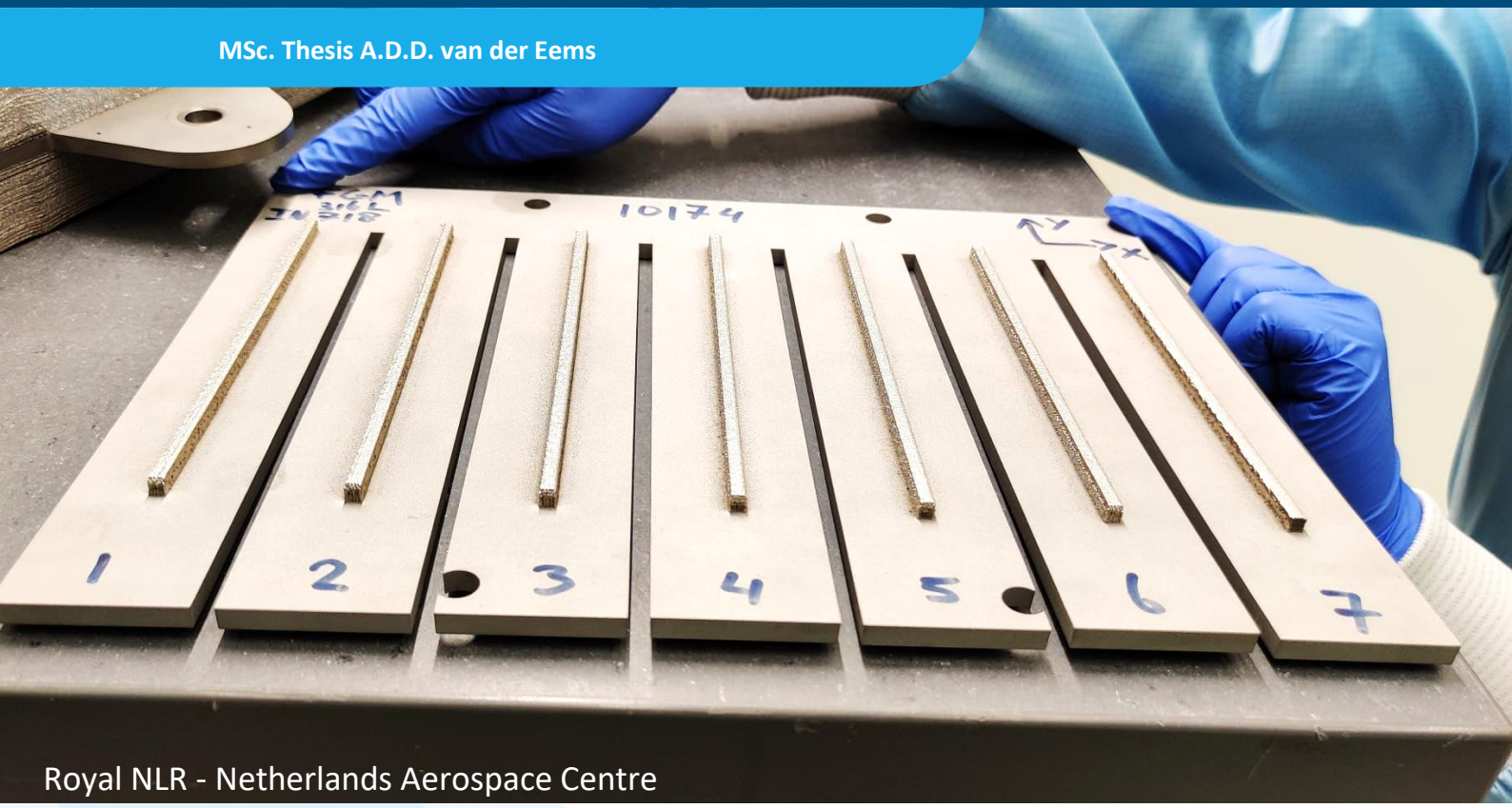

Royal NLR - Netherlands Aerospace Centre

Dedicated to innovation in aerospace

EXECUTIVE SUMMARY

UNCLASSIFIED

In718-SS316L Functionally Graded Materials Produced by Directed Energy Deposition - A Comparative Study on Deformation due to internal stess through Simulation and Experimentation

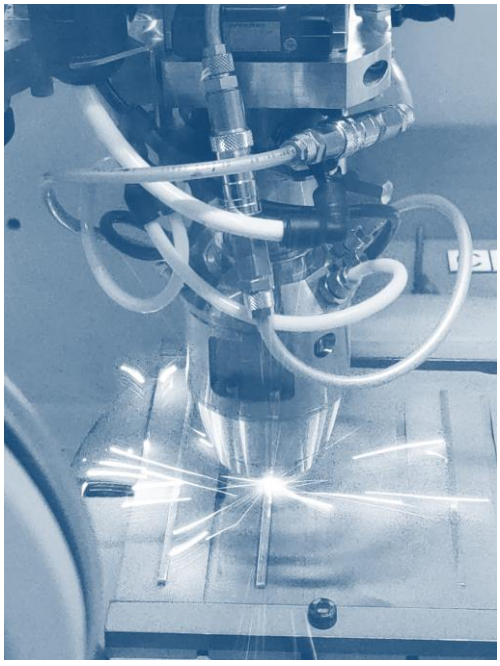

MSc. Thesis on the modelling of different types of DED produced In718-SS316L FGMs without the 25wt% Inconel compositional range, calibrated to an experimental build, and on the validation of deformations in these FGMs.

REPORT NUMBER
NLR-TR-2022-103

AUTHOR
A.D.D. van der Eems

REPORT CLASSIFICATION
COMPANY CONFIDENTIAL

DATE
18-10-2022

KNOWLEDGE AREAS
Computational Mechanics and Simulation Technology
Structures and Manufacturing Technology

DESCRIPTORS
FEM
DED
AM
FGM

Dedicated to innovation in aerospace

COMPANY CONFIDENTIAL

NLR-TR-2022-103 |

In718-SS316L Functionally Graded Materials Produced by Directed Energy Deposition

A Comparative Study on Deformation due to internal stress through Simulation and Experimentation

AUTHOR: A.D.D. van der Eems

Royal NLR – TU Delft – Biomechanical Engineering

CUSTOMER: NLR

TU Delft Delft University of Technology

BioMechanical Engineering

Royal NLR - Netherlands Aerospace Centre

Royal NLR
Anthony Fokkerweg 2
1059 CM Amsterdam, The Netherlands
p) +31 88 511 3113
e) info@nlr.nl i) www.nlr.nl

CUSTOMER	**NLR**
CONTRACT NUMBER	
OWNER	**NLR + partner(s)**
DIVISION NLR	**Aerospace Vehicles**
DISTRIBUTION	**Limited**
CLASSIFICATION OF TITLE	**UNCLASSIFIED**

APPROVED BY :																				
AUTHOR							**REVIEWERS**							**MANAGING DEPARTMENTS**						
A.D.D. van der Eems							Ir. J. Vroon Dr. J. Zhou							AVCE, Royal NLR Biomechanical Engineering, TU Delft						
DATE	18	10	2	0	2	2	DATE							DATE						

Preface

This document is part of my Master of Science graduation thesis. Royal NRL provided the subject of: ”the modeling of Functionally Graded Materials (FGMs) created by DED”. This immediately drew my attention since I have a high affinity with aerospace and additive manufacturing. On the latter, I just successfully finished a course given by Dr. Zhou, who is now my supervisor. The idea of conducting my thesis project on the modeling of residual stress in FGMs came after some initial exploratory literature research, from which I found that most research on FGMs is quite recent and there is a gap to fill in the aspect of material combination as well as in the modeling aspect. Furthermore, my supervisor from Royal NLR Ir. Vroon is very capable of thermomechanical modeling within Abaqus and is willing to assist me to expand his research to FGMs. The objective of this thesis consists of two parts. The first is to create an experimental additively manufactured build, which combines two materials, i.e., stainless steel 316L and Inconel 718. The second is to simulate the DED process and create a model that predicts deformations and thermal history. Conclusions can thereafter be drawn by comparing the experimental results to the model predictions.

First and foremost, I would like to thank my supervisor Ir. Jos Vroon from NLR and my supervisor Dr. Jie Zhou from the TU Delft for their advice and assistance during the writing of my literature review and during the research conducted in my subsequent thesis. Furthermore, I would like to thank the other researchers at NLR for their advice and useful discussions, especially Dr. Maria Luz Montero and Ir. Marc de Smit. Furthermore, special thanks to Joes Lanters who did a prior thesis on FGMs at NLR and gave valuable recommendations and advice for my thesis work. Also, I would like to thank Ir. Timo Osinga for helping me conduct the experiments as he has great skill in operating the DED machinery. Finally, I would like to thank God and my parents, for supporting me not only during my master thesis but my entire study in Delft.

Delft University of Technology A.D.D. van der Eems
October 10, 2022

Abstract

Directed energy deposition (DED) is an additive manufacturing technique that allows for the manufacturing of complex multi-material structures. Such structures composed of Functionally Graded Materials (FGMs) have a lot of potential for the aerospace, medical and nuclear industries. It provides the possibility to combine multiple materials with their specific properties in a single structure. This thesis focusses on the simulation and additive manufacturing of SS316L-IN718 FGMs produced specifically with DED. More specifically, it aims to compare the deformations due to internal/residual stresses after production. Furthermore, 5 types of structures are compared, i.e., an FGM with 10wt% sections, an FGM with 20wt% sections, a bimetal, a pure SS316L build and a pure IN718 build. To decrease microcracks observed in similar literature on these types of FGMs, the compositional range of 25wt% In718 has been omitted in the FGMs and a shorter hatch spacing has been used to decrease porosity.

The simulation overestimated the deformations but the results were mostly congruent with the experimental results, although multiple factors need to be taken into account, such as deformation of the baseplate before printing. Furthermore, the type 10 wt% FGM is more deformed than the type 20wt% FGM, which is more deformed compared to the bimetals. This can be partially attributed to the higher In718 percentage in the FGMs. This finding is congruent with the literature on internal stresses, namely higher internal stresses in FGMs, compared to the corresponding bimetals. It can be attributed to the precipitates and phases that cause a mismatch in volume and therefore internal stresses. These findings go against the common assumption that FGMs with a smooth transition would have low residual stresses.

Finally, concerning the quality of the produced structures, the porosity of the FGMs without the 20-30wt% In718 region was considerably better than the results in the previous study at the Royal NLR. In general the porosities of all the structures range in the 0.01% to 0.05%, which can be considered of very good quality. The few microcracks that were present, all originated at pores but not at random in the matrix. A lower porosity was observed in the 20wt% sectioned FGM as opposed to the 10wt% FGM, as the latter still contained some pores in the 10wt% region. Therefore, it can be concluded that it is best to leave out the whole 10-40wt% region, opposed to just leaving out the 20-30wt% region. Furthermore, the type 10wt% FGM and to a lesser extent the type 20wt% FGM experience higher internal stresses compared to the bimetals. This effect was found in simulation as well as in experimentation.

These findings have implications on future research to be conducted on stainless steel-Inconel FGMs, to improve the quality of the FGMs and reduce internal stresses. Furthermore, the findings on internal stresses are insightful for continued research on FGMs composed of different materials.

Contents

Abbreviations

ACRONYM	DESCRIPTION
ACCREx	Concept generation method: Abstraction, Categorization, Reflection, Reformulation, and Extension of search results
AM	Additive Manufacturing/Additively manufactured
BJ	Binder Jetting
CAD	Computer Aided Design
CBL	Compositional Bond Layer (filler material)
CTE	Coefficient of Thermal Expansion
DED	Directed Energy Deposition
EBAM	Electron Beam Additive Manufacturing
EBTT	Electron Beam Treatment Technologies
FE(M)	Finite Element (Modeling)
FEA	Finite Element Analysis
FGM	Functionally Graded Material
FLIR	Forward Looking InfraRed
GT	Gradual Transition
HIP	Hot Isostatic Pressing
IN718	Inconel superalloy
IPN	Ion Plasma Nitriding
LENS	Laser Engineered Net Shaping
MAMTeC	Metal Additive Manufacturing Technology Centre
MHD	Magnetohydrodynamic
MJ	Material Jetting
PBF	Powder Bed Fusion
Royal NLR	Netherlands Aerospace Centre / Dutch aerospace institute
SLM	Selective Laser Melting
SS316L	Stainless Steel alloy
ST	Step Transition
TCP	Topologically Close Packed
TFD	Thin Film Deposition
UTS	Ultimate Tensile Strength
VC	Vanadium Carbide
VPP	Vat Photopolymerization
WAAM	Wire Arc Additive Manufacturing
3mE	Mechanical, Maritime and Materials Engineering (a faculty of the TU Delft)

1 Introduction

Functionally graded materials (FGMs) are a new development in materials science, closely related to the recent developments in additive manufacturing (AM) technology. these developments provide the possibility to not only make complex shapes, but also change materials while the structure is being built up. This thesis focusses on AM and modeling of FGMs consisting of SS316L and In718 without the 25wt% Inconel range. The used production method is Directed Energy Deposition, hereafter abbreviated as DED. For the simulation, Abaqus 2021 software was used. In this introduction, the history of material development is briefly described and the place of FGMs herein. Thereafter, an explanation of DED is given. The next section will discuss the applications and opportunities. The last two sections will present the research questions and an outline of the structure of this thesis.

1.1 History

The development of materials started in the Bronze Age (4000 BC), see Figure 1, when the first alloy was created by combining copper and tin. This alloy named bronze was much stronger than its individual constituents. Development continued in the Iron Age on quenching and tempering techniques to prepare even stronger and more versatile iron. Presently, it is possible to purify metals to create new and even better (micro)alloys that can also be tuned to meet specific requirements. The latest in material developments are composites consisting of several different constituents. These distinct combinations give rise to very hard and wear-resistant materials. The structures created with all the previously mentioned materials are usually made out of a single alloy or composite throughout the whole part. In the last decade however, huge strides have been made in developing FGMs. This is possible, due to big improvements in AM technologies, in particular DED and Powder Bed Fusion (PBF), providing new possibilities for combining different metals [1].
AM is a widely used production method with growing popularity across a broad range of fields. One of its biggest advantages is its possibility to create complex structures directly from Computer-Aided Design (CAD), which gives possibilities to quickly realize designs that would otherwise be impossible to create.

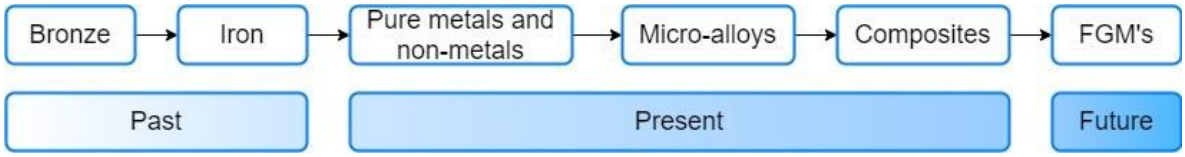

Figure 1. Timeline of material development from bronze to FGMs [1]

AM has already proved useful in the biomedical sector where it is used to create implants personally fitted to the patient. AM is furthermore being studied intensively in the aerospace sector for its possibilities to create complex structures. Winding cooling ducts are a good example, as these structures are impossible to create with conventional production methods. Another example are the complex topology-optimized structures that can now be manufactured directly from CAD files, whereas before it was impossible to create these structures at all. An example of such a structure is shown in Figure 2 [2].

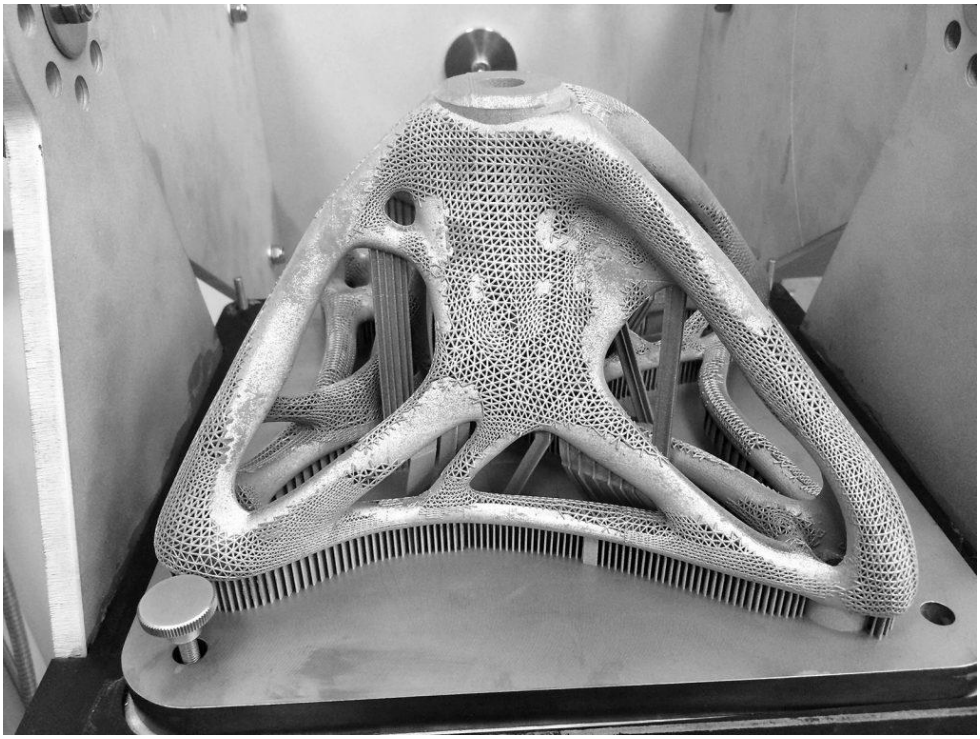

Figure 2. AM titanium demonstrator of a spider bracket that functions as a connection between the corners of architectural glass panels used in atria and floor-to-ceiling glazing. Note the complexity of the solid mesh and its lattice structures [2].

AM can also be used to combine multiple metals in one structure. This is done to create parts with different properties at different locations ranging through the structure (Functionally Graded). Such properties can be strength, heat resistance, corrosion resistance or magnetic susceptibility. The possibilities are limitless ranging from wear-resistant bearings integrated into lightweight wings, to turbine blades with high thermal resistance and anti-oxidation properties at the high-temperature side and with high mechanical strength and toughness required at the low-temperature side [1]. For the latter, a composite FGM can be created, such as tungsten in an aluminium matrix [3], where the tungsten increases the heat resistance and at the cooler locations aluminium gives a good strength to weight ratio.

The performance of a structure is closely related to structural optimization, which can be divided into size, shape, topology and material optimization using the ACCREx method (abstraction, categorization, reflection, reformulation, and extension of search results) [4]. Up until now, the
focus has been on the optimization of the shape of the object in order to meet conflicting requirements, often on strength and weight [5].

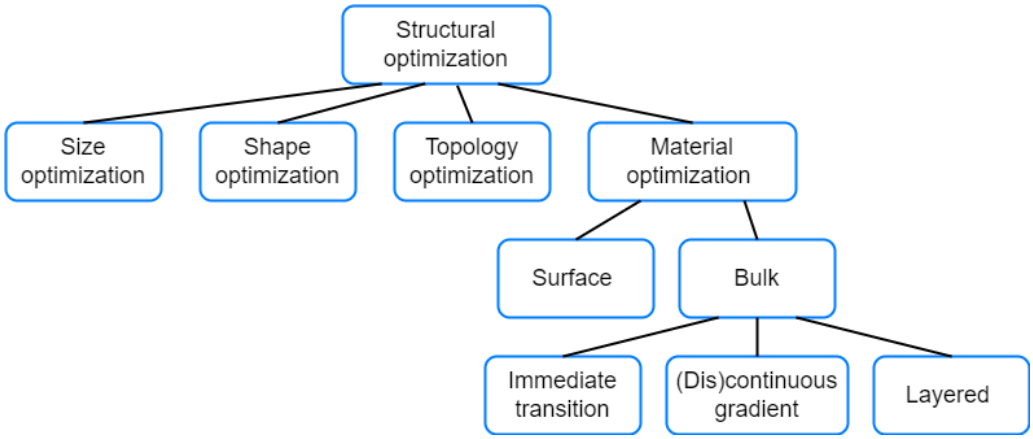

Figure 3. Classification of structural optimization and material optimization by implementation of the ACCREx method [4], [5].

With AM, a new variable can now be added to structural optimization, which is material, see Figure 3. This can be divided into two categories. First, surface treatment, which can be achieved with DED [6], but also by using many other techniques, such as thin film deposition (TFD), ion plasma nitriding (IPN) or electron-beam treatment technologies (EBTT) [7]. Second bulk, which is the focus of this report, in which the material is changed over its entire length. The manner of material transition can be divided into immediate transition, (dis)continuous gradient and layered gradient, which will be discussed in section 2.2. This new method of adding material as a variable to structural optimization, has recently been studied by several research groups. For example, a virtual element analysis looked at hyperelastic materials under large deformations [8]. Another study looked at single variable-based multi-material structural optimization [9]. However, these are all still theoretical simulations and materially topology-optimized objects are yet to be physically printed and tested.

The Metal Additive Manufacturing Technology Centre (MAMTeC) [10], established within the Royal Netherlands Aerospace Centre (NLR) [11], recognized the potential of FGMs. Within a four-year AM development program dedicated to investigating the possibilities of producing AM, a special lab was created for FGMs.
After some preliminary research on producing a bimetal with Selective Laser Melting (SLM) [12], NLR purchased a laser powder-blown DED machine, BeAM M400 in the summer of 2020. This machine was in theory capable of creating FGMs as it is equipped with multiple hoppers. However, during personnel training, it became clear that the machine was not capable of switching materials during one build job. Therefore, the thesis of J. Lanters was dedicated to making the production of FGMs technically feasible and to analysing mass-flow. This research resulted in the production of some promising SS316L-In718 FGM structures of reasonable quality, with low porosity and a few microcracks in different regions of the builds. Meanwhile, the modeling department of the Royal NLR has made large strives in the simulation of internal stresses in AM structures and wishes to expand this to FGMs. The thesis presented here, is a continuation of both research areas. It aims to improve the build quality of the SS316L-In718 FGMs, as well as improving the predictability of deformations with simulations, which can be calibrated and validated with the experimental AM FGM structures.

1.2 Directed Energy Deposition

AM technology can be divided into seven main production techniques: Directed Energy Deposition (DED), Vat Photopolymerization (VPP), Powder Bed Fusion (PBF), Material extrusion, Material Jetting (MJ), Binder Jetting (BJ) and Sheet Lamination [13],[14],[15]. In principle, all of the above can be used to create an FGM, but Powder Bed Fusion and DED are most popular. The advantage of DED over PBF in its suitability for the production of FGMs is the possibility to change the material composition through the nozzle at any time, which is more convenient, compared to the layer by layer method of PBF. This is the main reason why the Dutch Aerospace Centre chose to acquire the BEAM M400 machine. DED can be divided into two main types.

The first is the Wire Arc Additive Manufacturing (WAAM) process. This method feeds the material as a wire or filament and a welding arc melts it. The second method is Laser Powder-Blown DED or Laser Engineered Net Shaping (LENS). This process is incorporated into the BEAM M400 machine. It works as follows: the DED process starts with a laser beam focused on the surface of a substrate, creating a melt pool. Simultaneously powder is blown into this melt pool using inert gas to build a new layer.

The powder stream and laser spot can be combined in several nozzle configurations, as illustrated in Figure 4. These configurations can be categorized into off-axis / lateral feed nozzles (a) and coaxial nozzles (b-e) [16]. The BEAM M400 has a nozzle configuration as illustrated in (b), this will be further discussed in section 3.1.

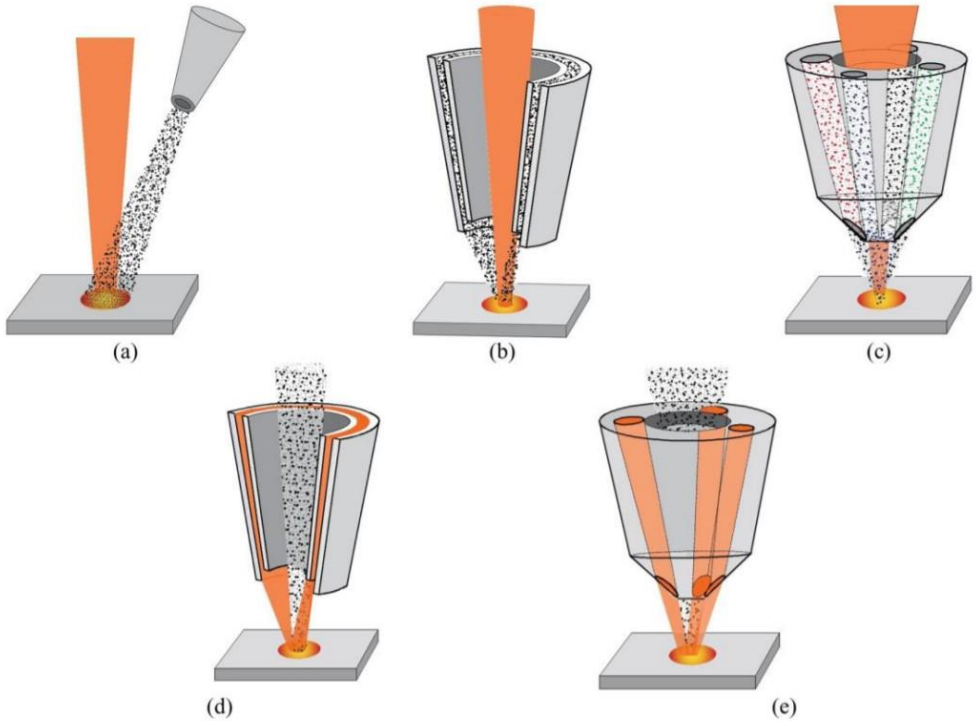

Figure 4. Orientation of powder feedstock and laser beam for (a) off-axis, (b) continuous coaxial, (c) discrete coaxial, (d) annular, and (e) discrete annular laser beam nozzles (the respective positions of laser and powder stream are marked by red and grey colours) [13].

The biggest threshold in AM, also called three-dimensional printing (3D printing), is the imperfections still present in the material matrix. These imperfections in AM arise from: unmolten particles, internal stresses, microcracks, air gaps and heat affected areas. This is a challenge in, for example aerospace, since (unpredictable) imperfections are not acceptable in critically designed lightweight structures. The use of FGMs comes with a few additional material challenges, such as

the formation of intermetallics and constitutional super-cooling, but also new possibilities that will be discussed in the next section.

1.3 Applications and opportunities

As mentioned in section 1.1, an FGM can be manufactured to achieve a trade-off between thermal resistance and strength, as was done with tungsten in an aluminium matrix [3]. This creates the opportunity to optimize the structure for stability and durability. However, an FGM is not easy to prepare, because the more dissimilar the thermal properties of the materials, the more difficult the fusibility is between the materials, because of solidification cracking. For this reason, the fusion of titanium with Inconel or stainless steel for example, is quite hard. Another opportunity for an FGM is to obtain a transition from a non-magnetic material to magnetic material, this has actually already been accomplished with a stainless tube structure transitioning from 316L stainless steel (SS316L) to SS430L [17]. Such an FGM is useful for controlling magnetism which finds applications in data storage [18] and MRI technology [19]. Furthermore, in the biomedical field, FGMs offer unprecedented opportunities for advanced orthopaedic treatments by combining Ti-, Mg-, and Fe-based bio-materials in, for example, bone substitution [20]. Finally, the transition of nickel-alloys to stainless steel is widely used in the nuclear and power industry. This is due to the requirements of high temperature corrosion resistance and wear resistance, which nickel-alloys excel at, combined with the reduction of costs with the use of stainless steel in less demanding areas [21]. More details on the last type of FGMs will be discussed in the next chapter.

1.4 Research questions

After an extensive literature review and on the basis of the possibilities at the NLR, the following research questions were set-out for this thesis project.

1) Can the deformations of FGMs be accurately predicted by finite element (FE) simulations in Abaqus software?
2) Does the step size in the composition of FGMs have an effect on the outcome of simulations in Abaqus, concerning internal stresses and deformations?
3) Does the step size in the composition of FGMs have an effect on internal stresses and deformations in an experimental DED build of SS316L-In718 FGMs (without the 25wt% Inconel range)?
4) Does the quality of the FGM structures improve by leaving out the 25wt% Inconel range in terms of less microcracking?
5) Does the porosity decrease with a significantly decreased hatch spacing.

1.5 Thesis structure

The thesis will continue in Chapter 2 with the presentation of the findings of the literature review on the FGMs produced by DED and thereafter the state-of-the-art of thermomechanical simulation of AM structures and FGM structures.
Chapter 3 describes the Methods and Design of Experiment, which have been applied in the production of the experimental FGM structures. The second part will elaborate again on the simulations performed.

Chapter 4 will elaborate on the results of the experiments which will start with mass flow calibrations and thereafter the results of the simulations.
Furthermore, the deformations found in the experiment and in the simulations, for different types of FGMs, will be compared. Differences and their possible causes will be discussed.
Thereafter, Chapter 5 will summarize the conclusions of this thesis work. Finally, in Chapter 6 recommendations for future research are proposed.

2 State of the art

In this chapter the state of the art is discussed by first addressing the most popular metal combinations and thereafter focussing on the combination of SS316L and In718, which is the focus of this thesis. The second section discusses the different approaches to building up an object. The final section concerns the major challenges in DED.

Google Scholar was used as the main search engine as it provided far more complete search results than other search engines, such as Scopus. Google Scholar would present, for the search inquiry FGM DED, 1790 results, compared to 17 at Scopus. FGM and DED were the only global inclusion criteria used. To find the combinations that received most interest, first a lot of literature reviews have been consulted. Thereafter, in snowball fashion, these combinations received their own dedicated search criteria, such as AM, FGM, Ti-6Al-4V and Inconel. For more information on the other combinations please see the literature review prior to this thesis.

2.1 Metal AM combinations

A wide range of material combinations has been studied, as shown in Figure 5. The most popular combinations are those with the titanium alloy Ti-6Al-4V and also pure titanium for their high strength to density ratios, good thermal properties and corrosion resistance, making these materials very desired in aerospace. Titanium is furthermore bio-compatible, a requirement for many biomedical applications, and it has good producibility via 3D printing. Research has been conducted on combining titanium with stainless steel [22], [23], aluminium [24]-[30] or Inconel [6], [31].
Another interesting material combination consists of aluminium-bronze with stainless steel [32],[33],[34]. This finds possible applications in the aerospace electronics and nuclear industries, due to the combination of the heat conductivity, oxidation resistance and lubricity of aluminium-bronze and the high mechanical strength, corrosion and creep resistance of stainless steel. Other popular material combinations are Inconel, particularly IN625 or IN718, with stainless steels, such as SS316L [35] or SS304 [35]. In the next subsection, the combination of stainless steel and Inconel will be discussed, which is the focus of this thesis.

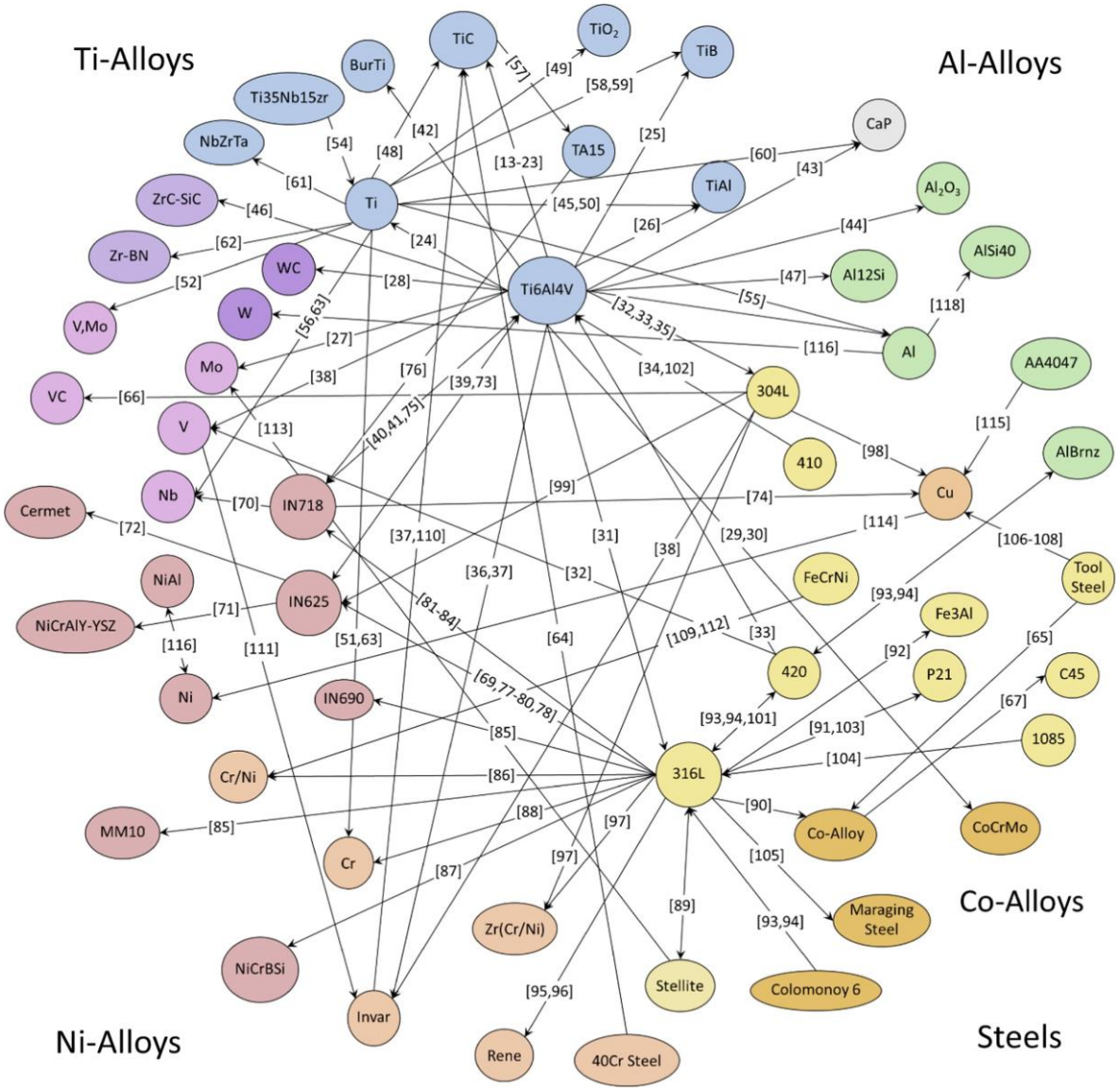

Figure 5. Visual representation of published studies on bimetallic structures and FGMs produced with the DED technique. The direction of fabrication is indicated by the arrow. Each number references a corresponding paper cited in Feenstra et al [36].

2.1.1 Stainless steel - Inconel combination

Stainless steel and Inconel make an interesting combination, since the Inconel superalloy has good mechanical properties at high temperatures (up to 650°). Furthermore, nickel along with other alloying elements, such as Cr, B, Si, Fe and C delivers excellent performance in wear and corrosive environments [21]. But Inconel lacks in bonding capability due to the generation of Nb- and Mo-rich compounds, which can cause hot cracking in the heat-affected zone (HAZ). Cracking interrupts the diffusion and welding with other substances. Stainless steel, on the other hand, is a suitable supportive and structural material, because it has a high affinity for adjacent substances with similar phases due to the high solubility of its principal constituents (Fe, Cr, and Ni), even towards the precipitate constituents. Furthermore, it has a high melting temperature, but it lacks the excellent creep rupture strength seen in Inconel. Finally, stainless steels in their austenitic structure possess high corrosion resistance. Therefore, by combining Inconel and stainless steel, an

FGM can be created with sufficient joinability and on both sides good corrosion resistance. Furthermore, an FGM of SS-Inconel creates the possibility to gradually trade off the good mechanical properties, high creep strength and chemical resistance of Inconel to the cheaper, more bonding-capable stainless steel [35], [36].

The fusion of stainless steel and Inconel comes with some challenges. The main challenge concerns the microcracks in the specific composition of around 25wt% Inconel. This is due to multiple reasons, such as solidification behaviour, a columnar-to-equiaxial phase transition, ceramic oxides such as Al_2O_3 and TiO_2 and the formation of intermetallics such as $(Ni,Cr,Fe)_2(Nb,Mo,Ti)$, δ-Ni_3Nb and γ-Ni_3Al. Challenges found in the literature and in a previous study by Royal NLR will be further discussed in subchapter 2.3. A few recent studies have succeeded in creating defect-free FGMs of SS316L combined with IN718 [35] or SS316L with IN625 [37].

2.2 Build methods

An important part of the build strategy is the build method. The joining of the metals and the consequent material phases that are produced, depend on it. Five build strategies can be distinguished: Direct Joining, Alternate Switching, Intermediate Section, Gradient path, and Compositional Bond Layer, see Figure 6 [16], [38]. The first method of directly joining two metals also known as creating a bimetal can result in a lot of residual stress, depending on the dissimilar coefficients of thermal expansion (CTEs), solidification cracking and brittle intermetallic formation [36]. The second approach of alternate switching is similar, but the layers are now successively alternated between two materials. Recent studies have shown that because of melt pool mixing, immediate transitions can be made more gradual, similar to gradient transitions [39], which are the third method and fourth method. In these methods, the material composition is gradually changed, which requires more effort, because powder mixing equipment is necessary, but it has the advantage that the composition is not too dependent on melt pool mixing. This can be done discontinuously via intermediate sections or with a continuous gradient path. The effects of interlayers and scanning strategies on residual stress have been studied by Woo et al., they found that the gradual transitions reduced the issues of residual stress and lattice mismatch [40]. The final method is the use of the compositional bond layer or filler-material to bond two metals together, which will be further discussed in 3.1.1.

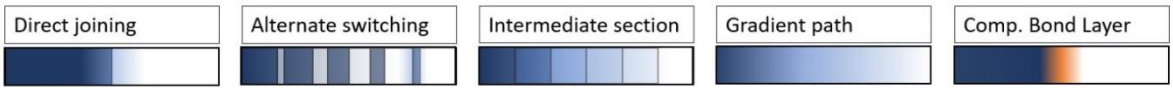

Figure 6. Build methods to produce an FGM transitioning the composition from one metal to another [16].

2.3 Challenges and respective approaches

Research on FGMs produced with DED faces a few challenges. These are intermetallic phases, subsequent microcracks and internal stresses. The first section 2.3.1 will go into detail on intermetallic phases and microcracks. The second section 2.3.2 will elaborate on internal stresses.

2.3.1 Intermetallic phases and microcracks

During the DED process difficult phases may occur, such as the formation of laves and σ-phases during the AM of Inconel, which have topologically close-packed crystal (TCP) structures, providing little strengthening effect. The TCP structured phases are also brittle and furthermore deplete the microstructure of useful elements. However, as for Inconel, these detrimental effects can be negated with the addition of rhenium, which increases the strengthening effect of the TCP phases [41].

When combining two different metals, new material phases may arise with a high percentage of intermetallics. Intermetallics are generally very hard and brittle. This can lead to micro-cracks via internal stress or bad solidification behaviour. This phenomenon is encountered in multiple studies on the combination of stainless steel and Inconel. The formation of micro-cracks was frequently encountered around the constitution of around 25 wt% Inconel [35], [37]. An experimental study at NLR, conducted by Lanters, focussed on an FGM of SS316L to IN718 showed similar cracks in the same compositional range of 25 wt% Inconel [16]. This can be clearly seen in Figure 7 in the lower part of the gradient zone.

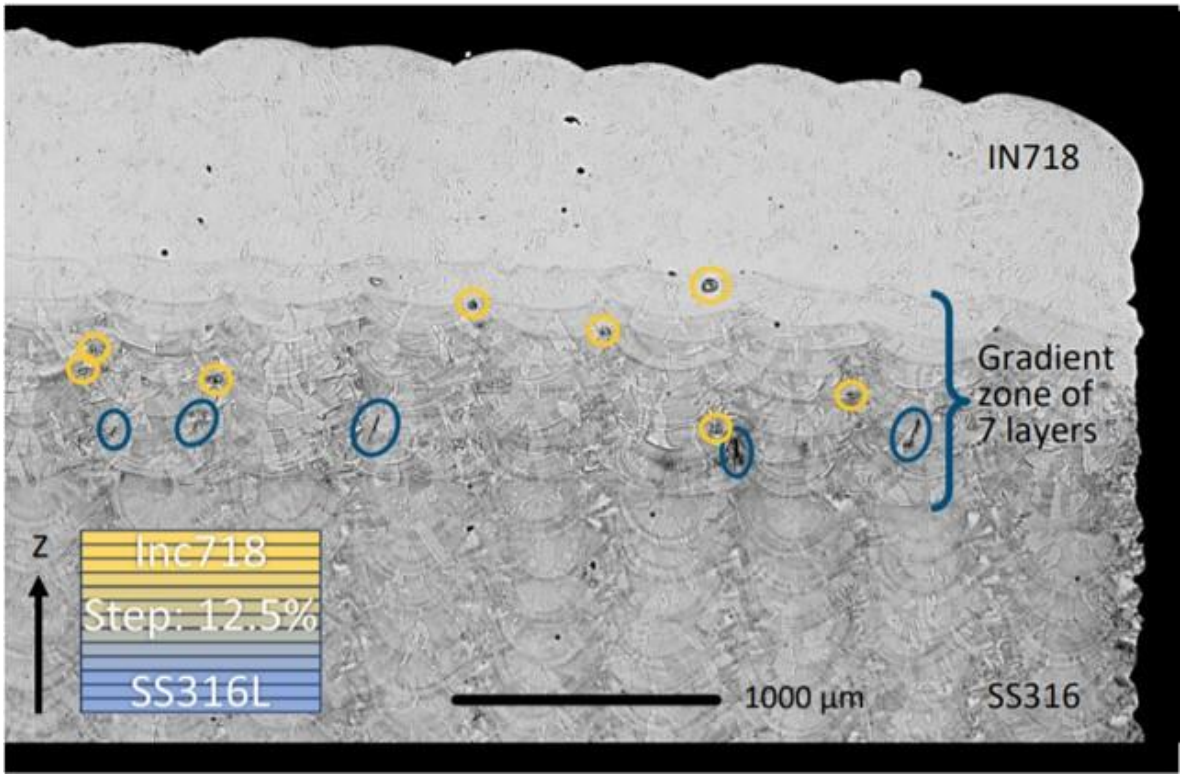

Figure 7. Defects found in the FGM transitioning from SS316L to IN718. In the upper half unmolten particles can be detected and in the lower part around the compositional range of 25wt% Inconel microcracks are spotted [16].

The occurrence of microcracks can be attributed to a few factors. The first is the mechanism of constitutional super-cooling, which is the solidification behaviour; this can be troublesome if the arising new phase has a different melting temperature from the starting components. The second cause of microcracks is the columnar-to-equiaxial phase transition, which occurs due to the changing material composition, respectively from IN718 to SS316L. At the interfaces of these phase transitions, thermal and residual stresses are concentrated, which causes the formation of microcracks [35]. It is therefore important to consider the material transition route.

Apart from the detrimental effects of microcracks on the structural integrity, the transition region also suffers from a loss in hardness, according to a study conducted by Shen et al [37]. This study focused on a similar FGM of SS316L and Inconel 625. They found a drop in micro-hardness in the same difficult 25wt% Inconel range, see Figure 8. Kim et al. also tested the cross-sectional hardness of their two FGMs both consisting of a transition of IN718 to SS316L by 10 wt% increments, but one FGM skipped the troublesome 20 wt% and 30 wt% Inconel stages. They demonstrated that leaving out the 20 wt% and 30 wt% ranges circumvented the drop in hardness, see Figure 9. Kim et al. were however not sure what caused this drop in hardness.

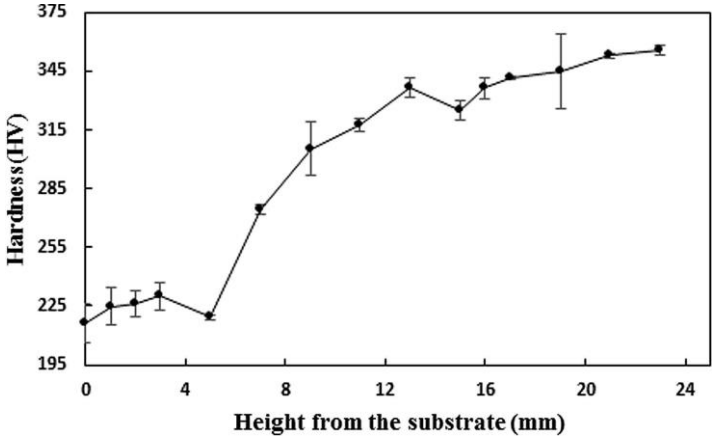

Figure 8. Micro-hardness distribution along the deposition direction for an FGM consisting of SS316L to Inconel 625, from Chen et al [37]. Note the drop in hardness around the 25wt% Inconel range.

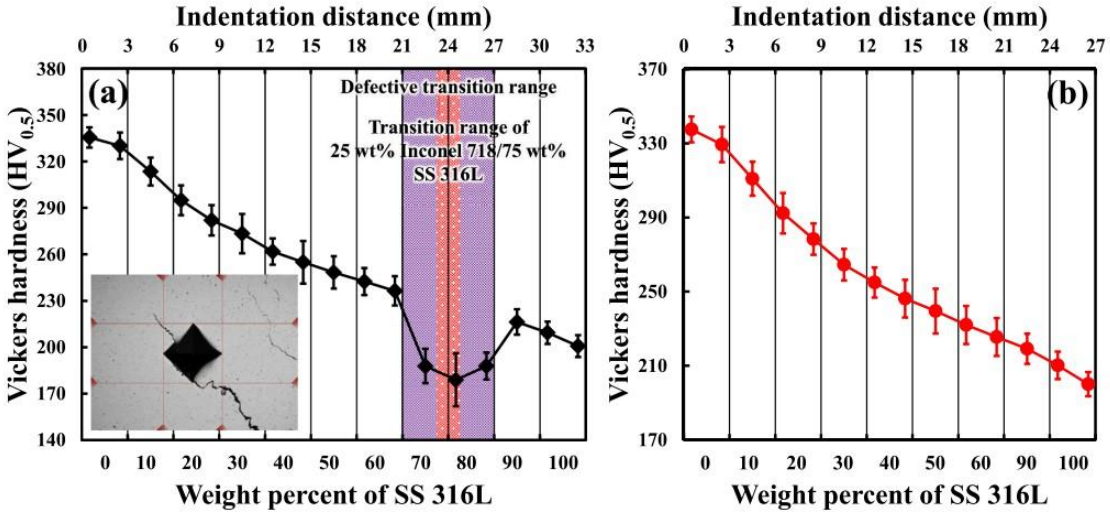

Figure 9. (a) Micro-hardness distribution along the deposition direction for an FGM consisting of SS316L and Inconel 718. (b) The same FGM but without the defective transition range of 25wt% Inconel. From Kim et al [35].

2.3.2 Internal stresses

Two major problems are occurring during multi-metal AM in the NLR experiment with SS316L and IN718 as well as the Fe-Al experiments. Firstly, micro-cracks caused by intermetallics and excessive melting, respectively. The second problem, especially experienced in the SS316L-IN718 combination, are non-optimized process parameters causing a lack

of melting and resulting in unmolten particles inside the metal. However, successes have already been achieved using a combination of SS316L-In625 by Chen et al. [37] and SS316L-In718 by Kim et al [35]. The latter also found defects in the 25 wt% Inconel 718 to 75 wt% stainless steel 316L region and avoided this problem by skipping the 20% and 30% Inconel layers in a 10% step graded structure from Inconel to stainless steel. By doing so, it was able to create a defect-free FGM.

Although defect-free FGMs have already been created, internal stress is still very prevalent in FGMs due to the process of DED that gives rise to a lot of thermal stress. Furthermore, the discrepancy in CTE between the two materials compounds even more stress. Internal stress can be calculated according to Eq. *(1*:

$$H(\sigma) = \frac{E\Delta\alpha\Delta T}{1-\mu}$$

where H(σ) is the internal stress, E is the Young's modulus, $\Delta\alpha$ is the thermal coefficient difference between two layers, ΔT is the temperature difference between the melt pool and the substrate, and μ is the Poisson's ratio. According to this equation, $\Delta\alpha$ and ΔT mainly determine the amount of internal stress.

The influences of defects and internal stress on each other are something to keep in mind, since internal stress can be absorbed by defects in the material. This results in an affected total deformation, thus not providing accurate deformations to compare to simulations. To consider the effect of defects, the defects are categorized into three types. The first two types are horizontal microcracks and vertical microcracks and span the range of orientations between them. The final type of defect is circle-shaped and represents air gaps or unmolten particles. Internal stress has a correlation with micro-cracks, depending on the orientation and whether it is under compression or tension. This is illustrated in Figure 10, where the internal stress is assumed as a pure bending moment on a beam. This is a good approximation for an FGM since most internal stress will be caused by a discrepancy in CTE, resulting in a bending moment. In this case, under tension at the top half and under compression at the lower half. A lateral micro-crack, shown to the left in the illustration, will only be affected by longitudinal stress if this is under compression, so in the lower half. Lateral stress would also pull open the crack, but this is not apparent in the bending moment and thus not illustrated. Air gaps, illustrated to the right of the horizontal microcracks, will always be affected by internal stress, independent of the orientation of the stress. In the middle, a microcrack is shown along the centre-line. Since the internal stress is assumed to be bending stress, there is a transition from tension to compression, as is indicated by the arrows in Figure 10b. Therefore, the stress here is negligible. To the right, vertical microcracks are shown, in this case, tension can open up the crack so only micro-cracks in the top half are affected.

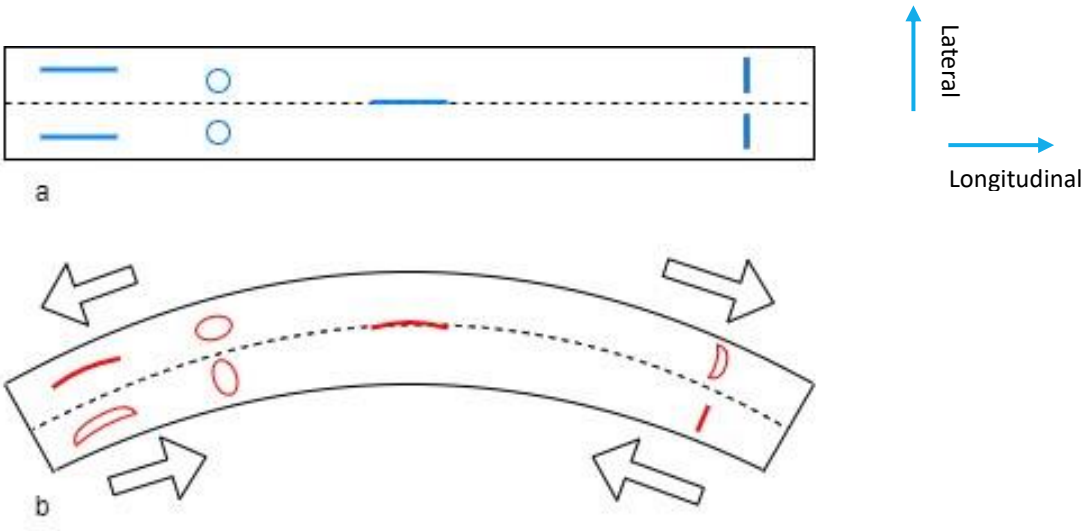

Figure 10. Illustration of the correlation between stress and defects in an object. (a) unstressed FGM beam with three types of defects. From left to right: horizontal microcracks, air-gaps or unmolten particle and vertical microcracks. (b) Effects of internal stress on the different types of defects. The direction of the stress is indicated by the arrows. Note that the microcracks are impacted by the stress depending on their location and orientation.

Respective approaches to reducing internal stresses are the use of synchronous or post heat treatments or the synchronous application of a magnetic field on the meltpool [28].

2.4 Modeling

Metal AM is an expensive process, the cost of professional DED equipment runs into the millions, therefore its printing time is valuable. Modeling can take on a significant part of experimental work to predict temperature evolution, structural response (distortions), material behaviour and residual stresses during and after the AM process. The acquired results can be used for parameter optimization or research [43]. The estimation of material properties will be discussed first in paragraph 2.4.1. Thereafter, the modeling of FGMs with the use of FEM software is discussed in paragraph 2.4.2.

2.4.1 Intermediate material property estimation

The most common type of FGM is the intermediate section type, see Figure 6. In other words the FGM is divided into segments. Each of these segments is comprised of a specific incremental composition. These compositions are often quite unique and specific material properties might be hard to find in the literature or with compositional route modeling. To still be able to model FGMs, material properties are estimated using functions, with the power-law function being most common [44]-[47], thereafter the Mori-Tanaka scheme [48]. Both can be adjusted to fit the material properties in the FGM very well. The Mori-Tanaka scheme is slightly more precise but the power-law is easier to adjust by just varying the power law index p and is therefore the most popular option. In these functions, the material properties are graded across the thickness (h) of an FGM structure from bottom ($z= -h/2$) to top ($z = h/2$) by changing the volume fraction (V_f), see Eq. 2. The power law functions to estimate the position-dependent variation of material property across the thickness direction are shown in Eqs. 3, 4 and 5 for, respectively, modulus of elasticity (E), thermal coefficient of expansion(α) and thermal conductivity(k). The subscripts c and m represent the two materials. P

represents the power law index or material property gradient index (p) which can also be varied to calibrate to experimental results.

$$V_f = \frac{z}{h} + \frac{1}{2} \tag{2}$$

$$E_z = E_m + (E_c - E_m)V_{fp} \tag{3}$$

$$\alpha = \alpha_m + (\alpha_c - \alpha_m)V_f^p \tag{4}$$

$$k_z = k_m + (k_c - k_m)V_{fp} \tag{5}$$

2.4.2 Finite Element Analysis of DED

Once the volume fractions are captured experimentally or designed via compositional route software, the data can be fitted to different types of formulas to model the behaviour of the FGM component. This type of analysis is usually done via Finite Element Method (FEM), which is a popular modeling technique to design structures and predict their mechanical and physical behaviour. It operates by splitting up the structure into small elements and doing computations on them individually. The use of FEM has proven invaluable for designing in engineering and is also very useful for the modeling of AM structures and FGMs.

2.4.2.1 Thermo-mechanical analysis

Fundamental research has been conducted on different types of AM methods. One study, conducted by Ahmad et al. wrote a procedure of numerical simulation on the WAAM or Electron Beam Additive Manufacturing (EBAM) process [49], a subtype of DED. The structure of interest was a rectangular beam fixated on a baseplate. The focus lay on distortion and residual stress analysis with two types of heat source models, namely the rectangular heat source and Goldak's double ellipsoid. These models are able to take the repetitive heating and cooling cycles during the WAAM process into account. The results, namely the distorted shapes of these two models, are very similar. As can be seen in Figure 11, where the displacements in the Y-direction and the angular distortion characteristics of the WAAM model are displayed to the left for the rectangular ellipse (a), (c) and to the right for the Goldak's double ellipsoid (b), (d). However, they found that deviations of the residual stresses do depend on the transient temperature distribution during the cooling phase, the applied forces on the WAAM structure after the cooling process and the removal of the substrate/table. They concluded that crucial information on deformations was acquired through simulation, which could find uses as a design phase planning tool prior to the actual experimental process.

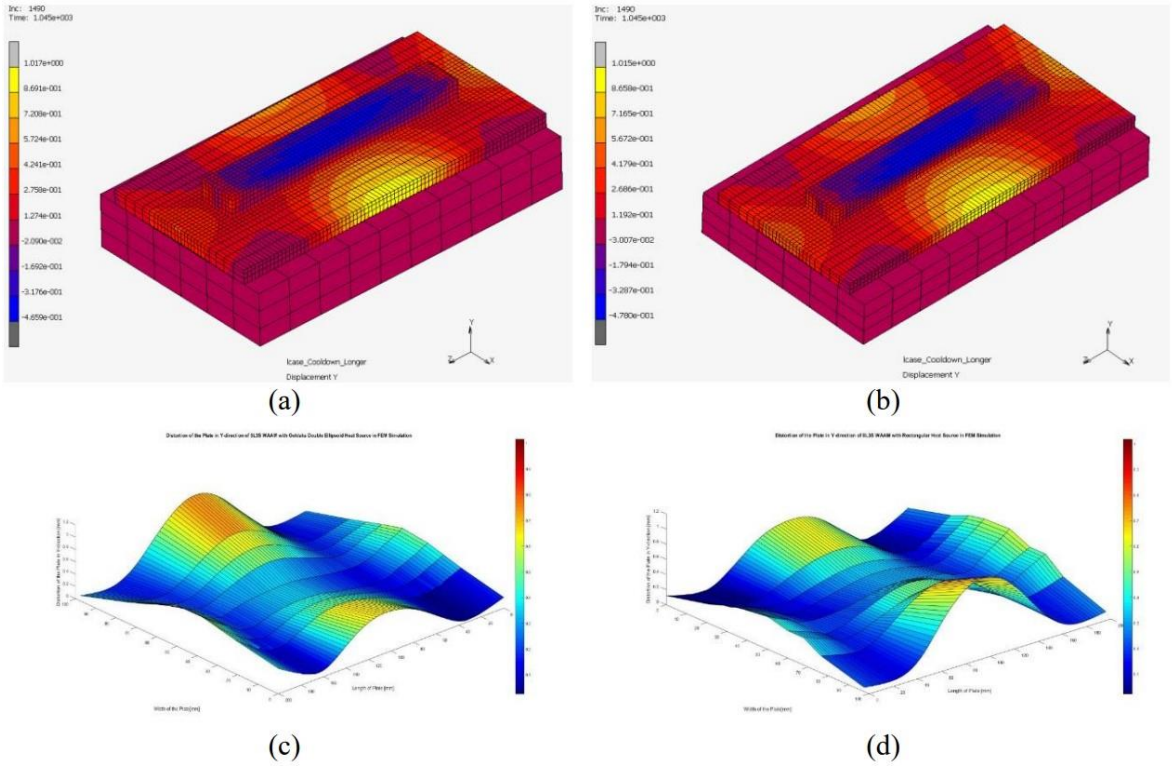

Figure 11. Displacements in Y-direction displayed for the two heat source models: (a) Rectangular (b) Goldak's double ellipse. The angular distortion characteristics of the WAAM model for again two different types of heat sources (c) Rectangular (d) Goldak's double ellipse, from Ahmad et al. [49].

Finite Element Analysis (FEA) applied to the Laser Engineered Net Shaping (LENS) process is another possibility. An analysis method created by Stender et al. incorporates a multistep FEA workflow to show the thermal and mechanical responses in LENS manufactured structures, specifically with SS304L [50]. Their method works as follows: a thermal element activation scheme captures the material deposition process at each time step. On the activated elements, with their associated geometry, first a thermal analysis is conducted, considering heat flow due to radiation, convection, and conduction. Thereafter a mechanical analysis is conducted to find the resulting stresses, displacements and material property evolution. They validated their model by comparing it to experimental builds produced at the Sandia National Laboratories (Albuquerque, NM). The results from the modeling and experimental data show general agreement in the evolved residual stress, dislocation density distributions at the end of the build, as well as the thermal profiles during manufacturing. A comparison of the normal beam computational model and corresponding Forward-Looking InfraRed (FLIR) images from the experimental build can be found in Figure 12. Similar positive results were found by Yang et al and Kiran et al. in their experimental validations of LENS modeling. Yang et al. focused on a LENS Ti-6Al-4V build and validated their FEM model with experimental results acquired with a 3D laser scanner and thermocouples applied to top and bottom [51]. The study of Kiran et al. focused on SS316L and used the 3DExperience finite element analysis software [52]. In contrast to Stender et al. both of the modeling approaches first applied experimental calibration. It is noteworthy that an extensive library of mechanical and microstructural history is experimentally available for the behaviour of traditionally manufactured materials [53], [54]. However, such a database does not exist for LENS manufacturing, although it is necessary to have calibration results acquired beforehand or available. Simulation methods could be attractive to fill this gap until such a database is created by extensive experimental testing [50]. It is however questionable how valuable modeling would be without the calibration, as was shown to be a necessity in the research of Yang et al. and Kiran et al. Furthermore, simulation of the LENS process is still very time-consuming. If this

could be reduced, it would make the widespread implementation possible, to provide information during manufacturing and to assist real-time decision making [50].

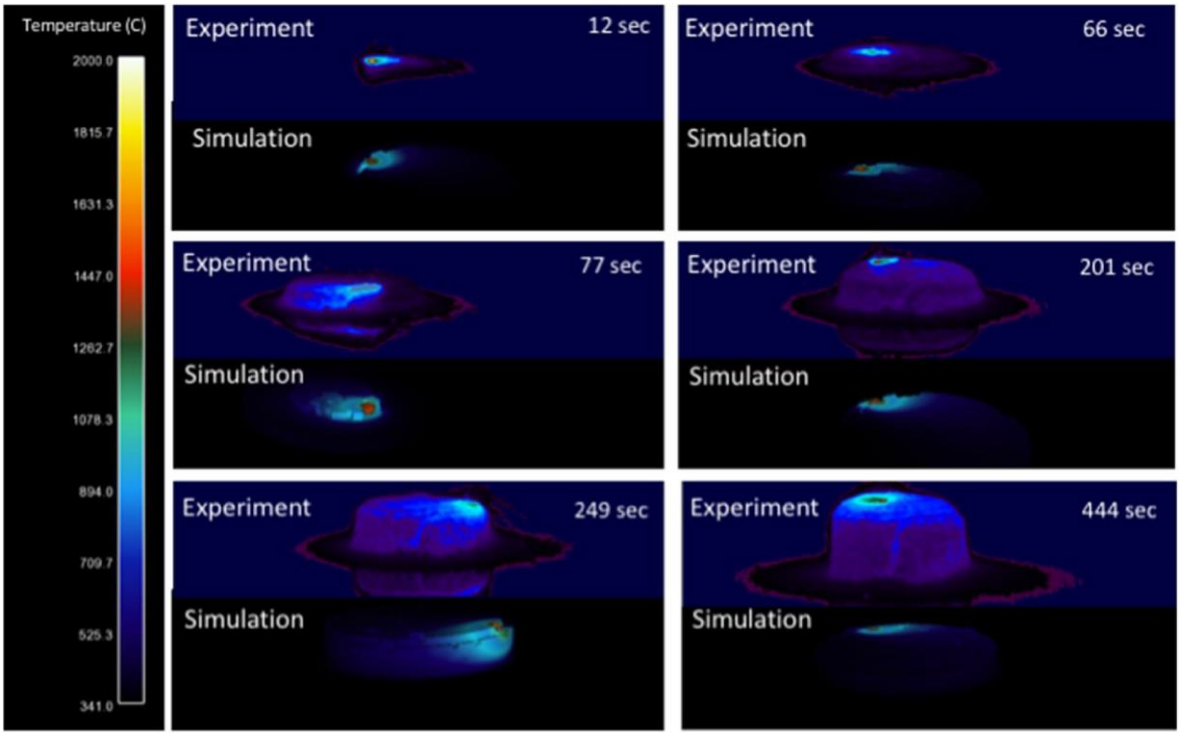

Figure 12. Comparison of temperature profiles of the normal beam computational model and corresponding FLIR images from the experimental build from Sandia National Laboratories requested by Stender et al. [50].

Another important aspect in the modeling of DED is the method of material deposition modelling. Two deposition models exist: the first uses quiet element; these elements are present in the analysis, even before being deposited, but only specific properties are assigned and so the analysis is not affected. The second approach uses inactive elements; in this case, the elements are not included in the analysis until the corresponding material has been added. The inactive approach is less accurate but also less computationally intensive. A new hybrid inactive/quiet element method is proposed by Michaleris [55]. The elements in this approach are initially inactive and are switched to quiet on a layer-by-layer basis. This approach reduces the computation time while maintaining equivalent results [55].

2.4.2.2 Multi-physics analysis

Thermomechanical models have proven to be a valuable tool for the prediction of residual stresses and can be used to model phase transformations. Multi-physics models, on the other hand, cover more physical phenomena, e.g., surface tension, the Marangoni effect, the recoil pressure, and evaporation, and are therefore capable of accurately predicting melt pool shape and sizes for both the PBF and DED processes and can furthermore predict lack of fusion and keyhole-induced pores. They have proven to be in reasonable agreement with experimental observations. However, substantial calibration is required due to the extra uncertainties that come with the added physics. Furthermore, a large drawback in multi-physics modeling of AM is its computational cost. This is far higher than for thermomechanical models. For PBF, there is at this moment, according to the literature, no modeling conducted on deformation or stress distribution of a large part with dimensions in the order of centimetres, while at the same time being able to resolve the movement of the laser beam. Not even for thermomechanical models, let alone multi-physics modeling. Multi-physics modeling is therefore useful for research on melt-pool physics (meso scale) but not yet for bigger structures (macro scale) [56].

2.4.2.3 Thermomechanical analysis of FGMs

The use of FEM on FGMs has also been a point of interest in the literature. For this purpose, one type of software has been specifically designed, namely MicroFEA 1.0 which runs on Abaqus with paths from MATLAB. In Figure 13, its process flowchart is shown, starting from the discrete volume fractions in the pre-processor running in MATLAB and ending with the equilibrium of forces in the Finite Element Analysis (FEA) in Abaqus. MicroFEA 1.0 can use B-splines to fit the volume fractions. It is not always realistic to assume a simple linear or exponential trend in volume fraction, i.e., the transition from one material(phase) to the next. B-splines are better at fitting experimental or computational data than exponential and power-law functions. An example is shown in Figure 14 with experimental data from Watanabe et al. [57].

It can be seen that the B-Spline curve is capable of better accounting for the jaggedness of the actual volume fraction distribution, in comparison to an exponential fit, and is therefore more accurate. The fitted volume fractions and the phase properties are then put through homogenization subroutines to compute the effective material properties. From this, a constitutive matrix can be set up. In the last part of the pre-processor B-splines are evaluated by least-squares fitting to find the required parameters for Abaqus, such as the knot vector and control points data. The FEM analysis in Abaqus can then start with creating the global stiffness matrix and setting up a 3D model containing the volume fractions. With this model, the material properties can be evaluated. Thereafter, the local constitutive matrix can be used to calculate the stress vector that can be used to plot stresses and displacements.

This software is useful to predict stresses and deformations of FGMs, which is beneficial in the booming experimental studies on new FGMs. It can also be used to conduct new research in different areas, such as topological optimization [58].

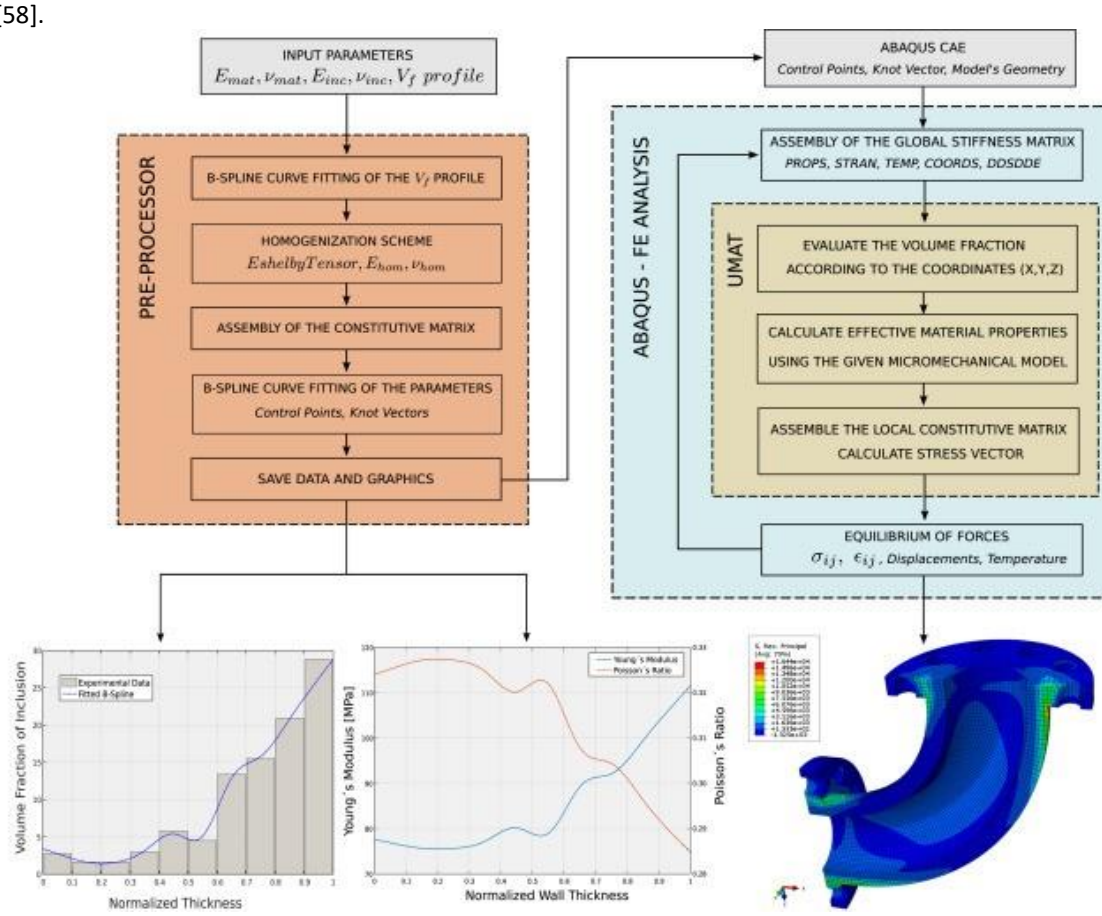

Figure 13. MicroFEA 1.0 operation flowchart, made by Medeiros and Parente [58].

Other software packages exist, such as a coupling of Abaqus and FORTRAN. But instead of the B-splines, these software packages only use a simple power-law distribution [59], [60]. Apart from Abaqus, ANSYS also provides a popular FEM environment, which has been used in a multitude of studies. One study, conducted by Murin et al. in particular, was interesting. It considered a simple FGM beam and compared the results from theoretically derived fourth-order differential equations and beam theory to a simulation with a very fine 2D mesh in Ansys. They found that the achieved accuracy was very high [61]. Another study by Aksoylar et al. on fibre–metal laminated composites furthermore found that there is a good and reliable agreement between the numerical results in ANSYS and their experimental results [62]. Modal analysis can also be conducted using FEM software, as was done by Tabatabaei and Fattahi [59]. They used Abaqus in combination with a subprogram in FORTRAN to find natural frequencies and mode shapes. In comparison to the research conducted by other researchers, they found excellent concordance.

For over a decade, FEM software capable of handling FGMs has been available, but it is still being developed and experimentation is needed to find more experimental data, which is needed to calibrate models and make FGM packages more complete. Furthermore, the computational times on models with FGMs are long (in the order of days) and it is therefore desirable to make models more efficient. On the other hand, one has to be careful not to oversimplify. For example, the models that leave out convective heat transfer, a logical simplification, significantly overestimate temperatures [56]. Overall, FEM has proven to be a valuable tool for the static analysis of internal stresses, as well as modal analysis for FGMs and is therefore a valuable addition in the design of structures, as it can be used to predict deformations and natural frequencies.

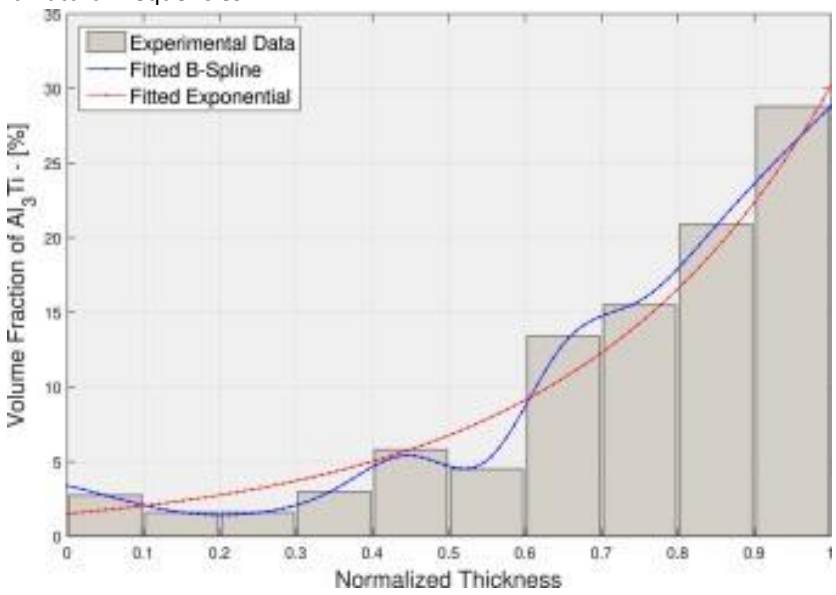

Figure 14. Volume fraction profile, with experimental data from Watanabe et al. [57], used by Medeiros and Parente to show the effectiveness of different fitting methods [58].

3 Methods and Design of Experiment

In this section, the intentions and the method of testing of the experiments and modeling are explained. The schematics of the (powder) systems can be used to understand the setup of each experiment. The section will start with a small introduction of the equipment used for the mass flow calibration and AM. Thereafter, the methods for the experiments will be discussed. The final subsection will concern the used software and methods of modeling.
Concerning the build method, a few aspects are important. First of all, it has been decided based on previous research at the NLR, that a gradual FGM or bimetal is most interesting. The alternate switching method is dropped. Another important aspect concerns the dimensions. This will be discussed in the next subsection.

3.1 Materials and equipment

The Dutch Aerospace institute acquired the BEAM Module 400 early 2020, as it features the possibility to make multi-material structures by connecting and activating multiple hoppers at the same time. The DED module is shown in Figure 15. Note the 4 hoppers in the cabin, which are also shown in Figure 16a. Its oscillating mechanism, as illustrated in Figure 16b, is shown in Figure 16c. The hopper can be adjusted over a range of oscillating percentages from 0% to 100% in whole integers, where a higher percentage results in a higher mass flow. The mass flow during operation can be seen in Figure 16d.

Figure 15. BeAM Modulo 400 as part of the research facility of NLR. Note the four powder hoppers at the right side of the machine.

It took a few months to prepare the machine for AM. Once the machine was ready, multiple studies were conducted on printing with Ti-6Al-4V, In718 and SS316L powders. The first studies were on parameter optimization for the individual materials. Recently, two studies have been conducted on deformations and internal stresses [71] and on making an FGM combining SS316L and In718, as shown in paragraph 2.3.1 [16]. In order to get a combined mass flow, a simple y-connection, see Figure 17, proved sufficient in mixing. The addition of a static mixer (a tube with some static

obstacles inside), did only slow down the mass flow, which made it harder for the particles to break the surface tension and therefore lead to an increase in porosity. The research presented in this thesis expands on these two studies, as we aim to improve the build quality of the FGM and analyze the deformations of the same FGM structures by performing simulations and experiments.

(a)

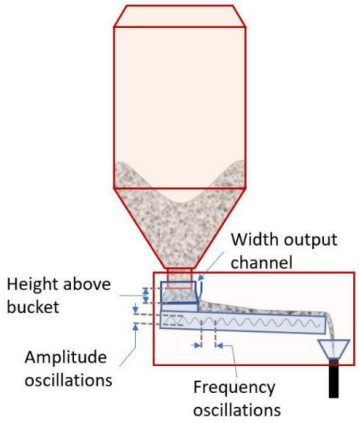

(b)

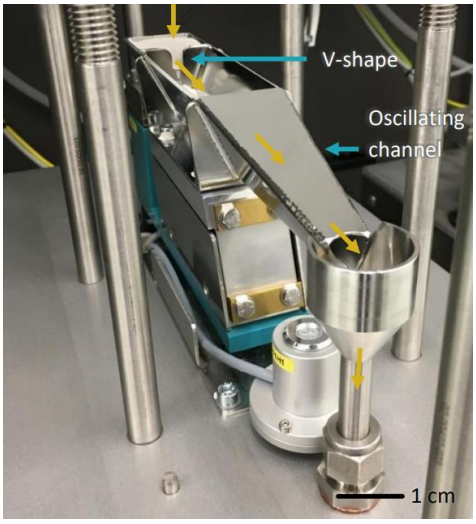

(c)

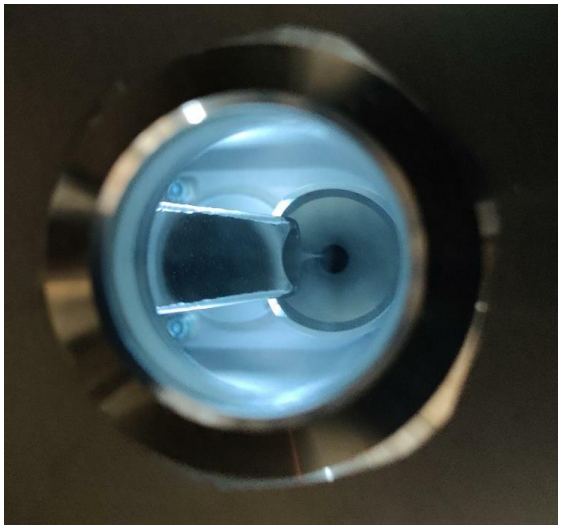

(d)

Figure 16. (a) The four powder hoppers of the BeAM Modulo 400 machine as part of the research facility of NLR. (b) Schematic of the inner mechanics of the hopper [40], [41]. The blue arrows indicate the elements that determine the outcoming mass flow. (c) Zoom-in on the inside of one of the hoppers showing the oscillating mechanism. (d) Powder flowing out of the activated hopper.

Figure 17. (a) Image of the Y-connection used to connect two hoppers in order to combine the mass flows. (b) Installed Y connection.

Another important aspect in BeAM M400 is the gas flows through the nozzle, see Figure 18. Three gas flows can be distinguished. The first is the central gas alongside the laser to protect the lens. The secondary gas flow is important to shape the mid-air mass flow. It basically pushes the powder straight down to create a less cone-shaped gas flow and more vertical. Still the gas flow and therefore powder diameter is quite cone-shaped and without this gas flow the powder diameter would change too much, as the nozzle height to structure changes during manufacturing, which is quite a common phenomenon. And the tertiary gas flow carries the powder through the hoses and nozzle, in Figure 18 indicated with the blue stream [72].

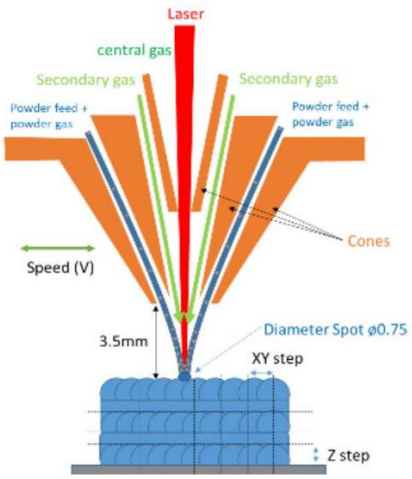

Figure 18. Illustration of the gas flows, as flowing through the nozzle in the BeAM M400 [16], [73].

The used nozzle is the 10VX Nozzle BeAM. The specifications can be found in Table 1.

Table 1. Characteristics 10VX Nozzle BeAM

	Distance to substrate [mm]	**Nozzle Diameter [mm]**	**Laser spot size [mm]**	**Accuracy [mm]**	**Power range laser source [W]**	**Deposition volume [cm³/h]**
10VX Nozzle	3.5	0.8	0.75	± 0.1	100-1000	5.5-6.5

3.1.1 Material selection

The Dutch Aerospace Institute has experience with the AM of 3 metals, namely SS316L, In718 and Ti-6Al-4V. It would therefore be favourable to use a combination of two of these materials, as the process parameters have been optimized already.

Not all metals are directly compatible. The main challenges are intermetallics or very dissimilar thermal properties such as melting temperature and CTE.
If this is the case, it might still be possible to make a bimetallic structure instead of an intermediate-transitioned FGM. This can be done via a compositional bond layer (CBL) to counteract the formation of brittle intermetallics and create a good bonding. An example of such a filler material, also called a buffer layer or a filler material, is the use of vanadium-carbide (VC) for the two immiscible alloys, i.e., Inconel and Ti-6Al-4V [63]. This way, a bimetallic structure can be created without the formation of the intermetallics, $TiNi_3$ and Ti_2Ni, to prevent microcracking. In Figure 19, a summary is given to show which combinations of the available materials at the NLR, namely SS316L In718 and Ti-6Al-4V are directly compatible and which combinations are less compatible with their possible corresponding filler materials.

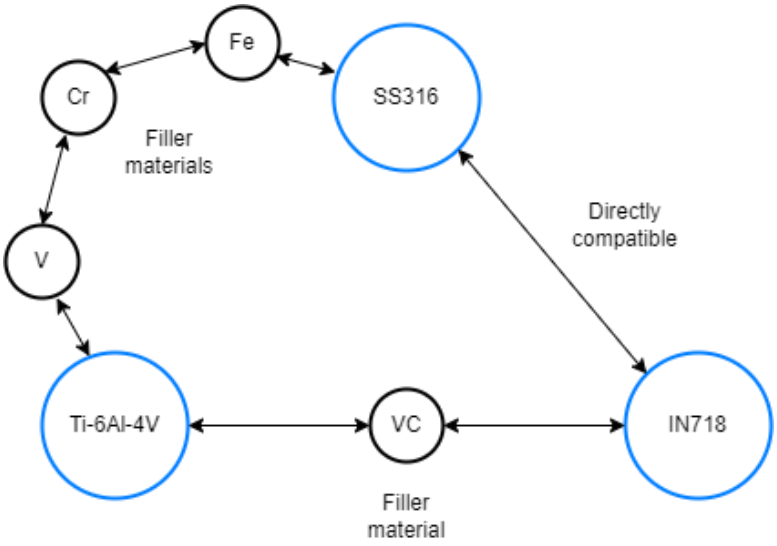

Figure 19. Visual representation of defect-free compatibility between three of the most popular AM FGM materials SS316L, Ti-6Al-4V and IN718, also available at the Royal NLR. Illustrating the use of Vanadium carbide as a filler material between Ti-6Al-4V and IN718 [63] and the V-C-Fe transitional compositional route for the combination of Ti-6Al-4V and SS316 [23]. SS316 and IN718 are directly compatible [35], [37].

In Table 2, the respective physical and mechanical properties of IN718, SS316L and Ti6Al-4V are summarized. Concerning the usefulness of the combinations, it is favourable if the properties are as divergent as possible. One example is a discrepancy in density and strength. Titanium is clearly a strong lightweight material with good thermal properties, although creep has to be taken into account. Inconel, on the other hand, has good creep resistance, compared to the other metals and has a significantly higher ultimate tensile strength (UTS) and yield strength. Furthermore, it can be noted that they are all low magnetic susceptible, so no uses can be found in this area. Another observation is that the CTE values of IN718 and SS316L are more similar, relative to Ti-6Al-4V. This is important for their compatibility, since this discrepancy causes high internal stresses. Finally, broad ranges of the values of UTS and yield strength for the materials SS316L and Ti-6Al-4V exist. This is due to a discrepancy between sources, most likely due to differently applied heat treatments.

Table 2. Material properties of IN718, SS316L and Ti-6Al-4V(Grade 5) [64], [65], [66], [67], [68], [69], [70].

	IN718	SS316L	Ti-6Al-4V (Grade 5)
σ-ultimate (MPa)	1375	485-560	897-900
σ-yield (MPa)	1100	170-290	827-830
Melting point, Solidus (°C)	1260	1375	1604
Melting point, Liquidus (°C)	1336	1400	1660
Thermal expansion coefficient (μm/m°C)	13	15.9-16.5	8.6
E-modulus (GPa)	200	193	114
Density (g/cc)	8.19	8	4.43
Magnetic permeability (H/m)	1.0011	1.008	1.00005

To conclude, from the available materials at the Royal NLR: titanium, stainless steel and Inconel, the combination of SS316L and In718 was the only viable option for intermediate sectioned FGMs or bimetals without a Compositional Bond Layer (CBL). Therefore in order to get good quality FGMs, which can be used to analyse deformations of different types of FGMs, the logical conclusion was to continue the research on this combination. Finally, the Dutch Aerospace Institute wished to improve the quality of these types of FGMs, as it finds relevance in a project for an FGM oil-valve for Mokveld and Shell. Therefore, new findings from literature on improving the quality have been incorporated into this thesis as well. Specifically, two improvements were incorporated, first of which is leaving out the 25wt% range to avoid microcracks mostly due to intermetallics. Secondly, a smaller hatch spacing was introduced to reduce porosity, more specifically unmolten particles, due to an insufficient energy per area input.
For more information on many other materials and combinations, the reader is referred to the literature review prior to this thesis project.

The specific powders that were used are IN718 from AP&C with a size distribution from 45 to 90 µm and SS316L from Oerlikon with a size distribution from 45 to 106 µm. The powder compositions of the two materials are shown in Table 3.

Table 3. Compositions [wt%] of Inconel 718 and Stainless Steel 316L powders.

	C	Mn	P	S	Si	Cr	Mo	Ni	Cu	Al	B	Co	Nb, Ta	Ti	Fe
In718	0.04	0.01	0.004	<0.001	0.04	18.9	3.09	52.06	<0.1	0.56	0.002	<0.1	5.04	0.92	Balance
SS316L	0.02	1.34	<0.01	<0.01	0.46	17.08	2.32	12.29	0.05	-	-	-	-	-	Balance

3.2 Design of experiment

This section will discuss the design of the experiment, starting with the chosen dimensions and material ratios for the structures to be produced. Thereafter, the specific procedures for mass flow calibrations and the actual AM experiment will be discussed. Finally, the methods of geometry analysis and microstructural analysis will be described.

3.2.1 Dimensions and material ratios

In recent research conducted by Ir. Vroon, the dimensions of 160 mm in length 4.8 mm in width and 4.8 mm in height were chosen [71][1]. To stay consistent and make possible comparisons between our conducted research, the same dimensions were used for all 7 modelled structures in this thesis. The exact dimensions are shown in Table 4-5. Note the absolute height which displays the actual height at the top of each section with a total of height of 4.8 mm at the last section.

Three types of FGMs were to be produced. The first was an FGM with 10% incremental sections but without the 20 wt% and 30 wt% In718 sections, hereafter referred to as type 10 wt% FGM. The second had 20 wt% sections but without the 20 wt% section (type 20 wt% FGM). And the third was a bimetal. Apart from these, a pure In718 structure and a pure SS316L structure were to be produced (Table 6). For an overview, please see the illustration in Figure 20.

Table 4. Dimensions of type 10wt% FGMs.

Section #	Number of layers	Length (mm)	Width (mm)	Absolute height top (mm)	Inconel wt%
1	1	160	4.8	0.2	0
2	3	160	4.8	0.8	10
3	3	160	4.8	1.4	40
4	3	160	4.8	2	50
5	3	160	4.8	2.6	60
6	3	160	4.8	3.2	70
7	3	160	4.8	3.8	80
8	3	160	4.8	4.4	90
9	2	160	4.8	4.8	100

Table 5. Dimensions type 20wt% FGM.

Section #	Number of layers	Length (mm)	Width (mm)	Absolute height top (mm)	Inconel wt%
1	4	160	4.8	0.8	0
2	5	160	4.8	1.8	40
3	5	160	4.8	2.8	60
4	5	160	4.8	3.8	80
5	5	160	4.8	4.8	100

Table 6. Dimensions 100wt% pure metal alloys and bimetal.

Section #	Number of layers	Length (mm)	Width (mm)	Absolute height top (mm)	Inconel wt%
1	12	160	4.8	2.4	0
2	12	160	4.8	4.8	100

To get to the specific dimensions, a few sections in the FGMs 1-3 did have fewer layers. For the 10% FGMs this meant one layer less in the top section and two layers less in the lowest section, as shown in Figure 20b. It was decided to decrease the first layers since these are presumed to have a lower impact on the deformations, relatively to the outer layers which can exert a larger moment (larger distance/arm to the centre of rotation). Furthermore, the middle sections were the point of interest, also from a material standpoint, and were therefore not to be limited in layers. The removal of an extra layer in the proximity of the 25 wt% Inconel range has been considered, but leaving out the 20 wt% and 30 wt% ranges was considered sufficient.

[1] To be published

The compositional route of 10% per increment had been chosen, as this is a setting quite often found in the literature on FGMs. Furthermore, it fitted well with the improvement to leave out the 25 wt% range, as the 20 wt% and 30 wt% sections could be skipped. Another FGM of interest was a bimetallic structure and its subsequent internal stresses. Therefore, two of these structures have been added to the experiment. Furthermore, the 20 wt% sectioned FGM was an intermediate experiment between the 10 wt% sectioned FGMs and the bimetallic structures. Finally, a pure SS316L structure and a pure In718 structure have been added as references. These were expected to show the highest discrepancy in deformation. Table 7-9 shows the exact settings used to get to the desired mass flow (MF) and with that the desired mass fractions for the individual sections.

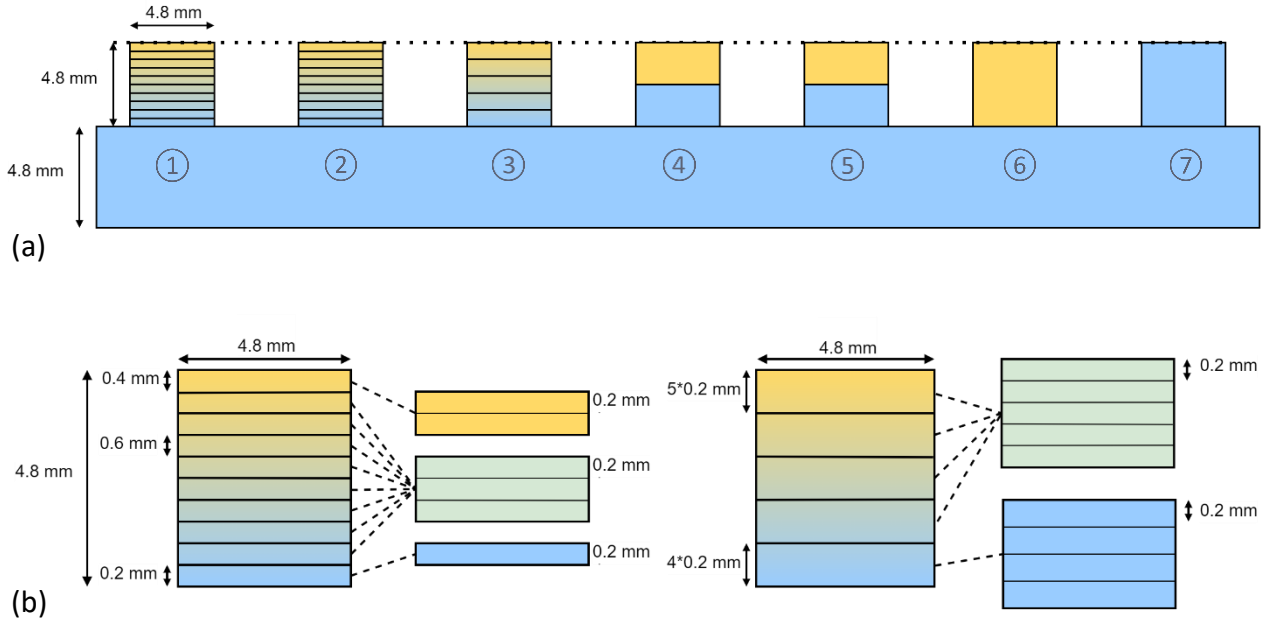

Figure 20. (a) General outline of the experimental set-up. With each structure numbered 1-7. In718 is marked in yellow and SS316L is marked in blue. (b) Zoom-in of the 10% incremental section FGMs and of the 20% incremental section FGM. The lines flowing from the sections show the build-up of the subsequent segments in terms of the number of layers.

Table 7. Compositional route powder feed of build job SS316 & In718 of type 10 wt% FGM.

SS316			**Inc718**				**Output**		**Aim**	
Feeder [%]	MF exp. [g/min]	Aimed MF [g/min]	Feeder [%]	Pre-set [%], used 10s	MF exp. [g/min]	Aimed MF [g/min]	Total MF Exp. [g/min]	Mass fraction Inc718	g/min	Exact Mass Fraction In718
42	6.6	6.5	-	-	-	0	6.6	0.00%	6.5	0.00%
39	5.6	5.85	2	3	0.4	0.55	6	6.67%	6.4	10.00%
33	4	3.9	4	5	2.2	2.2	6.2	35.48%	6.1	40.00%
30	3.2	3.25	5	6	3	2.75	6.2	48.39%	6	50.00%
26	2.4	2.6	6	7	3.8	3.3	6.2	61.29%	5.9	60.00%
22	1.7	1.95	6	7	3.8	3.85	5.5	69.09%	5.8	70.00%
20	1.275	1.3	7	8	4.8	4.4	6.075	79.01%	5.7	80.00%
17	0.6375	0.65	8	10	5.3	4.95	5.94	89.26%	5.6	90.00%
-	-	0	9	11	5.7	5.5	5.7	100.00%	5.5	100.00%

Table 8. Compositional route powder feed for type 20 wt% FGM.

SS316			**Inc718**				**Output**		**Aim**	
Feeder [%]	MF exp. [g/min]	Aimed MF [g/min]	Feeder[%]	Pre-set [%], used 10s	MF exp. [g/min]	Aimed MF [g/min]	Total MF Exp. [g/min]	Mass fraction Inc718	g/min	Exact Mass fraction In718
42	6.6	6.5	-	-	-	0	6.6	0.00%	6.5	0.00%
33	4	3.9	4	5	2.2	2.2	6.2	35.48%	6.1	40.00%
26	2.4	2.6	6	7	3.8	3.3	6.2	61.29%	5.9	60.00%
20	1.275	1.3	7	8	4.8	4.4	6.075	79.01%	5.7	80.00%
-	-	0	9	11	5.7	5.5	5.7	100.00%	5.5	100.00%

Table 9. Compositional route powder feed for the bimetals and pure alloy builds

SS316			**Inc718**				**Output**		**Aim**	
Feeder [%]	MF exp. [g/min]	Aimed MF [g/min]	Feeder[%]	Pre-set [%], used 10s	MF exp. [g/min]	Aimed MF [g/min]	Total MF Exp. [g/min]	Mass fraction Inc718	g/min	Exact Mass fraction In718
42	6.6	6.5	-	-	-	0	6.6	0.00%	6.5	0.00%
-	-	0	9	11	5.7	5.5	5.7	100.00%	5.5	100.00%

Method of mass-flow calibrations

To create the varying compositional sections, first of all the mass flow needed to be controlled in order to get the right ratio of SS316L to In718 as well as the correct combined mass flow. These calibrations have been performed in previous research on a SS316L-In718 FGM at the Royal NLR. However, calibration was required again as the powder was a year older and therefore slightly more oxidized. Furthermore, the powder characteristics might have been changed due to contamination of the two powders with each other by earlier mass flow calibration through the same hoses [74].
The process parameters were quite similar for SS316L and In718, although they did slightly differ; for example, the powder flow of SS316L was considered optimal at 6.5 g/min whereas earlier experiments with the In718 powder showed that 5.5 g/min was optimal. For the intermediate sections, this value has been interpolated. Still the prime objective was to get the correct ratio of Inconel to stainless steel and the combined mass flow was of secondary importance.

Three calibration series have been performed; the first calibration series on the individual SS316L and In718 mass flows got 1 minute per hopper setting. Thereafter, a series was run with 2 minutes per setting. And finally, the y-connection was inserted and a small series was run to find the combined mass flow. This setup can be found in Figure 21.

Before the calibration, the scale needed to be fully level and tared. The calibration started by flushing the hoses with argon gas so no oxygen could get into the material storage. During flushing, the force exerted by the flowing gas on the scale had been noted. Thereafter, a 2 minute start of the mass flow was initiated, as the mass flow took most time to stabilize from start. Furthermore, to speed up the stabilization process, a pre-step was incorporated to create an extra overshoot; the overshoots can be noted in the result and have the added benefit of giving a clear benchmark of a change

in oscillating setting. Thereafter, three calibration series have been performed, as described in the previous paragraph. Finally the raw data has been extracted to excel and processed.

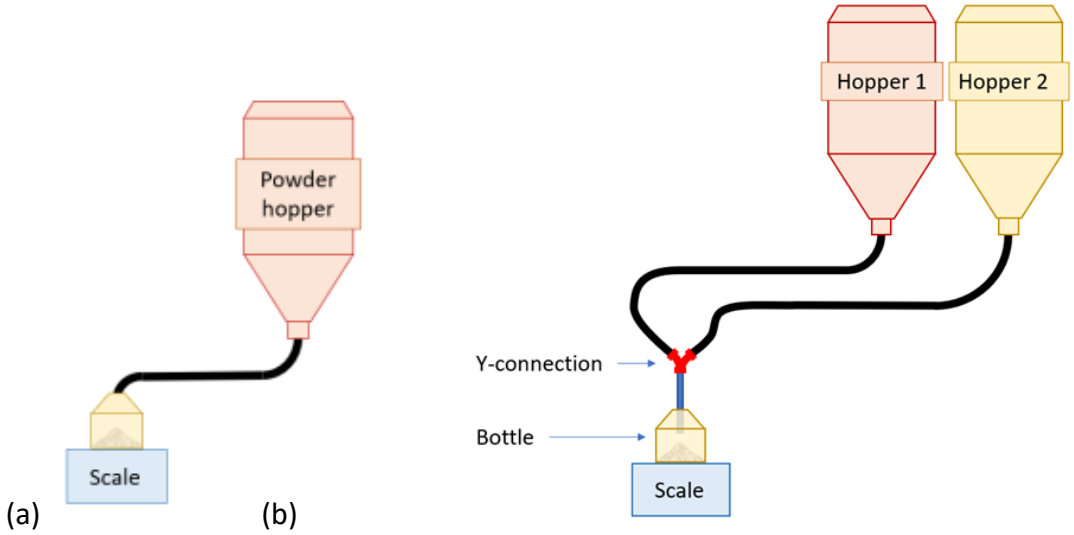

Figure 21. Schematic of the mass flow calibration set-up for (a) the individual mass-flows. (b) Schematic of the calibration setup for the combined mass flow. The red part is the Y-connector. [16]

3.2.2 Method of Additive Manufacturing of FGM structures

With the calibrated hopper settings described in the previous section, seven structures were built on a baseplate, over two days. On the first day, the pure Inconel and pure stainless steel structures have been produced. This was performed with the calibrated settings from mass flow calibration 1. Since the settings needed to be calibrated on the same day of manufacturing, the second and third mass flow calibrations were performed on the second day in advance of the production of the last five FGM and bimetal structures.

Before the production of the structures, the baseplate had been sandblasted to reduce reflectivity and remove oxidation and other impurities. Furthermore, the initial deformation, thickness and weight of the baseplate were measured.
The structures were produced with zig-zag pathing under normal atmospheric conditions but protected by flushing with argon gas. An illustration of the experimental setup, with the fixated baseplate, can be found in Figure 22a and the loose baseplate can be seen in Figure 22b, including what are defined as arms. The dimensions of the baseplate were (L x W x H): 320 x 240 x 11 mm. Each arm had a length of 200 mm and functioned as build platform for a type of structure.
The deformation of the arms, has been used to compare to the predicted deformations from the model.

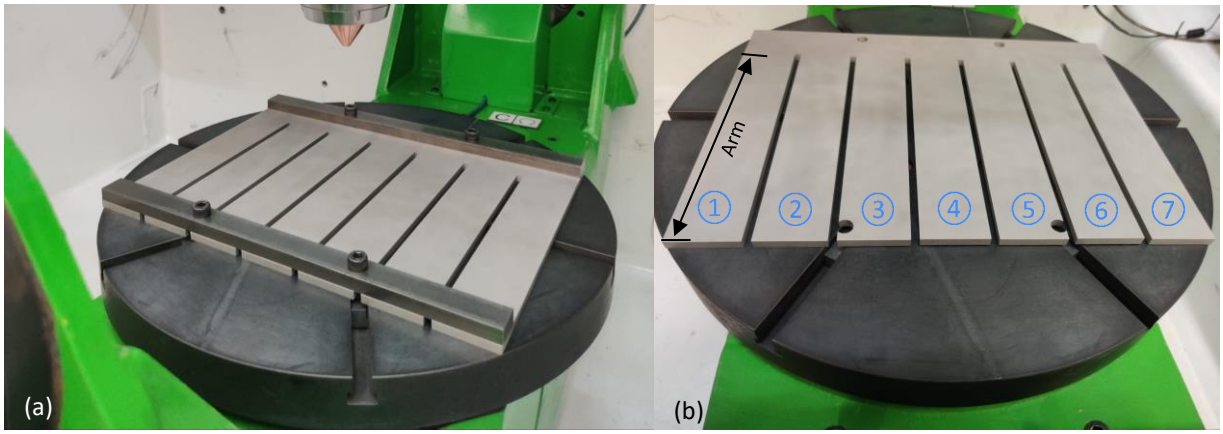

Figure 22. (a) Image of the baseplate, clamped on the black fixation plate, in the DED module. (b) Loose baseplate. The arrow indicates what is defined as an arm, of which seven are present, each functioning as build-platform for a structure.

For the manufacturing parameters the optimized parameters for SS316L have been used for all sections. The exact parameters can be found in Table 10.

Table 10. Deposition parameters

Material	Laser Power [W]	Scanning Speed [mm/min]	Power/speed [J/mm]	Track Width [mm]	Track height [mm]	Central gas flow	Secondary gas flow single hopper [L/min]	Secondary gas flow 2 hoppers [L/min]
SS316L	255	2000	7.65	0.4	0.2	6	3	2 (2x)
In718	255	2000	7.65	0.4	0.2	6	3	2 (2x)

3.2.3 Method of geometry analysis

After the manufacturing, two types of analysis have been conducted. The first concerns geometry measurements to accurately measure the deformations of the built structures. The second is a microstructural analysis which will be described in section Method of microstructural analysis in 3.2.4.

To get accurate measurement of the deformations of the arms, the deformations at the outer edges were measured by hand with a caliper. Before AM as well as after, since there was already a little deformation observed in the baseplate beforehand. The pre-existing deformation was due to the water cutting of the baseplate to create the 7 arms. The water-cutting technique was chosen over laser cutting for its low heat input so that the baseplate did not endure any unwanted extra heat treatment. Furthermore, for higher accuracy, a 3D scan was performed after AM to determine the radii of the deformed arms in the baseplate. Sadly, such an analysis has not been performed before printing, as the small deformations of the arms were only observed just before printing. The radii of deformation before AM have therefore been deducted from the caliper measurements. The deformations after AM were extracted from the 3D scan and fitted to a cylinder in GOM Inspect software to determine the radii of the deformed arms.

3.2.4 Method of microstructural analysis

Concerning the microstructural analysis, midway in the arms, small cross-sectional samples have been taken, as shown in Figure 23. The samples were embedded in epoxy resin, as shown in Figure 24.

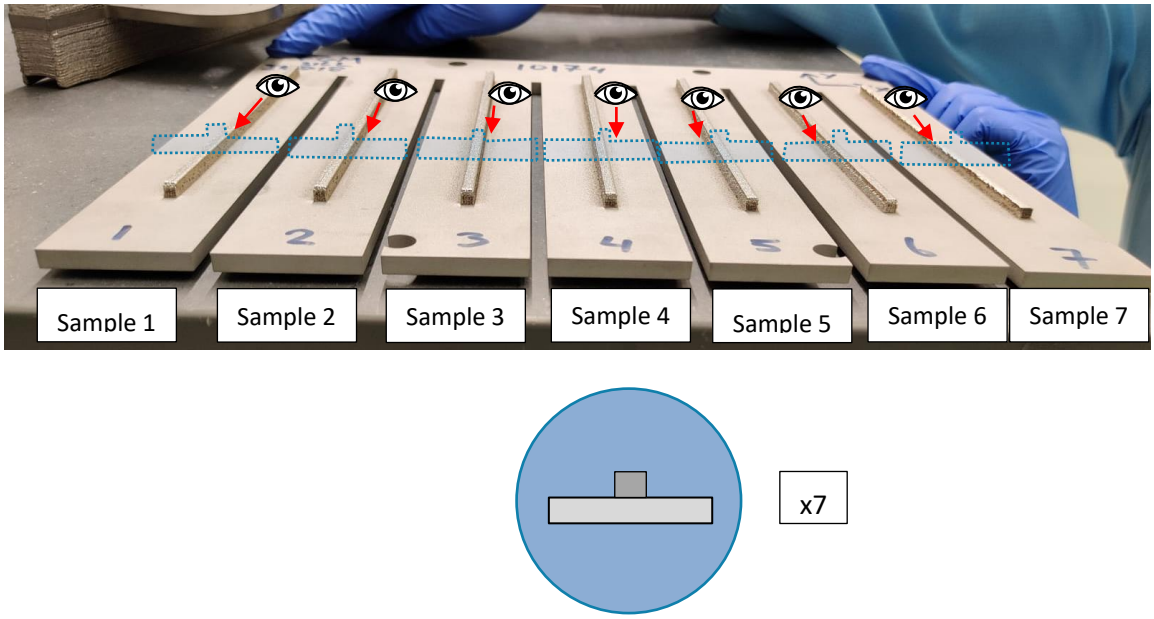

Figure 23. Representation of the area of interest in the produced structures to be prepared for metallographic investigation.

The cross sections have been polished and went through six stages of polishing to get a clear view on the porosity. The porosity was captured in high contrast LOM pictures. Thereafter, etching was performed by submerging the samples multiple times in a reagent until the microstructure was visible. In order to get a clear contrast between SS316L and In718 and to uncover the grain structures as well as melt pool borders, high contrast LOM pictures have been taken.
The first and most effective reagent applied was composed of 40 vol% hydrochloric acid (HCl), 13.8 vol% nitric acid (HNO_3) and 46.2 vol% water. A second reagent has been tried out, composed of HCL (28 vol%), H_2O_2 (1.4 vol%) and water (70.8 vol%). The latter was too reactive and therefore results from the first reagent will be exhibited in the results.

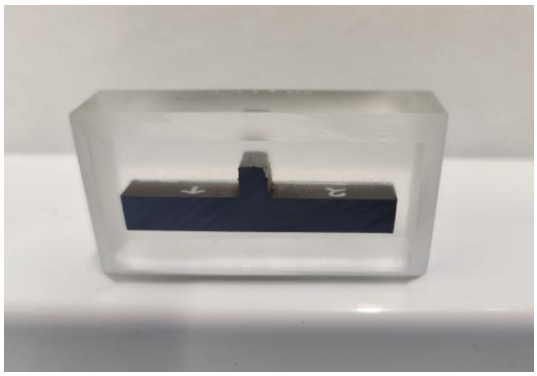

Figure 24. One of the cross-sectional samples embedded in epoxy resin used for microstructural analysis.

3.3 Thermomechanical modeling

The section will discuss the simulations to predict the deformations of each of the structures. The general method will first be discussed. Thereafter, a subsection is dedicated to the retrieval and derivation of (heat-dependant) material properties which are crucial for the fidelity of the simulations.

3.3.1 Method of simulation

A model of the complete experiment (fixation plate and baseplate plus structures) has been built, see Figure 25.

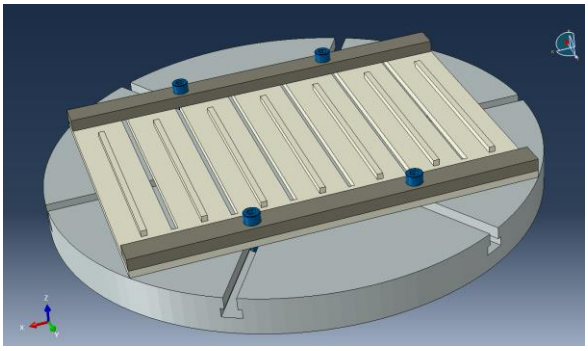

Figure 25. Overview of the complete model including the large fixation plate shown in grey and the baseplate including the to-be-printed structures in khaki.

The to-be-manufactured structures in the model were meshed with 8-node quadrilateral elements, with dimensions of 0.48x0.48x0.2 mm, the same dimensions as the melt pool in the experiment. See Figure 26 for an overview of the mesh. Since the dimensions were the same as the melt pool and the procedure of adding material was similar to the experiment, this should give good fidelity [71]. The element dimensions of the meshes of the baseplate were 3x3x1 mm and those of the fixation plate were 10x10x13.5 mm.

The procedure started with a thermal simulation of the AM of each individual structure.
For this, the path of the printer was planned, similar to the actual AM experiment (in G-code).
As the simulation was started, the elements were activated, in a timeframe, by a cross-sectional area running over the path. Thereafter, a box with the size of one element ran over the path. The box gave heat input to the elements defined as a laser spot, with a top-hat shape, and a defined laser power in watts. This box ran one box length behind the activation, to ensure the elements were activated first [74], [75]. Furthermore, a few simplifications were applied, such as no convection or radiation in the fixation plate, as this plate was relatively large and heat build-up was negligible, see Figure 25. Furthermore, heat was only able to travel from the baseplate to the fixation plate via conduction.

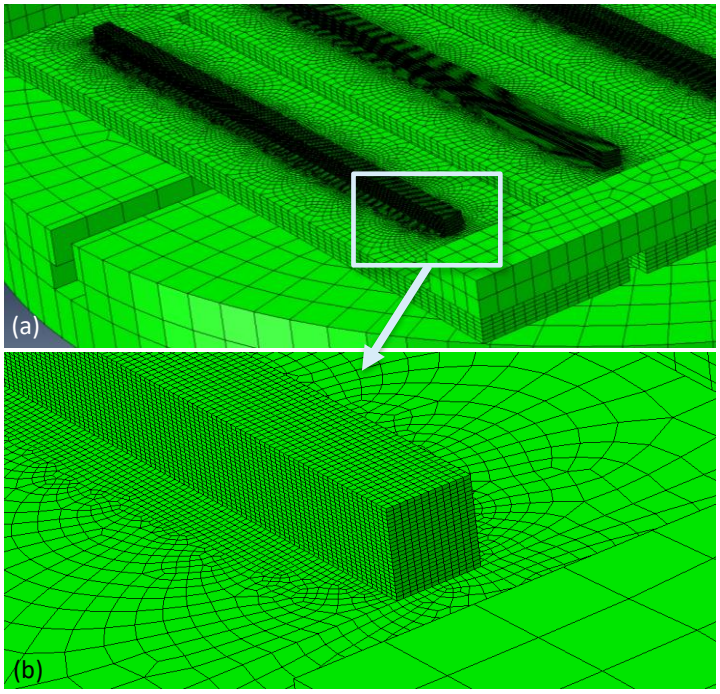

Figure 26. (a) Image of the mesh created in Abaqus CAE. (b) Zoom-in of the mesh of the structure on top of the baseplate. In the left corner a part of the clamp is notable with a very coarse mesh. Note the very fine mesh for the structure which is the area of interest.

To reduce computational effort, each step in the simulation activated multiple elements, around the length of 1.8 track or 10 seconds of pathing, see Figure 27. This was far larger than the melt pool size, which was approximately one element. The energy in this time period was distributed equally over the activated area. This was a significant simplification, but for a part-scale simulation it was unavoidable, as a shorter step size would lead to excessive calculation costs.

In the recent research on modeling with Abaqus for DED and PBF by Koenis [76], this was found to be an acceptable simplification as long as the results are calibrated to an experiment, by adjusting convection coefficient, radiation coefficient and initial temperature. This calibration is still needed to get correct magnitudes but after calibration the relative deformations are consistent.

The mechanical simulation was applied, based on the results of the thermal simulation which provided the temperature profile during the process. The simulation started again with the elements activated by a moving cross-section and a box slightly behind, to give the thermal input. The simulation then computed the expansion and thereafter shrinkage of the structure as the process continued. When all the elements were activated, a final phase was introduced, which incorporated the release of the baseplate from the fixation plate. The baseplate was thereafter able to deform freely, as all physical constraints had been removed. In small steps, the final deformation was obtained in an equilibrium of thermal stress and mechanical stress due to the stiffness of the baseplate. The resulting deformation was thereafter compared to the experimental results. For the mechanical simulation, the material parameters were very important, as well as the material behaviour over a wide range of temperatures. The next section will go into detail on these material properties.

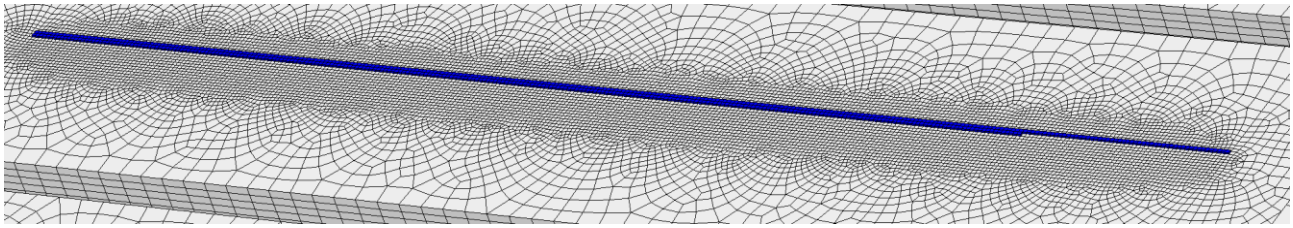

Figure 27. First and single step in a simulation, with a total length of approximately 1.8 tracks.

3.3.2 Material properties

The outcome of the simulation was expected to depend heavily on the provided material properties, such as plasticity, conductivity, Young's modulus, Poisson's ratio, CTE and specific heat. Furthermore, most material properties change with varying temperature. Finally, the intermediate properties have been linearized, as is a common approach in the literature, see section 2.4.1. Finally, some material properties should not affect the simulations and were therefore left out. These considerations will be discussed first.

Creep and ultimate tensile strength

The possible occurrence of creep was the first consideration to determine if this should be added to the analysis. If it were to be added, this would change the type of analysis to being time-dependant and therefore be more computationally intensive.

Based on the data of In718 from E. Hosseinia and V.A. Popovich [77], shown in Figure 28, it can be seen that at a temperature of 650 ^{0}C and at quite a high stress level, creep is only significant, if the stress is applied for over 200 hours. If we compare this to the conditions experienced in the DED process, as modelled, the time endured at high temperatures was in the order seconds and creep has therefore no influence. Inconel is known for its good creep resistance, but SS316L will neither experience creep, if stress is applied for a duration in the order of hours. [78]

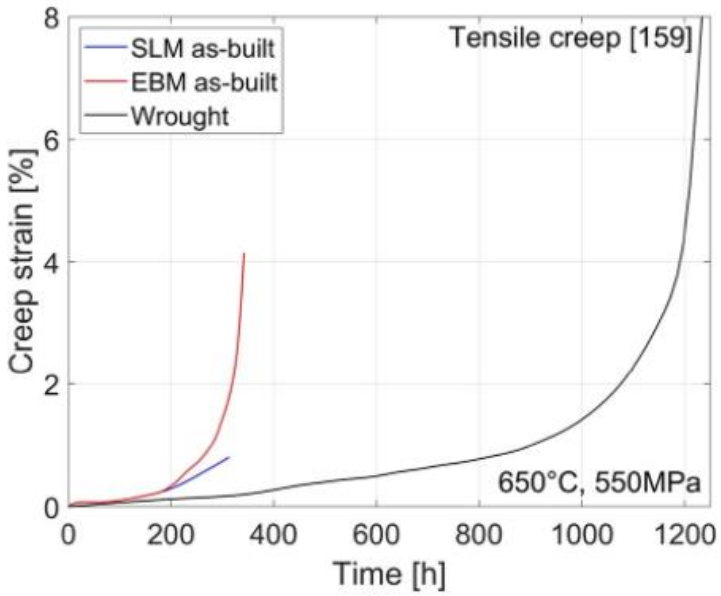

Figure 28. Creep versus time based on the data of In718 from E. Hosseinia and V.A. Popovich [77]

Therefore, the analysis was chosen to be time-independent and rely on the plastic strains at different temperatures as is common practice at the Dutch Aerospace institute.
Furthermore, concerning ultimate tensile stress, this was not considered, as the model did not include failure of the structure. Finally, most of the material properties of SS316L were already available from a previous study on the simulation of just SS316L [71].

Plasticity

Plasticity behaviour is dependent on not only temperature but also strain rate. This gives a large divergence in the literature on In718 [79-85]. For SS316L, some high quality data was available at a strain rate of 0.01/s [86], whereas for In718 most congruent sources used a strain rate of 0.001/s. The slight difference in stress due to this discrepancy in strain rate was found neglectable, especially at lower temperatures. Therefore, the yield stresses of In718 at various true strains have been extracted from the curves shown in Figure 29 [79]. Note the extracted data points indicated with the small red dots. The temperatures at which the stresses were obtained are mostly the same for In718 and SS316L, except at 950 ^{0}C and 1050 ^{0}C. To match these temperatures, the data from In718 has been linearized.

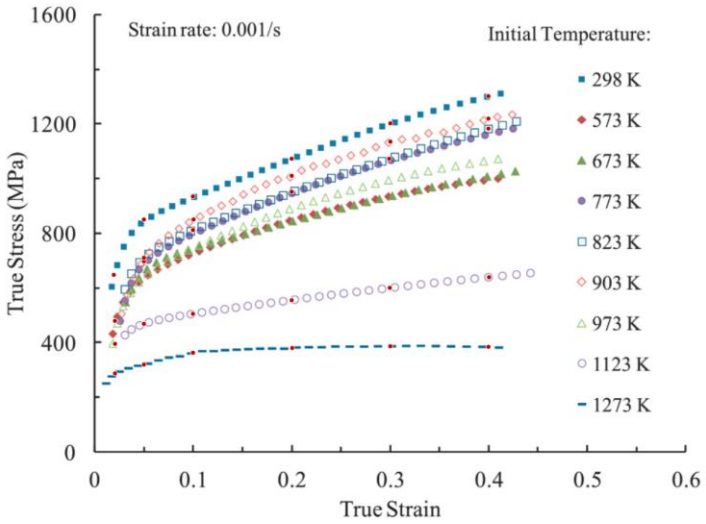

Figure 29. The true stress vs. true strain curves in the Z-direction at different temperatures and at a strain rate of 0.001/s. Including the extracted datapoints indicated with the small red dots. [79]

Conductivity λ

The conductivity values have been obtained from Simufact software [87].

Youngs modulus and Poisson ratio

Temperature-dependant Young's moduli of In718 were retrieved from a study by Aba-Perea et al. [88].
As for the Poisson's ratio, this was not taken to be temperature-dependant and the difference between SS316L and In718 is small, i.e., 0.294 and 0.3, respectively. Nonetheless, it has been interpolated for the individual sections.

Coefficient of Thermal Expansion

The temperature-dependant CTE has been retrieved from the study of Agazhanov, Samoshkin and Yu Kozlovskii [89].

Specific heat

The temperature-dependent specific heat data has been extracted from a comparative study of multiple studies on the Inconel 718 alloy, with line 4 in Figure 30 as the recommended data [89]. The obtained data points from this figure are indicated by the small red dots.

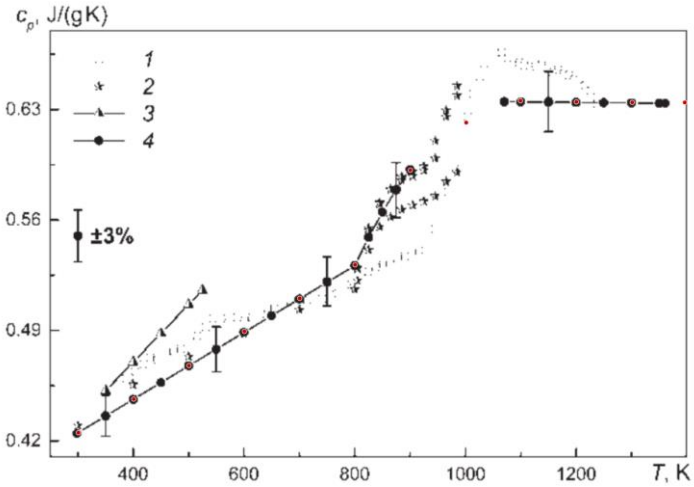

Figure 30. Comparison of the specific heat data of multiple studies on the Inconel 718 alloy with line 4 as recommended data [89]. Including the obtained datapoints indicated by the small red dots.

Density

Density was also added but as a temperature-independent property, since the CTE already accounted for material expansion. The density was set as 7966 Kg/m^3 for SS316L [71] and 8190 Kg/m^3 for In718L [65].

3.3.3 Boundary conditions

The simulation furthermore relied on a few boundary conditions and additional parameters such as the laser absorption coefficient. The parameters and their description can be found in Table 11. For the manufactured parts a different convection coefficient has been applied due to a higher gas flow. Furthermore, a higher radiation coefficient was applied due to a higher surface roughness [71].

Table 11. Simulation parameters.

Parameter	Value	Description
Laser absorption coefficient	0.4	Laser energy absorbed in the melt-pool
Initial temperature	24 °C	Initial temperature of the entire system
Convection coefficient Manufac. Parts	25	Convection coefficient for the manufactured parts as these experience a higher gas flow
Convection coefficient	10	Convection coefficient for the rest of the system
Radiation coefficient Manufac. Parts	0.45	Radiation coefficient for the manufactured parts, being higher due to a higher surface roughness
Radiation coefficient	0.3	Radiation coefficient for the rest of the system

A few (boundary) conditions will now be discussed. First of all, in the cool-down step of the simulation, the convection was decreased from 25 to 10, as there is no longer forced convection of the gas flows. Secondly, in the thermal model,

a tie connection was used between the parts; this stands for a shared temperature of the shared nodes. This was a simplification, as no contact conduction was taken into account, but the impact was considered minimal as the contact conduction was large due to the tight clamping. Furthermore, in the mechanical model, the clamps were replaced by a fixation condition in three directions. This boundary condition was only applied at the ground surface at the location of the clamps. Finally, in the release step, one node was fixated in the x, y and z directions and the rest of the nodes only in the x direction to avoid warping.

4 Results and Discussion

4.1 Mass flow calibration

For the creation of the incremental sections, first of all, the mass flow needed to be controlled in order to get the right ratio of SS316L to In718, as well as the right combined mass flow. The mass flows have been calibrated before, so there was some prior knowledge on calibration. For example, increasing the mass flow led to longer stabilization times, compared to decreasing the mass flow, and a bigger change in oscillating percentage needed a longer stabilization time. Finally, despite the availability of prior calibration data, recalibration was needed because the powder was a year old and might have been contaminated slightly. This contamination of In718 and SS316L with each other, is due to mass flow calibration using the same hoses. Furthermore, the powders might have gotten a little oxidized over time [74]. The process parameters were quite similar for the SS316L and In718 powders. Slight differences, such as the desired combined mass flow, have been taken into account by interpolation.

The new parameters that were to be tested were chosen carefully, based on the data from the previous study, see Table 12. The new parameters, interpolated and extrapolated, can be found in Table 13. Note that the aim was to be as close as possible to the desired mass fraction as well as the desired total mass flow and that these aims are different from the previous study by Lanters. Furthermore, there seemed to have been some inconsistencies in the previous tests at the 7% oscillate capacity of Inconel (oscillate capacity between 0-100%). For this setting the mass flow was relatively high and this might have been an error. Therefore, the same oscillating setting was kept, even though it might seem a bit too high for the 70% section. Calibration will necessary for this fine-tuning .
The first calibrations on the individual SS316L and In718 mass flows, which got 1 minute per hopper setting, appeared to be not yet fully stabilized. Therefore, the second and third calibrations were performed with a 2 minute duration per setting.

Table 12. Calibration data obtained from a previous study on FGMs by J. Lanters (in bold) [16]. These data were used to make initial decisions on which settings to test in the new mass flow calibrations.

	SS316L				**Inc718**			**Output**		**Exact Aim**
Set-ting	[%]	Mass flow [g/min]	Aim [g/min]	[%]	Pre step	Mass Flow [g/min]	Aim [g/min]	[g/min]	Obt. mass fraction	Desired mass fraction
1	42	**6.6**	6.5	-	-	**-**	0	6.6	0.00%	0.00%
2	39	**5.6**	5.68	2%	1%	**0.4**	0.69	6	6.67%	12.50%
3	36	**4.7**	4.87	3%	1%	**1.5**	1.38	6.2	24.19%	25.00%
4	33	**4**	4.06	4%	1%	**2.2**	2.06	6.2	35.48%	37.50%
5	30	**3.2**	3.25	5%	1%	**3**	2.75	6.2	48.39%	50.00%
6	26	**2.4**	2.44	6%	1%	**3.8**	3.44	6.2	61.29%	62.50%
7	22	**1.7**	1.63	7%	1%	**4.8**	4.13	6.5	73.85%	75.00%
8	18	**0.85**	0.81	8%	2%	**5.3**	4.81	6.15	86.18%	87.50%
9	-	**-**	0	9%	2%	**5.7**	5.5	5.7	100.00%	100.00%

Table 13. Settings chosen for the for first calibration based on the calibration data from Table 12 [16]. The interpolated and extrapolated values are marked in blue colour.

	SS316L			Inc718				Expected (prev. and calc.)		Aim	
Setting	[%]	Expected MF [g/min]	Aim [g/min]	[%]	Pre step	Expected MF [g/min]	Aim [g/min]	g/min]	Mass fraction	[g/min]	Desired Mass fraction
1	42	6.6	6.5	-	-	-	0	6.6	0.00%	6.5	0.00%
2	39	5.6	5.85	2	1%	0.4	0.55	6	6.67%	6.4	10.00%
3	33	4	3.9	4	1%	2.2	2.2	6.2	35.48%	6.1	40.00%
4	30	3.2	3.25	5	1%	3	2.75	6.2	48.39%	6	50.00%
5	26	2.4	2.6	6	1%	3.8	3.3	6.2	61.29%	5.9	60.00%
6	22	1.7	1.95	6	1%	3.8	3.85	5.5	69.09%	5.8	70.00%
7	20	1.275	1.3	7	1%	4.8	4.4	6.075	79.01%	5.7	80.00%
8	17	0.6375	0.65	8	2%	5.3	4.95	5.94	89.26%	5.6	90.00%
9	-	-	0	9	2%	5.7	5.5	5.7	100.00%	5.5	100.00%

The results from the first mass flow calibration contained a large random error. This was caused by the scale, which did not gave a stable output, due to the software and/or the gas flows hitting the scale. The gas flows can be categorized by the three gas flows to the melt pool and another gas flow, which circulates in the DED machine to extract the gasses and nano-particles from the air, before it leaves the machine. The error, caused by the force exerted by the circulating gas flow of the machine on the scale, was found to be at max -0.135 g and mostly around -0.005 g. This random error was resolved by averaging the values over 10 seconds, which gave a much smoother output, see Figure 31. Furthermore, note that the second to last stage was not fully linear (indicated with the orange lines). Therefore, in the second and third calibrations, two minutes per hopper setting has been used.

The average mass flows can also be found in Table 14. Note that the mass flows for stainless steel are much higher than expected. This has been interpolated for the next calibration.

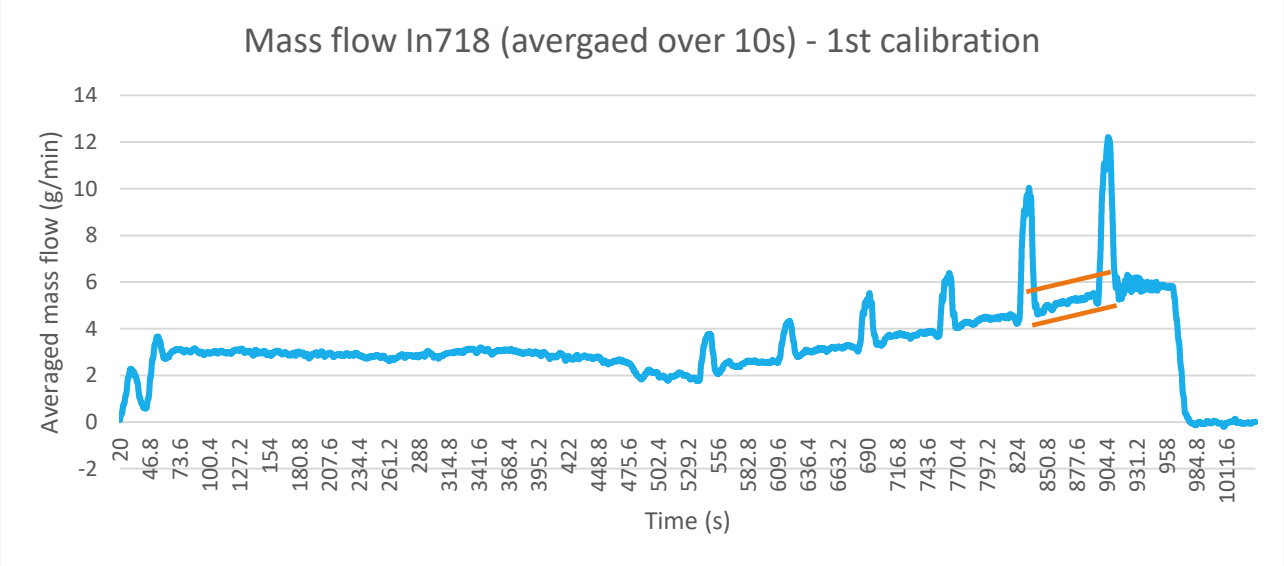

Figure 31. Averaged results over 10 seconds from the first mass flow calibration of In718. Note the not yet stabilized mass flow in the second to last section (oscillating percentage 8%), as highlighted by the red bars.

Table 14. Results from the first mass flow calibration showing the mass flows (in bold) of SS316L and In718 and their respective aims.

	SS316L				**Inc718**		
Setting	[%]	Mass flow [g/min]	Aim [g/min]	[%]	Pre step	Mass flow [g/min]	Aim [g/min]
1	42	**9.09**	6.5	-	-	-	0
2	39	**8.15**	5.85	2	1%	**1.84**	0.55
3	33	**6.08**	3.9	4	1%	**2.60**	2.2
4	30	**5.42**	3.25	5	1%	**3.24**	2.75
5	26	**4.16**	2.6	6	1%	**3.83**	3.3
6	22	**2.95**	1.95	6	1%	**3.83**	3.85
7	20	**2.46**	1.3	7	1%	**4.46**	4.4
8	17	**1.9**	0.65	8	2%	**5.38**	4.95
9	-		0	9	2%	**5.85**	5.5

The first calibrations on the individual SS316L and In718 mass flows, which got 1 minute per hopper setting, appeared to be not yet stabilized, as can be seen in Figure 31 and found in Table 14. Therefore, a second calibration was performed for a longer duration. Each setting was maintained for 2 minutes with a 10 s preset for Inconel. Furthermore, the mass flow values of the SS316L powder were a lot higher than expected and therefore by interpolation new lower hopper settings were chosen. The results can be found in Figure 32 and Table 15.

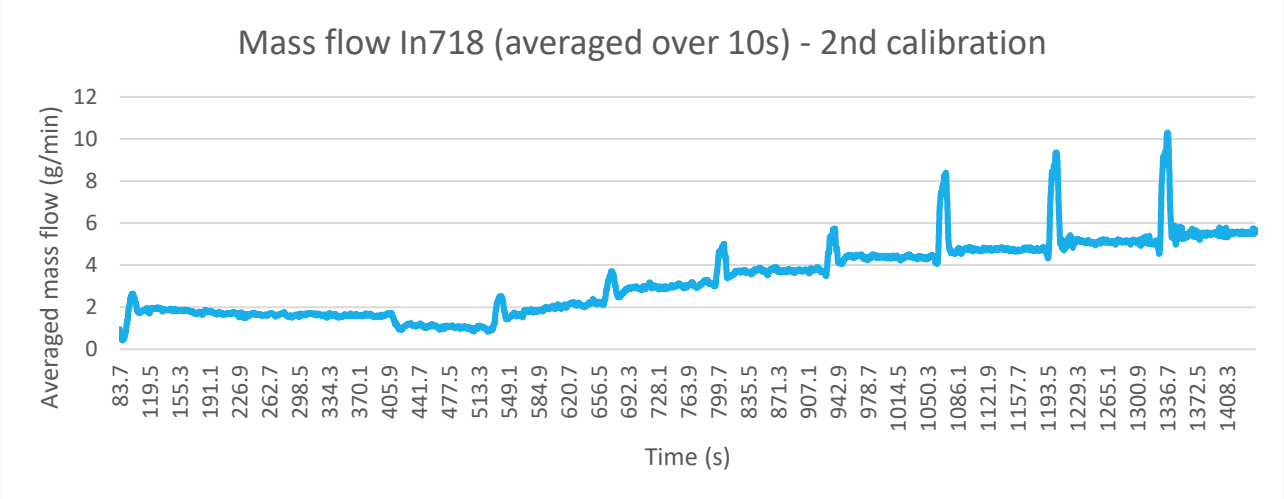

Figure 32. Averaged results over 10 seconds from the second mass flow calibration of In718.

Table 15. Results (in bold) from the second mass flow calibration of SS316L and In718 and their respective aims.

	SS316L				**Inc718**		
Setting	[%]	Output [g/min]	Aim [g/min]	[%]	Pre step	Output [g/min]	Aim [g/min]
1	34	**6.12**	6.5	-	-		0
2	31	**5.19**	5.85	2	1%	**1.05**	0.55
3				3	0%	**1.62**	1.62
4				4	1%	**2.33**	2.2
5				5	1%	**3.27**	2.75
6	26	**2.86**	2.6	6	1%	**3.77**	3.3
7			1.95	6	1%	**3.77**	3.85
8	20	**2.23**	1.3	7	1%	**4.33**	4.4
9	17	**1.41**	0.65	8	2%	**4.77**	4.95
10	14	**1.04**		9	2%	**5.23**	5.23
11	11	**0.48**	0	10	2%	**5.46**	5.5

The results of the second calibration were clearly closer to the aimed mass flow values, although some were still a little bit off. Therefore, the settings for the FGM builds were adjusted by interpolation one more time. The full SS316 and full In718 structures were already build with the settings of 33% and 9%, respectively, so slightly different from the settings found a day later. It must be noted however that the optimal settings can change in a day due to temperature and humidity variations.

Finally a small calibration was performed on the combined mass flows to check the total mass flow. The results can be found in Table 16. Note that the total mass flows were quite a bit off in a non-congruent fashion.
For the combined mass flow of 40% In718, the total mass flow should have been 6.1 g/min, based on the summation of the previous calibrations. It turned out however to be 6.83 g/min. For the combined mass flow of 70 wt% In718, the value was expected to be 5.8 g/min, but in the third calibration it was found to be a lower 4.98 g/min.

A possible explanation for this effect might be that the In718 powder has gotten a little bit more sticky over time, as mentioned before, due to oxidation. This might have slowed the mass flow down, relative to the percentage of In718. The behavior of the combined mass flow is recommended as subject for future research. The produced structures in this thesis project, were larger than expected, approximately, 5.8 mm in width and height compared to the aim of 4.8 mm. This deviation of the dimensions from the simulation is something to take into account as well for comparisons. Since more material was added in the experiment, which comes with internal stress mostly due to the CTE, this can exert a larger force and therefore induce more deformation.

Table 16. Results (in bold) from the third mass flow (MF) calibration considering a combined mass flow of SS316L and In718. The results are highlighted in bold next to their respective aims.

	SS316				**Inc718**			**Output**	**Aim**	
Setti-ng	[%]	MF [g/min]	Aim [g/min]	[%]	Pre step	MF [g/min]	Aim [g/min]	Combined MF [g/min]	Combined MF aim [g/min]	Exact mass fraction
4	28	3.79	3.9	4	1%	2.33	2.2	**6.83**	6.1	40.00%
7	19	1.95	1.95	6	1%	3.77	3.85	**4.98**	5.8	70.00%

4.2 Additive Manufacturing

This section will elaborate on the results obtained from the AM experiments. Subsection 4.2.1 will discuss the deformations from the geometry analysis and section 4.2.2 will elaborate on the microstructural analysis.

With the calibrated input values shown in Table 17, the structures have been manufactured in two days. The desired compositional route per structure and dimensions can be found in 3.2.1 (Dimensions and material ratios).

Table 17. Calibrated oscillating percentages used in the Additive Manufacturing experiment.

	SS316			**Inc718**				**Expected**		**Aim**	
Setti-ng	%	Exp MF [g/min]	Aim [g/min]	%	Pre-step	Exp [g/min]	Aim MF [g/min]	Combi. MF [g/min]	Mass fraction [%]	Combi. MF [g/min]	Exact mass fraction
1	35	6.44	6.5	-	-		0		0.00	6.5	0.00%
2	33	5.81	5.85	2	1%	1.05	0.55		6.67	6.4	10.00%
3	28	3.79	3.9	4	1%	2.33	2.2	6.83	35.48	6.1	40.00%
4	27	3.33	3.25	5	1%	3.27	2.75		48.39	6	50.00%
5	23	2.55	2.6	6	1%	3.77	3.3		61.29	5.9	60.00%
6	19	1.95	1.95	6	1%	3.77	3.85	4.98	69.09	5.8	70.00%
7	16	1.28	1.3	7	1%	4.33	4.4		79.01	5.7	80.00%
8	12	0.67	0.65	8	2%	4.77	4.95		89.26	5.6	90.00%
9	-	-	0	10	2%	5.46	5.5		100.00	5.5	100.00%

During the building of the first 10 wt% FGM structure, the machine stopped due to an mismatch with the G-code. The engineers at Royal NLR have experienced this problem before. The error was caused by the too large accelerations in the path created by the Siemens NX software, which are not feasible for the BEAM Machine. This problem was resolved by creating the code on a different roughness setting, specifically from roughing to smooth-finishing.
After the new code was implemented, the process was restarted at the 80% section and thereafter no problems occurred also not in the production of the second 10 wt% FGM.

By checking the feeder flow in the hopper during the build, it was noted that the Inconel powder had a sticky appearance on the oscillating platform; in other words, the flow showed stick-slip behaviour. This behaviour could have effect on the flow, by making it less stable. The stainless steel powder did not show this behaviour.

Another important factor influencing the mass flow is the cleanness of the tubes. These can get clogged up with residual material after using it a while. This material obstructs the mass flow and therefore slows it down. Residual material can be noted by ticking a little on the nozzle after printing and observing if any amount of powder falls down, this was the case in the experiment.

It was observed that the 7th structure (pure SS316L) was more oxidized on the top side and on the sides due to the longer high-temperature period for that section, as it was harder for the heat to dissipate. The sections with a higher Inconel composition experienced less oxidation.

Another observation was the slightly lower build quality at the left sides of the structures, see Figure 33a, as compared to the right side of the structures, see Figure 33b. This was observed in all the structures except for the pure SS316L build (structure 7).

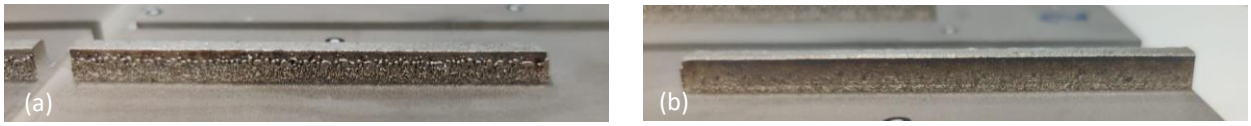

Figure 33. (a) left side of Structure 1, showing higher roughness of the outer layers. (b) Right side of structure. Note the much smoother build quality.

The roughness observed on the left side of every structure, especially in the In718 dominated structures, can be explained by three factors. The first is the build direction, which in this case goes from right to left and therefore the gas flow could have been deflected by the already applied tracks, as illustrated in Figure 34.

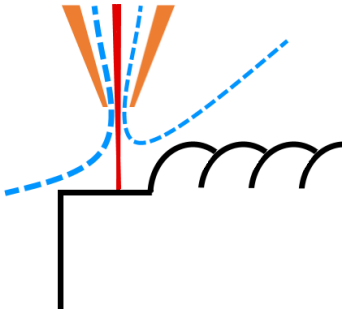

Figure 34. Illustration of the gas flow deflected, to an extent, to the left due to the already applied tracks.

The second possibility is a deviation in nozzle centering (the misalignment of the laser relative to the mass flow). From a small test, the alignment was confirmed to be correct, as can be seen in Figure 35. Therefore, misalignment is excluded as cause.

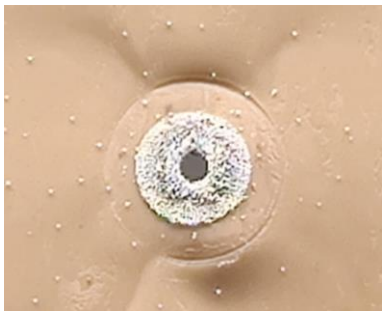

Figure 35. Results of post-experimental laser alignment test. Showing the hole created by the laser in the middle of the circle area of powder particles.

The third possibility, found after manufacturing, was the deformity in the nozzle, as can be seen in Figure 36. This deformity seemed large enough to deflect the gas/mass flow during manufacturing. This deformity is considered to be the main cause of the malformed left side of the structures, according to the mechanical engineer who controlled the BeAM machine during manufacturing.

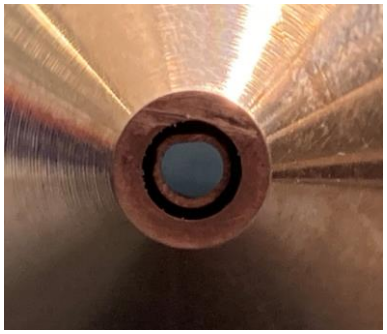

Figure 36. Deformity of the nozzle found after experimentation, most likely caused during assembly of the nozzle in the BeAM assembly.

Finally, the produced structures were larger than expected, 5.8 mm in both height and width, as compared to the aim of 4.8 mm. It might be possible that the absorption of the combination of the two powders in the melt pool was higher. Furthermore, it was already concluded from the mass flow calibrations, that the mass flow characteristics of the combined mass flow deviated a lot from the expected values (from the individual MF calibrations). This behaviour is recommended for future research.

4.2.1 Deformation

This section will provide the results of the deformation before and after AM found with the caliper. Furthermore, a 3D scan, as can be seen in Appendix A.2 Figure 48, has been performed after the manufacturing to determine the radii of deformation in all the arms after AM with slightly more accuracy. These deformations were extracted from the 3D scan and fitted to a cylinder in GOM inspect software, from which the radii were determined. Sadly, such an analysis has not been performed before manufacturing as the small deformations were only observed shortly before the manufacturing process.

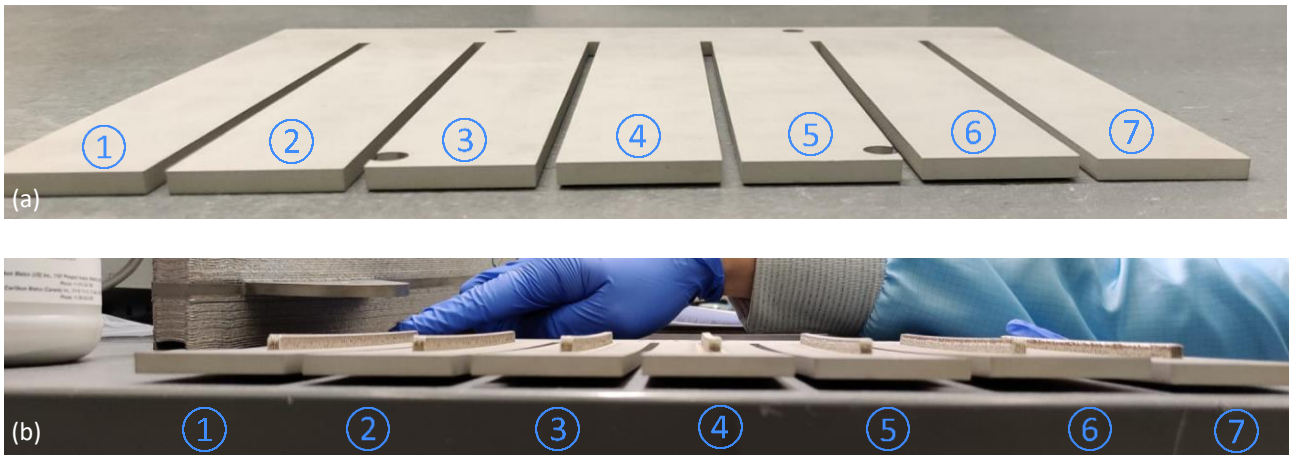

Figure 37. Deformations before (a) and after AM (b). From left to right, 10 wt% section FGMs (1,2) , 20 wt% section FGM (3), Bimetals (5,6), pure In718(6) and pure SS316L (7). Note the higher deformations for the structures with a higher percentage of Inconel.

Therefore, the radii of the deformed arms before manufacturing have been deducted from the caliper measurements. This was possible by considering that the positions of two points were known and the first one, at the start of the arm,

can be taken as horizontal, see Figure 38. This can also be interpreted as two close points on the same height, see Figure 39. With some trigonometry, the radii of deformation and subsequent curvatures were deducted [90]. As the baseplate did not deform after the 160mm millimeter line but linearly increases, it was deducted that taking the endpoint for calculation at 180 gave the most congruent results in the post AM data. This was therefore used to calculate the radius and curvature before AM.

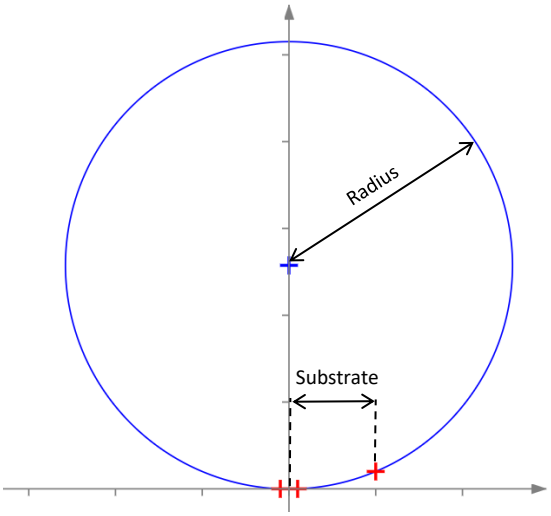

Figure 38. Illustration of the calculation of the radii of the arms. Showing the three points that are at minimum necessary to define a circle.

An overview of all deformations before and after AM can be found in Table 18. The values that have been deducted from the obtained date are highlighted in the blue font.

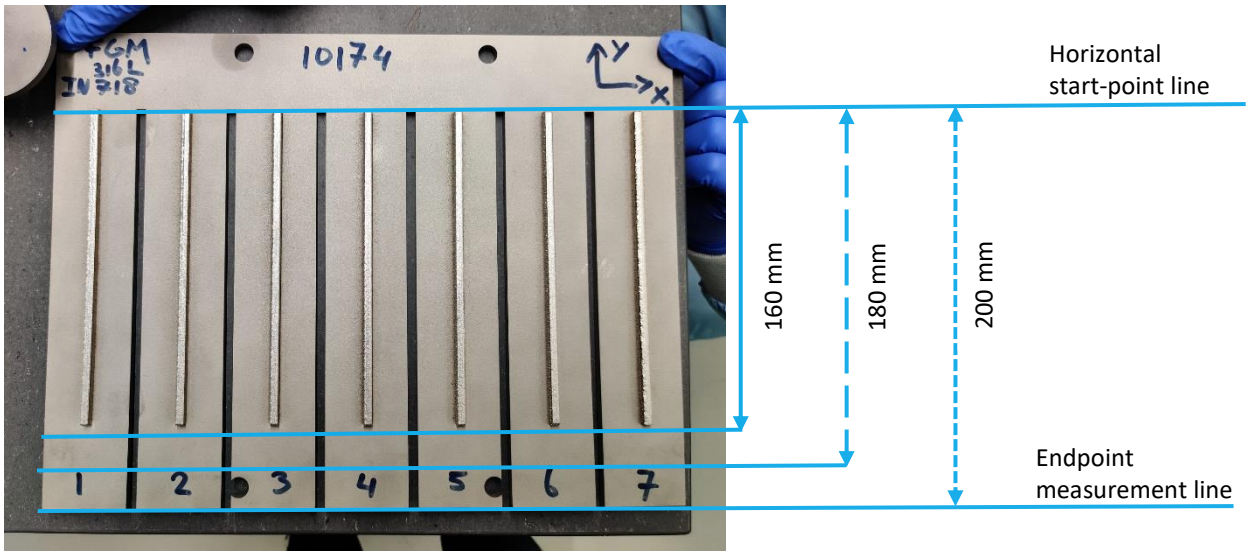

Figure 39. Illustration of the lines, on which the 3 points were taken to calculate the radius of each arm. Two points were taken infinitely close to the horizontal start point line and the third point was taken at the endpoint measurement line. The 180 mm line was used as the x-coordinate in the circle, from which the radii have been deducted.

Table 18. Deformations before and after AM. The values that have been deducted from the obtained data can be found below highlighted in blue.

	Before AM			**After AM**				**Subtracted Results**	
Struc-ture	Endpoint defor-mation [mm]	Deduc-ted Radius [mm]	Deduc-ted Curva-ture [/m]	Endpoint defor-mation [mm]	Radius [mm]	Curva-ture [/m]	Deduc-ted Radius [mm]	Endpoint defor-mation	Curva-ture [/m]
1	0	-	-	3.2	4890.6	0.2045	5064.1	3.2000	0.2045
2	0	-	-	3.2	5010	0.1996	5064.1	3.2000	0.1996
3	0.52	31154	0.0321	3.6	4771.9	0.2096	4501.8	3.0800	0.1775
4	0.88	18409	0.0543	3.8	4608.3	0.2170	4265.1	2.9200	0.1627
5	0.68	23823	0.0420	3.4	4840	0.2066	4766.4	2.7200	0.1646
6	1.08	15000	0.0667	4	4133.2	0.2419	4052.0	2.9200	0.1753
7	0.15	108000	0.0093	2.3	5908.7	0.1692	7044.6	2.1500	0.1600

4.2.2 Microstructural analysis

After the 3D-scan, to measure the deformations, destructive microstructural analysis has been performed. First, the porosity was analysed. The results can be seen in Figure 40.

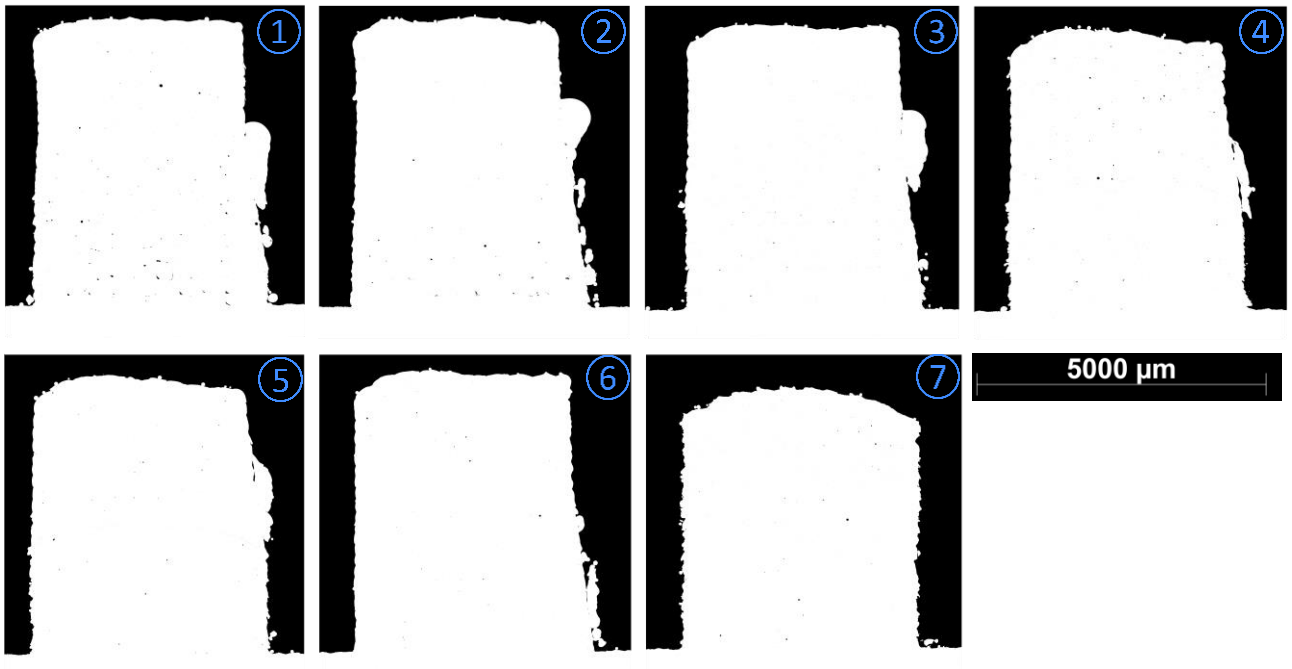

Figure 40. Porosity of all seven structures. From left to right, (1) FGM type 10wt%, (2) FGM type 10wt%, (3) FGM type 20wt%, (4) Bimetal, (5) Bimetal, (6) Pure In718, (7) Pure SS316L.

With a script provided by Royal NLR, the exact porosity percentages have been obtained for the individual compositional sections, as shown in Figure 41. For the type 10 wt% FGMs, this meant that for every 10 wt% section the porosity was determined and for the bimetals only two sections.

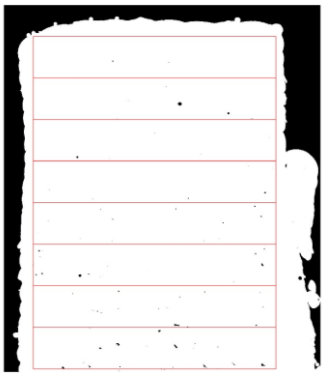

Figure 41. Structure 1, type 10 wt% FGM, the red outlined regions represent the 8 sections in which the porosities have been determined.

The results can be found in Table 19. The total porosity or average porosity is listed in the last column. As is clear from the figure, the obtained porosity percentages of all the structures are relatively low. The percentages of the type 10 wt% FGM are 0.01% and 0.03% and the pure In718 structures even a tenth of that. In comparison, for AM in general, percentages of around 2% or 3% are considered of good quality [91].

Table 19. Porosity values of the sections with distinct composition of the produced structures.

	Section (estimation percentage Inconel [wt%])								**Average**
Structure	1 (0-10wt%)	2 (40wt%)	3 (50wt%)	4 (60wt%)	5 (70wt%)	6 (80wt%)	7 (90wt%)	8 (100wt%)	(0-100%)
1 (type 10% FGM)	0.2964	0.1445	0.1478	0.0514	0.0676	0.0276	0.0352	0.1022	0.098
2 (type 10% FGM)	0.0970	0.1165	0.0046	0.0066	0.0235	0.0000	0.0006	0.0008	0.0312
3 (type 20% FGM)	0.0143	0.0214		0.0105		0.0019		0.0039	0.0104
4 Bimetal	0.0394							0.0565	0.0479
5 Bimetal	0.0195							0.0144	0.0169
6 Pure In718								0.0135	0.0135
7 Pure SS316L	0.0271								0.0271

After the porosity images were obtained, the samples have been etched with a reagent composed of 40 vol% hydrochloric acid (HCl) and 13.8 vol% nitric acid (HNO_3). The results can be found in Figure 42.

First of all, it can be noted that the sides of the structures(regions) dominated by SS316L were lower in height (arc shaped). This can be explained by the lower strength of SS316L by a factor two compared to In718, respectively, 560 and 1375 UTS at room temperature; this continues to be the same at higher temperatures. Moreover, at high temperatures, the SS316L is of a lower viscosity [91], [92], [93]. Furthermore, from simulation, it became apparent that the sides might be at around 10% higher in temperature. Therefore, decreasing the viscosity even further on the sides. Finally for structural reasons, the structure is more supported in the middle by surrounding material, whereas on the sides it can drop off to a side. This effect can be clearly seen in the etched image of In718, Figure 42 (6). However, this

material did experience, despite this effect, a far lower drop-off to the sides, compared to SS316L. Therefore the first two reasons can be considered dominant. The arc shape could be simply corrected by adding more materials to the sides [93].

Furthermore, it can be noted that the SS316L alloy was easier to etch and therefore had a lighter colour, compared to In718. This conveniently also shows the material transition. In Structure 7, it can be noted that the baseplate, which was also composed of SS316L, was lighter, compared to the AM SS316L material. This was due to the different microstructural phases; the exact phases are yet to be determined.

Another observation made in Figure 42, was the presence of rings, most apparent in Structure 1 at the right side of the middle and in the lowest layer of the pure In718 structure, as indicated with the cyan outline in Figure 42. These rings were caused by turbulent flows in the melt pool as layers of different composition were mixed [92].

Between some of the layers, a oxidation layer can be noted in the etched results, especially visible in Structure 6 at the bottom and in Structure 3 between the sections. It is likely that the oxidation layers were formed between the sections, as the manufacturing process was stopped at these positions, for 2 minutes, to stabilize the mass flow of a new composition [94].

Another important observation made, were the unmolten particles present particularly in the FGMs and the In718 part of the first bimetal (structure 4). A comparison between a zoomed-in etched image and a porosity image of Structure 1, type 10 wt% FGM is presented in Figure 43. Note the partially unmolten particles (highlighted in yellow and red outlines) uncovered by etching, which minimally influenced porosity, as they are hardly present in the porosity images. To avoid unmolten particles, a higher energy input would be the simplest solution but a more effective approach would be a

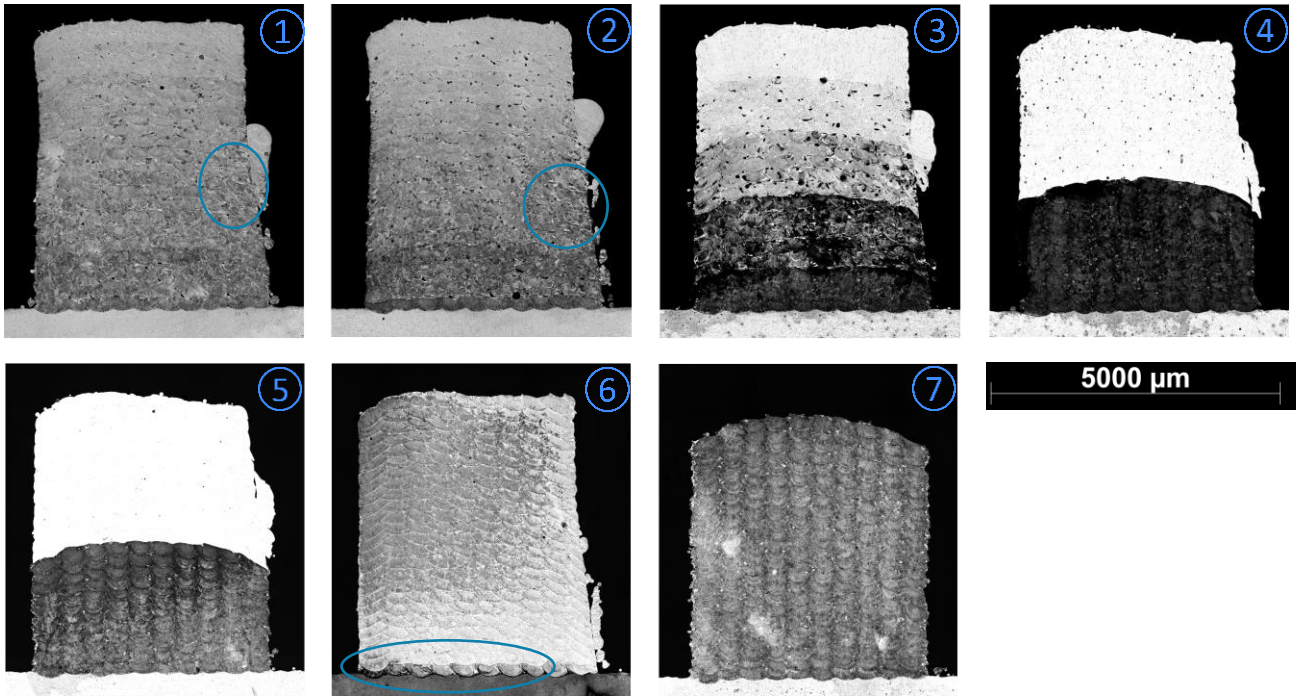

Figure 42. Etched cross-sections of all seven structures. From left to right, (1) FGM type 10wt%, (2) FGM type 10wt%, (3) FGM type 20wt%, (4) Bimetal, (5) Bimetal, (6) Pure In718, (7) Pure SS316L. Note the rings due to melt pool mixing indicated with the cyan outline. Furthermore note the unmolten particles (and a few pores) in Structure 1-3, which can be identified as the black dots.

lower laser speed [93].

Furthermore, the porosities were slightly hollowed out by etching, as highlighted in the blue-marked areas [92].

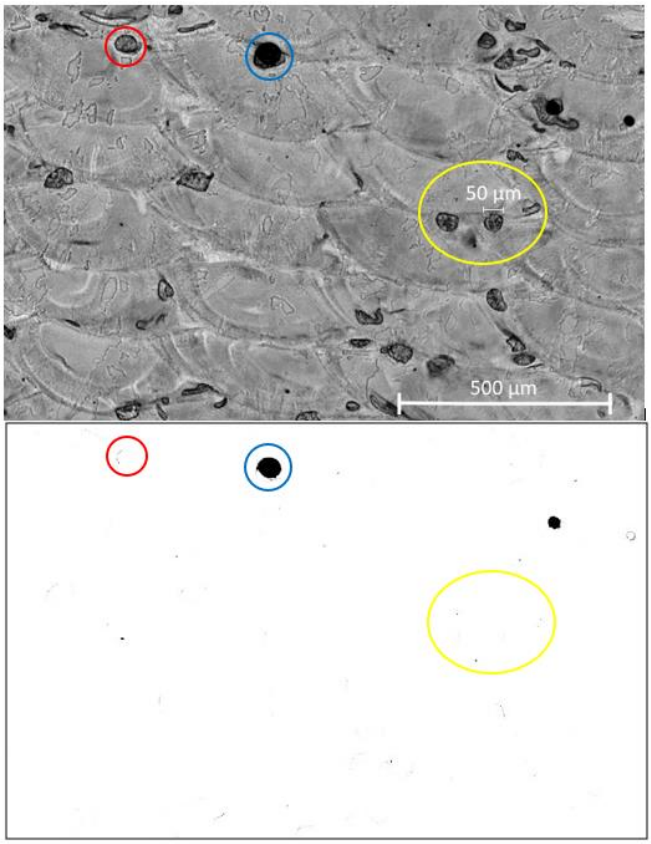

Figure 43. Comparison between the Etched image and porosity image of a zoom-in of Structure 1, type 10 wt% FGM. Note the partially unmolten particles (highlighted in yellow and red circles) uncovered by etching, which minimally influence porosity. Furthermore, note the hollowed out porosity due to etching, in the blue marked areas.

Zooming in on the pores, it becomes apparent that they were often the origin of microcracks, as shown in Figure 44. The cracks originated in the pores due to stress concentrations, since these were the weakest points in the structure. Furthermore, the verticality of the cracks is notable, this is likely due to two factors. The vertical crack formation can be explained by the orientation of horizontal (longitudinal) internal stress, that dissipated in the cracks and ruptured them vertically, as discussed in 2.3.2. Secondly, comparison to the etched figures shows that the cracks often followed grain boundaries. These boundaries were often close to being vertical due to the upward radial grain growth [92].

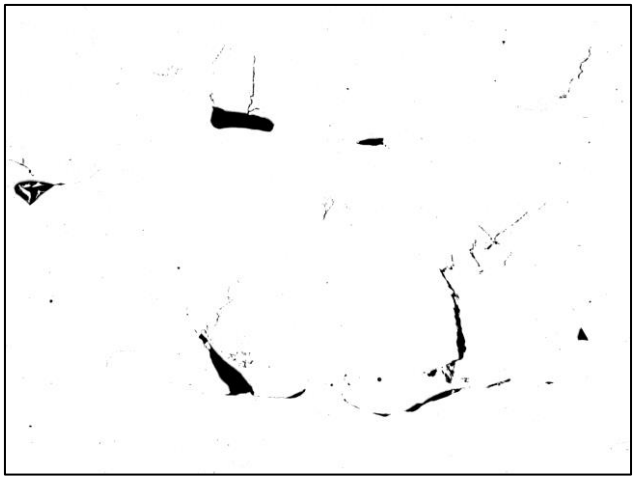

Figure 44. Zoom-in on some porosities found in the first structure of type 10wt% FGM. Note the microcracks originating in the porosities

Finally, the grains in the sections composed of predominantly Inconel crossed the melt-pool borders far more often than the grains in the sections composed of predominantly stainless steel did. This can be seen in, relatively, topside and downside of Structure 1, Figure 42 (1) or in the zoom-ins presented in Figure 45 below, encircled in cyan.

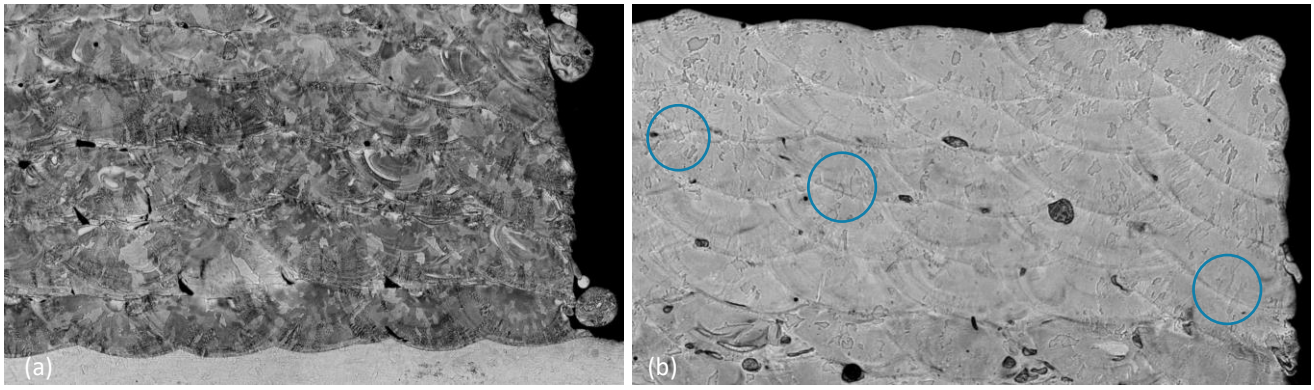

Figure 45. Zoom-ins on Structure 1. Showing the SS316L dominated bottom (a) and the In718 dominated top (b). Note some grains crossing the melt-pool borders in the In718 dominated sections, encircled in cyan.

4.3 Simulation

This study incorporates a comparison of the deformation found in the experiment, as described in section 4.2.1, and the results of thermomechanical simulation, which will be presented in this section. Starting with the thermal simulation and subsequently the mechanical simulation. Both will include a comparison to the experiment and discussion. Finally some simplifications will be discussed.

4.3.1 Thermal simulation

Although the aim of the simulations was to find the deformations after the release step, some interesting observations were made on the thermal history of the subjects.

On the etched cross sections, shown in Figure 42, a higher concentration of unmolten particles was observed in the middle of Structures 1 and 3 and especially in the middle of Structure 2. A logical explanation for the presence of unmolten particles, would be a lower temperature in the middle of the structures, as compared to more lateral regions. In Figure 46, the thermal histories at 4 different locations (a), in the structures 5(b), 1(c) and 2(d) are shown.

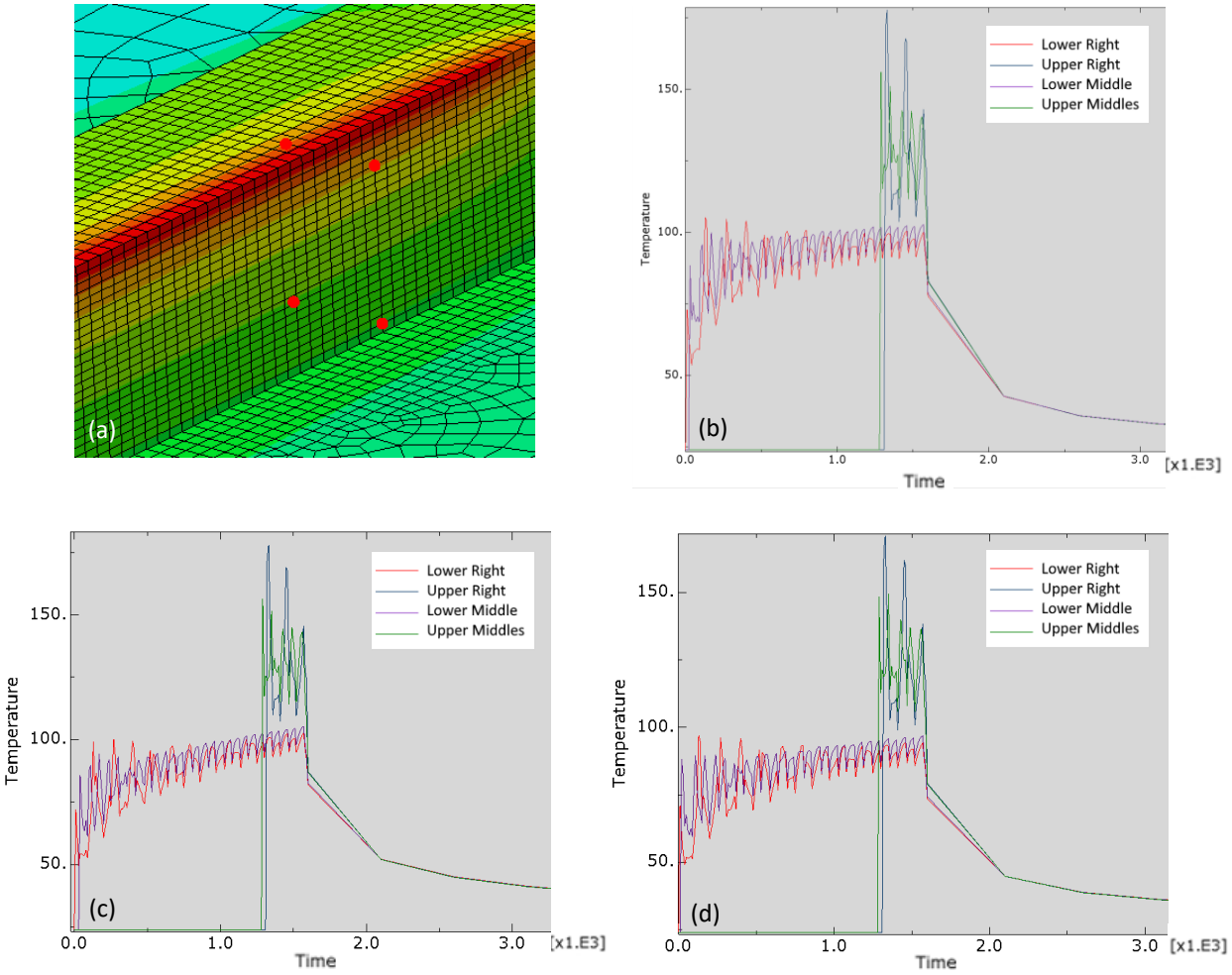

Figure 46. Thermal history results from thermal simulation. (a) Illustration of the points of interest, named according to their position: Lower Right, Upper Right, Lower Middle and Upper middle. (b) Structure 5, type bimetal. (c) Structure 1, type 10 wt% FGM. (d) Structure 2, type 10 wt% FGM. Note the higher temperature at the points on the sides (blue and red figures), compared to the points in the middle (green and purple figures).

Note that, for both the lower regions as the higher regions the thermal history was dependent on the laterality (distance from the centre).

Also note that the temperatures were not high in this simulation relative to the actual experiment, as the temperature was spread out over a larger length. Therefore, it is more suitable to look at the ratio in temperature between the inner dots and outer dots. For Structures 1, 2 (type 10 wt% FGMs) and 4 (bimetal), this temperature difference ratio was

practically the same, all at approximately 10%. This number is quite significant, with melting temperatures of around 1300 ^{0}C for both materials, and could explain the higher unmolten particle density observed in the middle.

An explanation for the lower temperature in the middle, could be the higher conduction for the present elements, as they were surrounded by more elements. The elements at the side did get the effect of convection but this was far weaker by up to a factor 1000 [71]. A slightly lower overall temperature was also expected for the complete bimetal, as this was in the middle of the baseplate and fixation plate, but this seemed neglectable, compared to the other structures.

4.3.2 Mechanical simulation

The first mechanical simulation gave a very twisted result, shown in Appendix B.1. This warping was encountered before in the simulations of Vroon [71]. In AM, some warping can be encountered [95], but the warping found of around 180 ^{0} was clearly not reasonable.

Therefore, a new simulation was conducted, now with a higher ''Expansion Time Constant'' to speed up the process. This constant dictated the time step, during which the expansion and shrinking of the elements occur. To avoid any warping, the rotation about the y-axis and z-axis were fixed. The results are shown in Table 20. The curvatures of deformation, found in the experiments, are added in the final column as well.

Table 20. Comparison of the deformations found in the simulation and experiments for all 7 structures.

structure	Radius Simulation	Curvature Simulation	Curvature Experiment
1 10%	3.59	0.2786	0.2045
2 10%	4.03	0.2481	0.1996
3 20%	4.14	0.2415	0.1775
4 Bimetal	4.30	0.2326	0.1627
5 Bimetal	4.28	0.2336	0.1646
6 In718	3.61	0.2770	0.1753
7 SS316L	4.76	0.2101	0.1600

Firstly, overestimations of the simulated deformations can be noted. This was a new occurrence, since in previous simulations by Vroon, an underestimation was found. This difference is likely due to the higher ''Expansion Time Constant''. The exact reasons for this effect can be subject to further research.

Secondly, The curvatures of the two type 10wt% FGMs were equal in the experiment, but in the simulation the curvature was significantly higher in the most lateral FGM. An explanation for this could be a higher temperature in a more lateral position. By comparing the thermal histories of these FGMs, in Figure 46c and Figure 46d, only a very small temperature difference can be noted, respectively in top-temperature 175 ^{0}C to 170 ^{0}C, a decrease of 3%. This is a very small difference but it was consistent in its entire thermal history and therefore could explain this effect in the simulation.
In the experimental results it is apparent that the curvature of Structure 2 was closer to the curvature of Structure 1, than to the curvature of Structure 3, which was the case in the simulation. The higher curvature of Structure 2 could be attributed to the different thermal histories of the two produced FGMs. Since the production of the first FGM was paused due to a program error at 70% completion, the experiment was fully cooled down to room temperature before

the process was continued. On a second note, and very important for the FGMs, is the time it took to stabilize the mass flow in every switch of composition. Therefore, the produced structures are cooled far more than they are in the simulation.

Furthermore, from the experiments, it was noted that In718 experienced a 9.5% higher deformation compared to SS316L. In the simulation, a similar effect was noted but the deformation of In718 was 31.8% higher. It is important to note other factors from the experiment, such as the deformation present before AM in the arm of the baseplate on which In718 was build, the baseplate could therefore be considered as coldworked and therefore stiffer. Therefore, the deformation of the arms in the experiment could be underestimated for In718. The reason for the higher deformation of In718, despite having a slightly lower CTE, is its higher plasticity values at higher temperatures. These values can be found in Table 21 in Appendix B.2.

Another interesting note is that an overall increase in In718 content led to an increase in curvature in the simulation with the exception of the first structure. In the experiments, a similar effect was observed, however, the highest deformation was not found in the pure In718 build. Again, this was likely due to the already present deformation of the baseplate before AM. An interesting subject for future research could be a bimetal, starting with In718 and then switching to SS316L. This could prove that the upper layers do have a larger impact on deformation due to the moment they can exert.

Finally, the type 10 wt% FGMs were more deformed than the type 20 wt% FGM which were more deformed, compared to the bimetals. This can be explained by two factors. First of all, the In718 percentage in the type 10 wt% FGM was higher, as discussed before; this increased deformation. Secondly, FGMs of this type experience higher internal stresses, compared to bimetals according to a recent study by Rodrigues et al [96]. This study compared internal stresses, with neuron diffraction, in a bimetal composed of In625-SS316L and a 5 wt% sectioned FGM, without skipping the detrimental 25 wt% region. The higher residual stresses can be attributed to intermetallics (carbides), δ-phase (Ni_3Nb) and σ phase. The combination of these intermetallic compounds and phases causes a mismatch in volume and therefore internal stresses. These findings go against the common assumption that FGMs with a smooth transition experience less internal stress. The structures in this thesis have been optimized by leaving out the 25 wt% region but from the microstructural analysis it became clear that the occurrence of intermetallics in the 10 wt% section is still likely, since a significantly higher porosity was observed in this region. Furthermore, the phase transitions will of course be far more present in the FGMs, as compared to the bimetals. Also, according to Rodrigues et al., the internal stress is highest around 55 wt% In625. This is an interesting result, as this is not the region with the highest porosity, but the mismatch between the phases in this region most likely translates into internal stress instead of porosity.

4.3.3 Simplifications

The mayor subject of this thesis is to find the deformations in a AM build structure of a relative large size (not just a few tracks). This meant that a lot of tracks had to be modelled and this would be very computationally intensive. Despite the extensive computational server facility, which possesses a 256 Cores CPU, a melt-pool size simulation would take weeks to run. Therefore, the model had to be simplified with a larger expansion time constant of 20 s to 500 s. The laser-energy in this time period would be distributed equally over a larger area. This is quite a simplification but in recent research by Koenis also from the NLR this was concluded to be an acceptable simplification as long as calibration has been applied. No further literature is found on this subject.

Furthermore, the material properties have been linearized. However, the microstructure revealed a clear mixing of the In718 and SS316L materials, therefore different phases will occur with different material properties. The estimation of material properties could be improved by further microstructural research to find the volume fractions (material composition). This could be fitted with MicroFEA 1.0 software as discussed in 2.4.2.3 to improve the simulations in Abaqus.

5 Conclusions

Conclusions concerning the research questions:

- The porosity of the FGMs without the 20-30wt% In718 region was considerable better than the results in the previous study at the Royal NLR. And in general, the porosities of all structures range between 0.01% and 0.05%, which can be considered of very good quality.
- Few microcracks were present, all originating from pores but not at random in the matrix.
- Lower porosity was observed in the type 20 wt% FGM as opposed to the type 10 wt% FGMs. The latter contained still some pores in the 10 wt% In718 region (Table 19). Therefore, it can be concluded it is best to leave out the whole sub-40 wt% In718 region, opposed to just leaving out the 20-30 wt% region, to reduce porosity.
- Type 10 wt% FGMs and to a lesser extent type 20wt% FGMs experience higher internal stress, compared to bimetals. This effect was found in the simulation as well as in the experiment.
- The simulation overestimated the deformations but was mostly congruent with the experimental results, although multiple factors need to be taken into account, such as the deformation of the baseplate before AM.

Mass flow:

- It takes around 2 minutes to fully stabilize the mass flow.
- The combined mass flow of the In718 and SS316L powders differs from the sum of the calibrated individual mass flows. And this effect is not congruent. The higher the In718 constituent, the lower the mass flow will be. This could be contributed to the 'sticky' behaviour of the In718.

Microstructural:

- The grains in the ranges composed of predominantly Inconel crossed the melt-pool borders far more often than in the regions composed of predominantly stainless steel.
- AM SS316L is more easily etched than the baseplate composed of rolled 316L stainless steel, due to different microstructural phases, these are yet to be determined.
- Stainless steel experienced a drop-off on the sides; in other words, the structures were arc-shaped. This could be explained by a lower viscosity on the sides, due to a higher temperature, and because SS316L is a lot weaker at higher temperatures, thus being lower in viscosity.
- Between the individual compositional sections small oxidized layers were observed. This can be attributed to the stabilization time needed before each new section.
- The turbulent flow of the melt pool mixes different compositional sections and can be seen as rings at a few positions in the microstructure, especially in Structure 6 at the bottom and in Structure 3 between the sections.
- Partially molten particles were observed in the type 10 wt% and type 20wt% FGMs as black dots in the etched images. This is logical, since In718 has a higher melting temperature. However this phenomenon is not observed in the pure Inconel build. Therefore, it must be due to the different material composition.
- The produced structures were larger than expected, 5.8 mm in both height and width, as compared to the expected 4.8 mm. This is most likely due to the different mass flow characteristics of the combined mass flow as compared to the individual mass flows or a higher powder absorption in the melt pool.

Thermal simulation:

- The thermal history of the inside of the simulated structures was consistently 10% lower compared to the outside. This can be attributed to the convection being a weaker factor compared to conduction

- The thermal histories of the different structures do depend slightly on the position; a 3% difference can be noted between the first and second identical type 10 wt% FGMs. Furthermore, the bimetal has a slightly higher thermal history, so the composition does have a small influence on the thermal history as well.

Mechanical simulation:

- From the experiments, it was noted that In718 was 9.5% more deformed compared to SS316L. In the simulation a similar effect was noted but with a difference of 31.8%. It is important to note other factors in the experiment, such as an already present deformation in the arm of the baseplate, on which In718 was build. This could therefore be considered as cold-worked and therefore stiffer.
- Increasing the In718 composition increases deformation.
- Finally, the type 10 wt% FGMs were more deformed than the type 20wt% FGM, which were more deformed compared to the bimetals. This can be partially attributed to the higher In718 percentage in the FGMs. But this result is also congruent with other literature on internal stresses which found higher internal stresses in the FGMs compared to bimetals but attribute this to precipitates and phases causing a mismatch in volume and therefore internal stresses. These findings go against the common assumption, that the production of FGMs with a smooth transition results in less deformation.

6 Recommendations

Mass flow

- Further analysis of the combined mass flow is highly recommended as the characteristics of this flow do not seem to be in a linear relation to the individual mass flows.
- A further analysis of the scale is recommended as the fluctuations of the mass flow were very notable.

Additive manufacturing

- It is recommended to omit the entire range of 0-40wt% In718, as high porosity was still observed in this region. This porosity has similar characteristics to the intermetallics-induced porosity of 20-30 wt% and can therefore hardly be improved by changing the process parameters.
- A dry test run before printing can be considered to avoid the experienced halts during printing.
- Measurement of the deformation of the baseplate before printing is highly recommended. As deformation can be present due to the water-cutting, preferably a 3D scan is to be performed prior to AM to compare the image data with the 3D scan after AM.
- Use a baseplate with as little as possible thermomechanical history. Laser-cutting is not an option due to the heat input but maybe the deformation due to water cutting can be decreased with a stiffer set-up.
- Increase the laser-power in the In718 dominated regions to avoid partially molten particles.
- Research on the mechanical properties of the individual alloys could be conducted by making tensile specimens consisting of only one alloy.
- The effect of transitioning from one alloy to another, on the mechanical properties could be examined, by taking tensile specimens of an FGM.
- The previous recommendation could be extended to compare the effect of transitioning in a smoother fashion (10-20 wt% increments) to a more abrupt transition (bimetal).
- Further research could be conducted on a bimetal starting with a lower section of In718 and thereafter switching to SS316L, to find if the top regions do have a relative higher impact on deformation, compared to lower regions.

Microstructural analysis

- Use a reagent composed of 40 vol% hydrochloric acid (HCl), 13.8 vol% nitric acid (HNO_3) and 46.2 vol% water as this was found to give the best results for both SS316L and In718.
- SS316L is reacting more quickly relatively to the In718 alloy. Therefore, for optimal microstructural results, it is recommended to capture an image for an optimal SS316L etching. Thereafter, capture an image at the optimal trade-off between the etched materials and finally capture an image of the optimally etched In718.
- SEM analysis can be performed on the etched cross sections from this thesis project to further analyse grains and phases.

Simulation

- The application of a rougher mesh is recommended, as the simulations of this kind are very computational intensive, a data file size of 60 GB was not uncommon in the simulations of this thesis.
- To avoid excessive warping fixate the displacement around the x-axis. The fixation of rotation about the y-axis and z-axis does not solve this problem.
- In the production of the FGMs, the composition is changed per section and every change requires up to 2 minutes of stabilization time. This should be taken into account in the thermal history of the experiment. Furthermore, the process

can be stopped due to unexpected (software) errors. Therefore, it is recommended to create a thermal simulation after the experiment to represent the experiment with the highest fidelity.

- Further research can be conducted on the effect of the step size, as this basically spreads out the energy input over a larger length.
- The positive correlation between the ‘’Expansion Time Constant’’ and deformation is an important topic for further research.
- If further microstructural research is conducted to find the volume fractions (material composition). This could be fitted with MicroFEA 1.0 software to improve the simulations in Abaqus.

7 References

[1] V. Bhavar, P. Kattire, S. Thakare, S. patil, and R. Singh, "A review on functionally gradient materials (FGMs) and their applications," *IOP Conference Series: Materials Science and Engineering*, vol. 229, p. 012021, 2017.

[2] Metal AM, "Materialise Magics: Advanced part orientation and support solutions to speed up application development." https://www.metal-am.com/articles/materialise-magics-advanced-part-orientation-and-support-solutions-3d-printing/, 2021. Accessed: 15-07-2022.

[3] J. Kelly, J. Elmer, F. Ryerson, J. Lee, and J. Haslam, "Directed energy deposition additive manufacturing of functionally graded al-w composites," *Additive Manufacturing*, vol. 39, p. 101845, Mar 2021.

[4] P. Breedveld, J. L. Herder, and T. Tomiyama, "2: Teaching for creativity and teaching creatively," *Primary Design and Technology for the Future*, p. 24–41, 2013.

[5] R. Larsson, *Methodology for Topology and Shape Optimization: Application to a Rear Lower Control Arm*. PhD thesis, Chalmers, 2016.

[6] S. Ji, Z. Sun, W. Zhang, X. Chen, G. Xie, and H. Chang, "Microstructural evolution and high temperature resistance of functionally graded material ti-6al-4v/inconel 718 coated by directed energy deposition-laser," *Journal of Alloys and Compounds*, vol. 848, p. 156255, Dec 2020.

[7] S. Valkov, M. Ormanova, and P. Petrov, "Electron-beam surface treatment of metals and alloys: Techniques and trends," *Metals*, vol. 10, no. 9, p. 1219, 2020.

[8] X. S. Zhang, H. Chi, and G. H. Paulino, "Adaptive multi-material topology optimization with hyperelastic materials under large deformations: A virtual element approach," *Computer Methods in Applied Mechanics and Engineering*, vol. 370, p. 112976, 2020.

[9] C. Kim, H. K. Seong, I. Y. Kim, and J. Yoo, "Single variable-based multi-material structural optimization considering interface behavior," *Computer Methods in Applied Mechanics and Engineering*, vol. 367, p. 113114, 2020.

[10] "Metal Additive Manufacturing producs & Services." NLR. Accessed: 06-07-2022. [Online]. Available: https://www.nlr.org/flyers/en/f401-metal-additive-manufacturing.pdf

[11] "NLR mission and vision," NLR, Accessed 06-07-2022. https://www.nlr.org/about-us/mission-and-vision/

[12] E. Amsterdam, "Selective laser melting of multiple materials," NLR, Amsterdam, Experimental study NLR-CR-2015-520, Jan. 2018.

[13] J. Edgar and S. Tint, ""additive manufacturing technologies: 3d printing, rapid prototyping, and direct digital manufacturing", 2nd edition," *Johnson Matthey Technology Review*, vol. 59, no. 3, p. 193–198, 2015.

[14] F. Calignano, D. Manfredi, E. P. Ambrosio, S. Biamino, M. Lombardi, E. Atzeni, A. Salmi, P. Minetola, L. Iuliano, P. Fino, and et al., "Overview on additive manufacturing technologies," *Proceedings of the IEEE*, vol. 105, no. 4, p. 593–612, 2017.

[15] HUBS, "What is 3d printing? how does 3d printing work?." https://www.hubs.com/ guides/3d-printing/, GEN3D, 2021. Accessed: 09-12-2021.

[16] J. Lanters, "Exploration of producing functionally graded materials using laser-based powder-blown directed energy deposition," Master's thesis, NLR, 2021.

[17] A. Bandyopadhyay and B. Heer, "Additive manufacturing of multi-material structures," *Materials Science and Engineering: R: Reports*, vol. 129, p. 1–16, 2018.

[18] O. O. Brovko, P. Ruiz-Díaz, T. R. Dasa, and V. S. Stepanyuk, "Controlling magnetism on metal surfaces with non-magnetic means: Electric fields and surface charging," *Journal of Physics: Condensed Matter*, vol. 26, p. 093001, Feb 2014.

[19] H. Zhang, J. Ding, G. Chow, M. Ran, and J. Yi, "Engineering magnetic properties of ni nanoparticles by non-magnetic cores," *Chemistry of Materials*, vol. 21, no. 21, p. 5222–5228, 2009.

[20] N. Putra, M. Mirzaali, I. Apachitei, J. Zhou, and A. Zadpoor, "Multi-material additive manufacturing technologies for ti-, mg-, and fe-based biomaterials for bone substitution," *Acta Biomaterialia*, vol. 109, p. 1–20, Jun 2020.

[21] S. Banait, C. Paul, A. Jinoop, H. Kumar, R. Pawade, and K. Bindra, "Experimental investigation on laser directed energy deposition of functionally graded layers of ni-cr-bsi and ss316l," *Optics & Laser Technology*, vol. 121, p. 105787, 2020.

[22] L. D. Bobbio, B. Bocklund, R. Otis, J. P. Borgonia, R. P. Dillon, A. A. Shapiro, B. McEnerney, Z.-K. Liu, and A. M. Beese, "Characterization of a functionally graded material of ti-6al-4v to 304l stainless steel with an intermediate v section," *Journal of Alloys and Compounds*, vol. 742, p. 1031–1036, Jan 2018.

[23] W. Li, S. Karnati, C. Kriewall, F. Liou, J. Newkirk, K. M. Brown Taminger, and W. J. Seufzer, "Fabrication and characterization of a functionally graded material from ti-6al4v to ss316 by laser metal deposition," *Additive Manufacturing*, vol. 14, p. 95–104, Feb 2017.

[24] Aalco datasheets, '' Aluminium Alloy - Commercial Alloy - 5754 - H22 Sheet and Plate'' www.aalco.co.uk/datasheets/Aluminium-Alloy-5754-H22-Sheet-and-Plate_153.ashx, nov, 2018.

[25] Materialise, "Datasheets 3d printing materials," https://www.materialise.com/en/manufacturing/materials/aluminum, Mar 2021.

[26] H. Hotz, M. Zimmermann, S. Greco, B. Kirsch, and J. C. Aurich, "Additive manufacturing of functionally graded ti-al structures by laser-based direct energy deposition," *Journal of Manufacturing Processes*, vol. 68, p. 1524–1534, Aug 2021.

[27] E. O. Olakanmi, M. Sepako, J. Morake, S. E. Hoosain, and S. L. Pityana, "Microstructural characteristics, crack frequency and diffusion kinetics of functionally graded ti-al composite coatings: Effects of laser energy density (led)," *JOM*, vol. 71, no. 3, p. 900–911, 2019.

[28] J. Wang, Z. Pan, Y. Ma, Y. Lu, C. Shen, D. Cuiuri, and H. Li, "Characterization of wire arc additively manufactured titanium aluminide functionally graded material: Microstructure, mechanical properties and oxidation behaviour," *Materials Science and Engineering: A*, vol. 734, p. 110–119, 2018.

[29] F. Wagner, M. Kreimeyer, R. Kocik, and F. Vollertsen, "Laser joining of aluminum to titanium with focus on aeronautical applications," *Pacific International Conference on Applications of Lasers and Optics*, 2006.

[30] A. Kar, S. K. Choudhury, S. Suwas, and S. V. Kailas, "Effect of niobium interlayer in dissimilar friction stir welding of aluminum to titanium," *Materials Characterization*, vol. 145, p. 402–412, 2018.

[31] K. Shah, A. Pinkerton, R. Moat, L. Li, and M. Preuss, "Direct diode laser deposition of functionally graded ti-6al-4v and inconel 718 components," *Pacific International Conference on Applications of Lasers and Optics*, p. 273, 2008.

[32] K. I. Makarenko, O. N. Bubinin, S. D. Konev, and I. V. Shishkovsky, “Physical and mechanical properties of cu-fe system functionally graded and multimaterial structures after the ded,” Skolkovo Institute of Science and Technology, Sep 2021.

[33] K. I. Makarenko and I. V. Shishkovsky, “Direct energy deposition of cu-fe system functionally graded structures,” IOP Conference Series: Materials Science and Engineering, vol. 969, no. 1, p. 012104, 2020.

[34] E. E. Feldshtein, O. Devojno, M. Kardapolava, N. Lutsko, and J. Patalas-Maliszewska, “On the features of composite coating, based on nickel alloy and aluminum–iron bronze, processed by direct metal deposition,” Materials, vol. 14, no. 4, p. 957, 2021.

[35] S. H. Kim, H. Lee, S. M. Yeon, C. Aranas, K. Choi, J. Yoon, S. W. Yang, and H. Lee, “Selective compositional range exclusion via directed energy deposition to produce a defect-free inconel 718/ss 316l functionally graded material,” *Additive Manufacturing*, vol. 47, p. 102288, Nov 2021.

[36] D. Feenstra, R. Banerjee, H. Fraser, A. Huang, A. Molotnikov, and N. Birbilis, “Critical review of the state of the art in multi-material fabrication via directed energy deposition,” *Current Opinion in Solid State and Materials Science*, vol. 25, no. 4, p. 100924, 2021.

[37] B. Chen, Y. Su, Z. Xie, C. Tan, and J. Feng, “Development and characterization of 316l/inconel625 functionally graded material fabricated by laser direct metal deposition,” *Optics & Laser Technology*, vol. 123, p. 105916, Oct 2020.

[38] L. Yan, Y. Chen, and F. Liou, “Additive manufacturing of functionally graded metallic materials using laser metal deposition,” *Additive Manufacturing*, vol. 31, p. 100901, 2020.

[39] D. R. Feenstra, A. Molotnikov, and N. Birbilis, “Effect of energy density on the interface evolution of stainless steel 316l deposited upon inc 625 via directed energy deposition,” *Journal of Materials Science*, vol. 55, no. 27, p. 13314–13328, 2020.

[40] W. Woo, D.-K. Kim, E. Kingston, V. Luzin, F. Salvemini, and M. R. Hill, “Effect of interlayers and scanning strategies on through-thickness residual stress distributions in additive manufactured ferritic-austenitic steel structure,” *Materials Science and Engineering: A*, vol. 744, p. 618–629, 2019.

[41] R. A., M. O. V., and J. R., “Additive manufacturing of nickel-based super alloys for aero engine applications,” *Advances in Civil and Industrial Engineering*, vol. 1, p. 48–70, Jun 2020.

[42] D. R. Askeland and W. J. Wright, The Science and Engineering of Materials, p. 387–389. Cengage Learning, 2016.

[43] X. Lu, X. Lin, M. Chiumenti, M. Cervera, J. Li, L. Ma, L. Wei, Y. Hu, and W. Huang, “Finite element analysis and experimental validation of the thermomechanical behavior in laser solid forming of ti-6al-4v,” *Additive Manufacturing*, vol. 21, p. 30–40, May 2018.

[44] K. Swaminathan and D. M. Sangeetha, “Thermal analysis of fgm plates – a critical review of various modeling techniques and solution methods,” *Composite Structures*, vol. 160, p. 43–60, 2017.

[45] T. Q. Bui, T. van Do, L. H. That Ton, D. H. Doan, S. Tanaka, D. T. Pham, T. NguyenVan, T. Yu, and S. Hirose, “On the high temperature mechanical behaviors analysis of heated functionally graded plates using fem and a new third-order shear deformation plate theory,” *Composites Part B: Engineering*, vol. 92, p. 218–241, 2016.

[46] H. Ziou, G. Hamza, and M. Guenfoud, “Numerical modelling of a timoshenko fgm beam using the finite element method,” *International Journal of Structural Engineering*, vol. 7, p. 239, 01 2016.

[47] J. Murin, M. Aminbaghai, and V. Kutis, “Exact solution of the bending vibration problem of fgm beams with variation of material properties,” *Engineering Structures - ENG STRUCT*, vol. 32, pp. 1631–1640, 06 2010.

[48] K. Tanaka, Y. Tanaka, H. Watanabe, V. Poterasu, and Y. Sugano, “An improved solution to thermoelastic material design in functionally gradient materials: Scheme to reduce thermal stresses,” *Computer Methods in Applied Mechanics and Engineering*, vol. 109, no. 3, pp. 377–389, 1993.

[49] S. N. Ahmad, Y. H. Manurung, M. F. Mat, Z. Minggu, A. Jaffar, S. Pruller, and M. Leitner, “Fem simulation procedure for distortion and residual stress analysis of wire arc additive manufacturing,” *IOP Conference Series: Materials Science and Engineering*, vol. 834, no. 1, p. 012083, 2020.

[50] M. E. Stender, L. L. Beghini, J. D. Sugar, M. G. Veilleux, S. R. Subia, T. R. Smith, C. W. Marchi, A. A. Brown, and D. J. Dagel, “A thermal-mechanical finite element workflow for directed energy deposition additive manufacturing process modeling,” *Additive Manufacturing*, vol. 21, p. 556–566, May 2018.

[51] Q. Yang, P. Zhang, L. Cheng, Z. Min, M. Chyu, and A. C. To, “Finite element modeling and validation of thermomechanical behavior of ti-6al-4v in directed energy deposition additive manufacturing,” *Additive Manufacturing*, vol. 12, p. 169–177, Oct 2016.

[52] A. KIRAN, J. HODEK, J. VAVŘÍK, O. LUKÁŠ, and M. URBÁNEK, “Distortion modelling of steel 316l symmetric baseplate for additive manufacturing process and experimental calibration,” *METAL 2020 Conference Procedings*, vol. 29, p. 862–867, May 2020.

[53] H. Liu, Z. Liu, Y. Qiu, G. Cao, C. Li, and G. Wang, “Characterization of the solidification structure and texture development of ferritic stainless steel produced by twin-roll strip casting,” *Materials Characterization*, vol. 60, no. 1, p. 79–82, 2009.

[54] K. M. Kulkarni, “Review of forging, stamping, and other solid-phase forming processes,” *Polymer Engineering and Science*, vol. 19, no. 7, p. 474–481, 1979.

[55] P. Michaleris, “Modeling metal deposition in heat transfer analyses of additive manufacturing processes,” *Finite Elements in Analysis and Design*, vol. 86, p. 51–60, 2014.

[56] M. Bayat, W. Dong, J. Thorborg, A. C. To, and J. H. Hattel, “A review of multi-scale and multi-physics simulations of metal additive manufacturing processes with focus on modeling strategies,” *Additive Manufacturing*, vol. 47, p. 102278, Nov 2021.

[57] Y. Watanabe, P. D. Sequeira, H. Sato, T. Inamura, and H. Hosoda, “Aluminum matrix texture in al–al3ti functionally graded materials analyzed by electron back-scattering diffraction,” *Japanese Journal of Applied Physics*, vol. 55, no. 1S, 2015.

[58] M. S. Medeiros and E. Parente, “Microfea 1.0 — a software package for finite element analysis of functionally graded materials,” SoftwareX, vol. 11, p. 100481, 2020.

[59] S. J. Tabatabaei and A. M. Fattahi, “A finite element method for modal analysis of fgm plates,” *Mechanics Based Design of Structures and Machines*, vol. 50, p. 1–12, 2020.

[60] H. Ziou, H. Guenfoud, and M. Guenfoud, “Numerical modelling of a timoshenko fgm beam using the finite element method,” *International Journal of Structural Engineering*, vol. 7, p. 239, Nov 2016.

[61] J. Murín, M. Aminbaghai, and V. Kutiš, “Exact solution of the bending vibration problem of fgm beams with variation of material properties,” *Engineering Structures*, vol. 32, no. 6, p. 1631–1640, 2010.

[62] C. Aksoylar, A. Ömercikoğlu, Z. Mecitoğlu, and M. H. Omurtag, “Nonlinear transient analysis of fgm and fml plates under blast loads by experimental and mixed fe methods,” *Composite Structures*, vol. 94, no. 2, p. 731–744, 2012.

[63] B. Onuike and A. Bandyopadhyay, “Additive manufacturing of inconel 718 – ti6al4v bimetallic structures,” *Additive Manufacturing*, vol. 22, p. 844–851, 2018.

[64] Maher, “titanium-6al-4v-datasheet.” https://www.maher.com/media/pdfs/ titanium-6Al-4V-datasheet.pdf. Accessed: 10-11-2021.

[65] MatWeb, “Material properties in718.” http://www.matweb.com/search/datasheet_ print.aspx?matguid=94950a2d209040a09b89952d45086134. Accessed: 10-11-2021.

[66] MatWeb, “Material properties titanium ti-6al-4v (grade 5), annealed.” http://www.matweb.com/search/DataSheet.aspx?MatGUID= b350a789eda946c6b86a3e4d3c577b39&ckck=1. Accessed: 10-11-2021.

[67] G. Magnetics, “What is the difference between the magnetic properties of 304 and 316 stainless steel?.” https://www.greenwoodmagnetics.com/resource/ what-is-the-difference-between-304-and-316-stainless-steel/. Accessed: 1711-2021.

[68] MatWeb, “Material properties ss316l.” http://www.matweb.com/search/datasheet_ print.aspx?matguid=1336be6d0c594b55afb5ca8bf1f3e042. Accessed: 17-11-2021.

[69] E. S. A. (ESA), “Material properties stainless steel aisi 316l.” http://esmat.esa.int/ Services/Preferred_Lists/Materials_Lists/a63.htm. Accessed: 17-11-2021.

[70] Upmet, “Properties stainless steel types 316, 316l, 317, 317l.” https://www.upmet.com/ sites/default/files/datasheets/316-316l.pdf. Accessed: 17-11-2021.

[71] J. Vroon, ‘’Simulation of Additive Manufacturing (title to be decided)’’, unpublished.

[72] T. Osinga, ‘’Three massflows through the nozzle in the BeAM M400’’, 28-06-2022.

[73] M. L. Montero, T. Osinga, “Mass flow calibration” Personal conversation, 20-06-2022.

[74] Dassault Systemes, ‘’Box toolpath-mesh intersection’’, guideline. https://help.3ds.com/2020/english/DSSIMULIA_Established/SIMACAEANLRefMap/simaanl-c-amtoolpathmeshintersect-box-toolpath.htm?contextscope=all&id=2c3a27bcfa3f4a32be0ce67751bd7ad8. Accessed: 15-08-2022.

[75] Dassault Systemes, ‘’ABQ_AM_MovingHeatSource_Advanced’’, guideline. https://help.3ds.com/2020/english/DSSIMULIA_Established/SIMACAEANLRefMap/simaanl-c-amspecialpurpose-type-heatsource-advanced.htm?contextscope=all. Accessed: 15-08-2022.

[76] T. Koenis, ‘’Effect of parameters on DED and SLM simulation, Presentation document, 2020.

[77] E. Hosseini and V. Popovich, “A review of mechanical properties of additively manufactured inconel 718”, Additive Manufacturing, vol. 30, p. 100877, 2019.

[78] J.K. Solberg, ‘’The influence of carbon and nitrogen on the high temperature creep properties of AISI type 316 austenitic stainless steel’’, Materials Science and Engineering, vol. 50, p. 39-44, 1982.

[79] K. Yuan, W. Guo, P. Li, Y. Zhang, X. Li, and X. Lin, “Thermomechanical behavior of laser metal deposited inconel 718 superalloy over a wide range of temperature and strain rate: Testing and constitutive modeling,” Mechanics of Materials, vol. 135, p. 13–25, 2019.

[80] S. Medeiros, Y. Prasad, W. Frazier, and R. Srinivasan, “Microstructural modeling of metadynamic recrystallization in hot working of in 718 superalloy,” Materials Science and Engineering: A, vol. 293, no. 1-2, p. 198–207, 2000. Literature Review A.D.D. van der Eems

[81] J. Zhang, Z. Gao, J. Zhuang, Z. Zhong, and P. Janschek, “Strain-rate hardening behavior of superalloy in718,” Journal of Materials Processing Technology, vol. 70, no. 1-3, p. 252–257, 1997.

[82] K. Prasad, R. Sarkar, P. Ghosal, and V. Kumar, “Tensile deformation behaviour of forged disc of in 718 superalloy at 650°c,” Materials amp; Design, vol. 31, no. 9, p. 4502–4507, 2010.

[83] L. Cheng, X. Xue, B. Tang, D. Liu, J. Li, H. Kou, and J. Li, “Deformation behaviour of hot-rolled in718 superalloy under plane strain compression at elevated temperature,” Materials Science and Engineering: A, vol. 606, p. 24–30, 2014.

[84] A. Thomas, M. El-Wahabi, J. Cabrera, and J. Prado, “High temperature deformation of inconel 718,” Journal of Materials Processing Technology, vol. 177, no. 1-3, p. 469–472, 2006.

[85] H. Xue, W. Lijun, X. Hui, L. Runguang, W. Shaogang, and C. Zhonglin, “Superplastic properties of inconel 718,” Journal of Materials Processing Technology, vol. 137, no. 1-3, p. 17–20, 2003.

[86] E.S. Puchi Cabrera, ‘’High temperature deformation of 316L stainless steel’’, Materials Science and Technology, 17:2, 155-161, DOI: 10.1179/026708301101509944.

[87] Simufact, ‘’Inconel properties’’, Material Database Software, Accessed: 05-05-2022.

[88] P. Aba-Perea, T. Pirling, P. Withers, J. Kelleher, S. Kabra, and M. Preuss, “Determination of the high temperature elastic properties and diffraction elastic constants of ni-base superalloys,” Materials amp; Design, vol. 89, p. 856–863, 2016.

[89] A. S. Agazhanov, D. A. Samoshkin, and Y. M. Kozlovskii, “Thermophysical properties of inconel 718 alloy,” Journal of Physics: Conference Series, vol. 1382, no. 1, p. 012175, 2019.

[90] PlanetCalc, ‘’ Equation of a circle passing through 3 given points’’ https://planetcalc.com/8116/. Accessed: 15-07-2022.

[91] J. Vroon and J. Zhou, “Discussion Microstructural analysis” Personal conversation, 08-08-2022.

[92] M. L. Montero, “Discussion Microstructural analysis” Personal conversation, 09-08-2022.

[93] A. van der Eems, N. Jimenez, M. L. Montero, M. de Smit, and J. Vroon, “Discussion Microstructural analysis”, Introductory meeting CRM Group and Royal NLR, 22-08-2022.

[94] M. L. Montero, T. Ossinga, “Discussion Microstructural analysis and continuation of the study” Personal conversation, 25-08-2022.

[95] B. Redwood, F. Schöffer and B Garret, ‘’The 3d printing Handbook’’, Coers & Roest, p. 149-152, DOI: 978-90-827485-0-5, 2020.

[96] T. A. Rodrigues, F.W. Cipriano Farias, K. Zhang, A. Shamsolhodaei, J. Shen, N. Zhou, N. Schell, J. Capek, E. Polatidis, T. G. Santos, J. P. Oliveira, Wire and Arc Additive Manufacturing of Stainless Steel 316L/Inconel 625 Functionally Graded Material: Development and Characterization, Journal of Materials Research and Technology,

https://doi.org/10.1016/j.jmrt.2022.08.169.

Appendix A Additive manufacturing

Appendix A.1 DED in operation

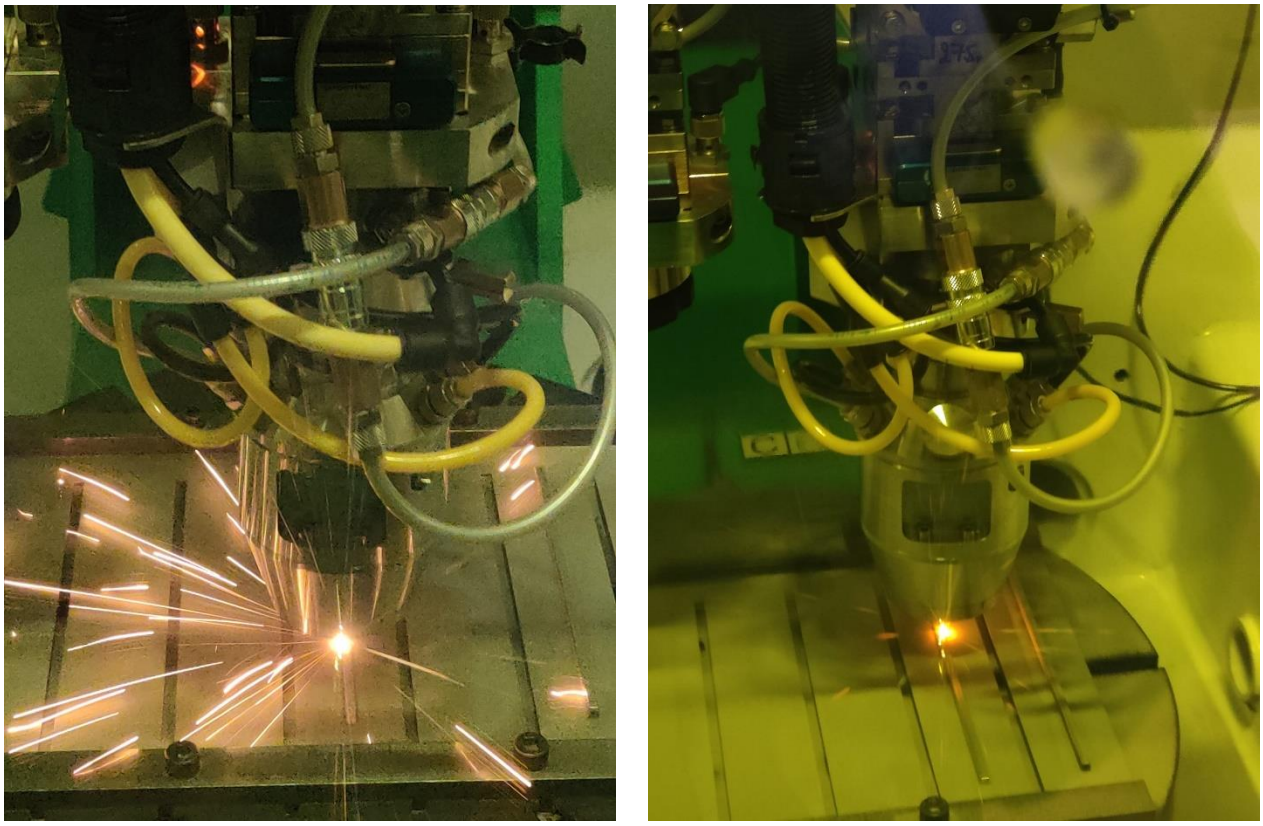

Figure 47. AM of a layer of pure SS316L in the bimetal structure. (b) AM of a layer of pure In718 in the pure In718 structure. Note the considerable less sparks in the In718 build, as it experiences less oxidation.

Appendix A.2 3D scan

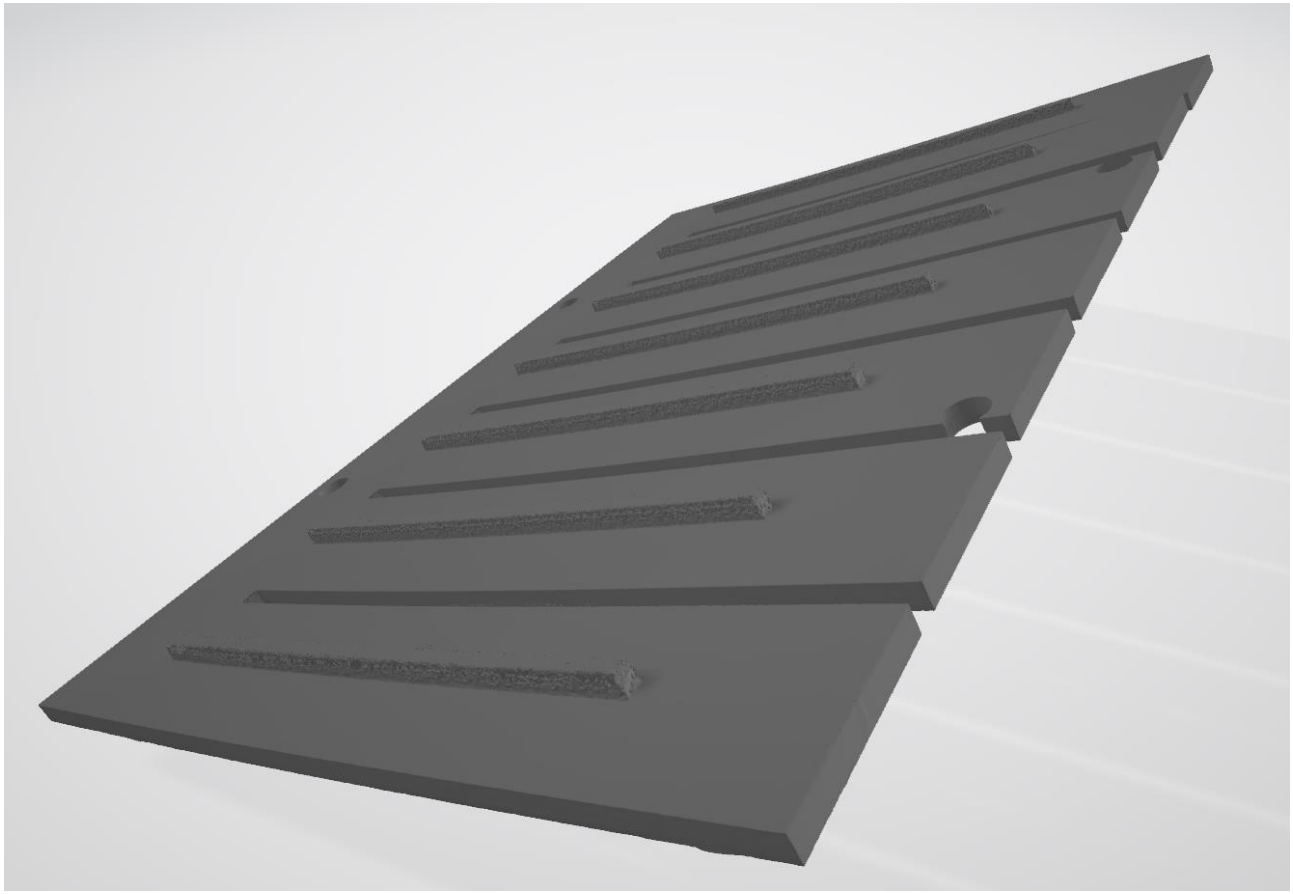

Figure 48. 3D scan of the experimental AM build

Appendix B Simulation

Appendix B.1 Warped results from the first mechanical simulation

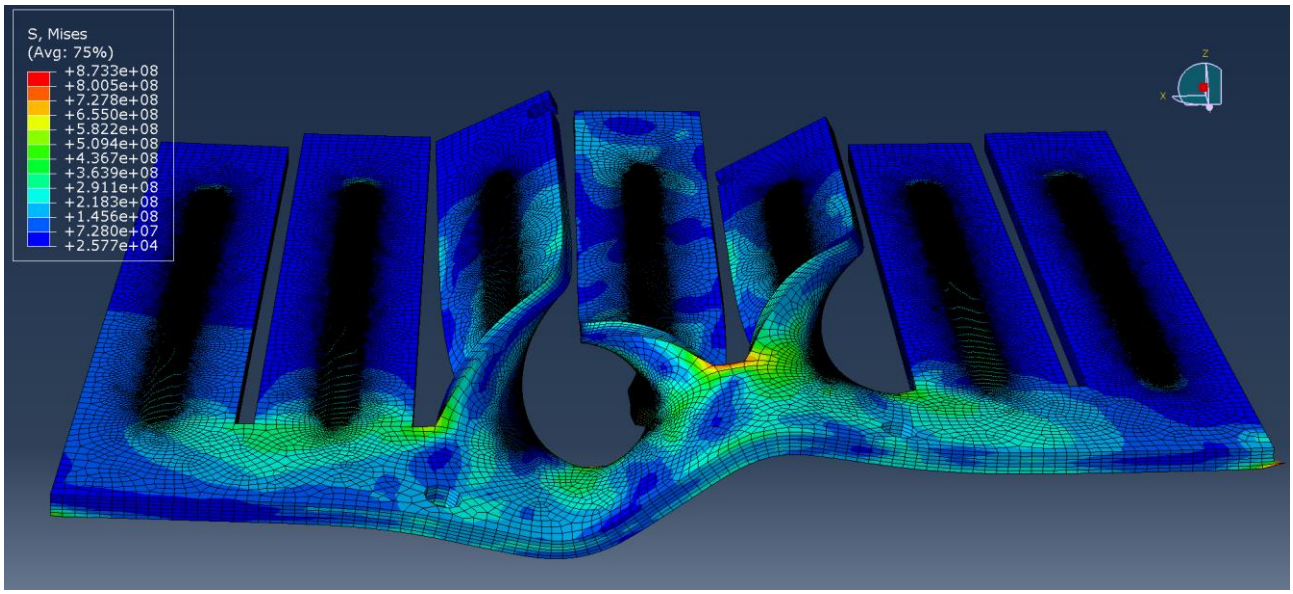

Figure 49. Result of the first computed mechanical simulation. Showing a large warping effect.

Appendix B.2 Stress strain data

Table 21. Plasticity data used in the thermomechanical simulation

Plasticity SS316L			**Plasticity In718**		
Stress (Mpa)	Strain	Temperature (°C)	Stress (Mpa)	Strain	Temperature (°C)
325	0	20	649.06	0	20
393	0.05	20	851.75	0.05	20
494	0.1	20	935.85	0.1	20
648	0.2	20	1073.85	0.2	20
775	0.3	20	1203.23	0.3	20
880	0.4	20	1302.43	0.4	20
249	0	300	480.86	0	300
325	0.05	300	698.65	0.05	300

424	0.1	300	851.75	0.1	300
544	0.2	300	1011.32	0.2	300
575	0.3	300	1136.39	0.3	300
575	0.4	300	1220.49	0.4	300
211	0	550	480.86	0	550
286	0.05	550	711.59	0.05	550
380	0.1	550	812.94	0.1	550
480	0.2	550	953.1	0.2	550
500	0.3	550	1073.85	0.3	550
500	0.4	550	1183.83	0.4	550
140.2	0	850	396.77	0	850
182.1	0.05	850	470.08	0.05	850
229.6	0.1	850	506.74	0.1	850
247.4	0.2	850	556.33	0.2	850
260.5	0.3	850	601.62	0.3	850
265.8	0.4	850	640.43	0.4	850
76.7	0	1000	288.95	0	1000
99.6	0.05	1000	321.29	0.05	1000
125.6	0.1	1000	364.42	0.1	1000
135.3	0.2	1000	381.67	0.2	1000
138.4	0.3	1000	388.14	0.3	1000
140.3	0.4	1000	385.98	0.4	1000

Dedicated to innovation in aerospace

Royal NLR - Netherlands Aerospace Centre

NLR operates as an objective and independent research centre, working with its partners towards a better world tomorrow. As part of that, NLR offers innovative solutions and technical expertise, creating a strong competitive position for the commercial sector.

NLR has been a centre of expertise for over a century now, with a deep-seated desire to keep innovating. It is an organisation that works to achieve sustainable, safe, efficient and effective aerospace operations.
The combination of in-depth insights into customers' needs, multidisciplinary expertise and state-of-the-art research facilities makes rapid innovation possible. Both domestically and abroad, NLR plays a pivotal role between science, the commercial sector and governmental authorities, bridging the gap between fundamental research and practical applications. Additionally, NLR is one of the large technological institutes (GTIs) that have been collaborating over a decade in the Netherlands on applied research united in the TO2 federation (Deltares, MARIN, NLR, TNO, Wageningen Research (WR) foundation).

From its main offices in Amsterdam and Marknesse plus two satellite offices, NLR helps to create a safe and sustainable society. It works with partners on numerous programmes in both civil aviation and defence, including work on complex composite structures for commercial aircraft and on goal-oriented use of the F-35 fighter. Additionally, NLR helps to achieve both Dutch and European goals and climate objectives in line with the Luchtvaartnota (Aviation Policy Document), the European Green Deal and Flightpath 2050, and by participating in programs such as Clean Sky and

For more information visit: **www.nlr.org**

Postal address
PO Box 90502
1006 BM Amsterdam, The Netherlands
e) info@nlr.nl **i)** www.nlr.org

Royal NLR
Anthony Fokkerweg 2
1059 CM Amsterdam, The Netherlands
p) +31 88 511 3113

Voorsterweg 31
8316 PR Marknesse, The Netherlands
p) +31 88 511 4444